

MITIGATION OF CONTRAST LOSS IN UNDERWATER IMAGES

A THESIS SUBMITTED TO THE UNIVERSITY OF MANCHESTER
FOR THE DEGREE OF DOCTOR OF PHILOSOPHY
IN THE FACULTY OF ENGINEERING AND PHYSICAL SCIENCES

2010

By
Halleh Mortazavi
Electrical and Electronic Engineering

Contents

List of Important Symbols	14
Abstract	15
Declaration	16
Copyright	17
Dedication	18
Acknowledgements	19
List of Publications & Presentations	20
1 Introduction	21
1.1 Aims and Objectives	24
1.2 Outline of the Thesis	25
2 Literature Review	27
2.1 Underwater Imaging	27
2.1.1 Scattering	27
2.1.2 Extinction	29
2.1.3 Underwater Image Geometry	29
2.2 Image Enhancement Methods	31
2.2.1 Hardware Based Approach	32
2.2.2 Non-hardware Based Approach	34
2.2.3 Comparison of Enhancement Methods	37
2.3 Other Technical Background	39
2.3.1 Recursive Gaussian Filter	39

2.3.2	Statistical Distribution of Image Texture	40
2.4	Colour	41
2.4.1	Human Visual System (HVS)	41
2.4.2	Colorimetry	43
2.4.3	CIE Colour Spaces	43
2.4.4	RGB and sRGB Colour Spaces	46
2.4.5	Multispectral Imaging	47
3	Experimental Methodology	48
3.1	Non-constrained Test Images	48
3.2	Constrained Test Images	48
3.2.1	Water Tank Experimental Setup	49
3.2.2	RGB Test Images	52
3.2.3	Multispectral Test Images	53
4	Degradations in Underwater Images	56
4.1	The Impact of L_2 and L_3 in Image Degradation	56
4.2	Experimental Characterisation	59
4.2.1	Results and Conclusion	61
5	Underwater Image Model	64
5.1	Forward Model of Image Formation	64
5.2	Image Recovery (Inversion Model)	66
5.3	Water Tank Experiment	66
5.3.1	Fixed Path	66
5.3.2	Regression Method	68
5.3.3	Experimental Design	68
5.3.4	Experimental Errors	69
5.3.5	Experimental Procedure	74
5.3.6	Results and Discussions	74
6	Mitigation of Contrast Loss	84
6.1	Estimation of b_λ and a_λ	85
6.1.1	Optical Back-scatter Model	85
6.1.2	Extinction Model	88
6.1.3	BS-MinPix Filter	90
6.1.4	BS-Hist Filter	91

6.1.5	BS-CostFunc Filter	91
7	Simulations	93
7.1	Synthetic Underwater Image	93
7.1.1	Formation of Image Content (\hat{I}_{syn})	94
7.1.2	Synthetic Optical Back-scatter	96
7.1.3	Synthetic Underwater Image	97
7.2	Monochrome Simulations	97
7.2.1	Performance Evaluation	99
7.2.2	Procedures and Results	100
7.3	Colour Simulations	110
7.3.1	Synthetic Colour Image Generation	111
7.3.2	Performance Evaluation	111
7.3.3	Simulation 1	112
7.3.4	Simulation 2	114
7.3.5	Simulation 3	117
8	Experimental Results	122
8.1	Introduction	122
8.2	Monochrome Images	123
8.2.1	Accuracy	123
8.2.2	Consistency	127
8.2.3	Quality	127
8.3	Colour Constrained Images	130
8.3.1	Experiment 1- Colour Images in Narrow Spectral Bands	130
8.3.2	Experiment 2- Colour Images in Wide Spectral Bands	130
8.4	Colour Non-constrained Images	133
9	Conclusions and Future Works	143
9.1	Conclusions	143
9.2	Suggestions for Future Work	147
A	Camera Specifications	149
A.1	Canon PowerShot Pro90 IS	149
A.2	Hamamatsu ORCA-ER	151
B	Oakley & Bu cost function with variable offset	152

List of Tables

3.1	Different levels of water turbidity for RGB test images.	53
3.2	Different levels of water turbidity for capturing multispectral test images.	55
5.1	The calculated value for the expected experimental error and c' coefficient at different wavelengths and different level of water turbidity.	77
7.1	Estimated values of Beta distribution parameters based on Attewell & Baddeley (2007) study for four different types of environments, Woodland, Beach, Urban and Interior.	95

List of Figures

1.1	Sample underwater images provided by the a) Racal Research (now Thales Research) in UK, b) ADMA oil company in Abu Dhabi. . . .	22
1.2	Underwater Image Geometry. $L1$ is the reflected light from the scene. $L2$ is the forward scattered light, with angel θ relative to the propagation direction. $L3$ is the optical back-scatter. R is the optical path distance.	23
2.1	Scattering pattern for different sizes of particles. (a) size: smaller than one tenth of the wavelength of light. (b) size: approximately one fourth the wavelength of light. (c) size: larger than the wavelength of light. .	28
2.2	The amount of image point misplacement due to forward-scatter light is Y_1	30
2.3	The authorised copy of the timing plot of range-gated imaging system from (C.S. Tan & He 2005). Reflected Image Temporal Profile (RITP) in time domain, for clear water condition with attenuation coefficient, $c=0.26/m$; absorption coefficient, $a= 0:04/m$ 1. Front RITP, 2. Middle RITP, 3. Tail RITP.	33
2.4	From left to right, each row contains the sample of a degraded underwater image, the printed by permission sample of processed images by POSHE and BBFHE methods.	38
2.5	The printed by permission sample of a) the degraded image (right side) and improved image (left side) by simple contrast loss method. b) the degraded image (left side) and improved image (right side) by polarisation method.	38

2.6	Probability Distribution Function of a) the Log-normal distribution with zero mean and different values of σ b) the Poisson distribution with two different parameters value of κ c) the Uniform distribution d) the Gaussian distribution with zero mean and two different values of σ e) the Beta distribution with different values of α_{Beta} & β_{Beta}	42
3.1	The schematic design of water tank experiment.	49
3.2	Resolution charts. a) The NBS chart b) The USAF chart c) A general resolution chart with low frequency bars.	51
3.3	The experimental arrangement to capture RGB test images. 1) Canon PowerShot Pro90 IS camera. 2) Halogen lamp 3) Water tank 4) Translation stage.	52
3.4	The experimental arrangement for capturing multispectral images. 1- a) Hyperspectral Camera, 1-b) VariSpec optics, 2) Halogen lamp, 3) Water tank, 4) Translation stage, 5) Host computer, 6) The electronics controller module.	54
4.1	(a) A target bar chart in a non scattering medium. (b) The line plot of the target bar chart.	57
4.2	The structure of a degraded underwater image. The values of optical distance and extinction coefficient are $R = 1m$ and $\beta = 0.5m^{-1}$. (a) Direct component, L_1 . (b) Back-scatter component, L_3 . (c) The combination of direct and back-scatter components. (d) Forward-scatter component, L_2 . (e) The combination of three components, which represents the degraded underwater image line plot.	58
4.3	The line plot of original image (dotted line) and the line plots of two degraded images (solid line) with two different degradation effects (a) Resolution loss (b) Contrast loss.	59
4.4	Experimental optical target.	60
4.5	Sample images from the target bar at different water conditions. S_0 is for clear water and S_1 - S_5 are for low to high water turbidity respectively. 61	
4.6	(a) The MTF charts for different levels of turbid water. (b) The plot of contrast and bandwidth with respect to the turbidity level.	63

5.1	The camera position is fixed at angle of β_1 and height of h_1 for capturing images from different locations of seabed. The optical path remains constant at d_1 while the seabed pattern is changing for different camera locations.	67
5.2	The schematic form of an image pixel coordinates for a sample of Fixed Path Vector, $v(p(x, y, 1), p(x, y, 2), \dots, p(x, y, n))$	67
5.3	The pixel $X(p)$ in (a) is misregistered to $X(p+r)$ in (b). The registration error is r pixel position.	71
5.4	The plot of σ_{Reg}^2 versus r in clear water condition for sample image (first camera position) at $600nm$	73
5.5	Sample of captured images (1024×1344) in $600nm$ wavelength at first camera position in a) Clear water condition b) Low level of turbid water, T_1 ($0.3gr/100litres$) c) Medium level of turbid water, T_2 ($0.7gr/100litres$) d) High level of turbid water, T_3 ($0.9gr/100litres$).	75
5.6	A block of 40×40 ($226 : 266, 330 : 370$) of neighboring pixels of pixel position $(244, 350)$ is selected and shown for all 10 images. The content of the sample image pixel in position of $(244, 350)$ in main image $((18, 20)$ in sample image block) is shown for different camera locations.	76
5.7	The plot of V_i versus V_f . V_i is the Fixed Path vector in turbid water condition and V_f is the Fixed Path vector in clear water condition. The estimated value of extinction and optical back-scatter are about 0.1857 and 156.9 respectively. The black solid line is for the regression line and the two red dashed lines in position of ± 4.62 from the regression line are defining the estimation intervals.	78
5.8	Dispersion value for all pixel positions at $600nm$, and for medium water turbidity, T_2 . The median dispersion for all pixel positions is 3.85 and the expected experimental error is 4.62.	79
5.9	Dispersion value for all pixel positions at $600nm$ for a) Low level of turbid water, T_1 . The median dispersion for all pixel positions is 10.19 and the expected experimental error is 9.16. b) High level of turbid water, T_3 . The median dispersion for all pixel positions is 2.28 and the expected experimental error is 3.55.	81

5.10	Dispersion value for all pixel positions at $550nm$ for medium level of turbid water, T_2 . The median dispersion for all pixel positions is 3.39 and the expected experimental error is 4.01.	82
5.11	Dispersion value for all pixel positions for medium level of turbid water, T_2 , at a) $650nm$. The median dispersion for all pixel positions is 4.21 and the expected experimental error is 4.38. b) $700nm$. The median dispersion for all pixel positions is 4.62 and the expected experimental error is 4.60.	83
6.1	a) A sample of underwater image in clear water condition, where the scene is illuminated by a search light. b) The line-plot of row=400 of the original image (dashed line) and the line-plot of row=400 of the filtered image by a low pass filter.	86
6.2	a) The sample image in size of 1024×1344 from from T_3 test images in $600nm$. b) The line-plots of row=500 for I_λ with a dash-dotted line, \bar{I}_λ with a dashed line, and b_λ with a solid line. c) The contour plot of the estimated optical back-scatter. d) The contour plot of the smoothed image.	89
7.1	a) The plot of μ_B and α_{Beta} , b) The plot of μ_B and β_{Beta} , for natural textures data from Attewell & Baddeley (2007) data.	95
7.2	a) A sample pattern of intensity variation across an image row generated by $\cos(\frac{\pi x}{1.5w} - \frac{\pi}{3})$, where w is for the width of an image row. In this example $w = 350$. b) A sample of synthetic optical back-scatter function, $b_{syn} = 0.8 \cos(\frac{\pi x}{1.5w} - \frac{\pi}{3})$	97
7.3	The formation of a synthetic monochrome underwater image. a) Synthetic image texture consisted of several blocks. The pixels intensity of each image block follow Beta distribution. b) The line plot of the light intensity variation. c) Synthetic underwater image in clear water condition under direct illumination, where its pattern is shown in (b). d) The line plot of the intensity of optical back-scatter variation. e) Synthetic degraded underwater image.	98
7.4	a) The plot of \mathcal{E}_{ave}/n_{mp} , b) The plot of \mathcal{E}_{std}/n_{mp} , c) The plot of $\mathcal{E}_{ave}/n_{HB}\%$, d) The plot of $\mathcal{E}_{std}/n_{HB}\%$ e) The plot of $\mathcal{E}_{ave}/\sigma_{cf}$ f) The plot of $\mathcal{E}_{std}/\sigma_{cf}$	102

7.5	a) The plot of $\mathcal{E}_{ave}/(M \times N)$ for different region scales of $m \times n$ for BS-CostFunc filter, b) The plot of $\mathcal{E}_{std}/(M \times N)$ for different region scales of $m \times n$ for BS-CostFunc filter, c) The plot of $\mathcal{E}'_{ave}/(M \times N)$ for different region scales of $m \times n$ for BS-CostFunc filter, d) The plot of $\mathcal{E}_{ave}/\sigma_n$ for BS-CostFunc, BS-MinPix and BS-Hist filters, e) The plot of $\mathcal{E}_{std}/\sigma_n$ for BS-CostFunc, BS-MinPix and BS-Hist filters, f) The plot of $\mathcal{E}'_{ave}/\sigma_n$ for BS-CostFunc filter.	104
7.6	a) The plot of $\mathcal{E}_{ave}/\mu_B(min)$ for BS-CostFunc, BS-MinPix and BS-Hist filters. b) The plot of $\mathcal{E}_{std}/\mu_B(min)$ for BS-CostFunc, BS-MinPix and BS-Hist filters. c) The plot of $\mathcal{E}'_{ave}/\mu_B(min)$ for BS-CostFunc.	107
7.7	a) Different synthetic light variation patterns using different θ . w is the size of an image row and x is the row pixel index. b) The plot of $\mathcal{E}_{ave}/\gamma_s$ using BS-CostFunc filter for different θ , c) The plot of $\mathcal{E}_{std}/\gamma_s$ using BS-CostFunc filter for different θ	108
7.8	a) The plot of \mathcal{E}'_{ave} versus intensity, b) The plot of \mathcal{E}^d_{ave} versus $\frac{\sigma_B}{W}$ for two image widths, $W=1050$ and $W=1400$ pixels.	110
7.9	The plot of mean colour difference, CD_m , for 100 images between Set I & Set II (dash-dotted line), and Set I and the clear reference image (solid line).	113
7.10	The plots of a) the halogen lamp power spectrum, b) the estimation error spectra.	115
7.11	The plot of mean colour difference, CD_m , for 100 images between Set III and the clear reference image (dash-dotted line), and Set IV and the clear reference image (solid line).	116
7.12	The plot of local standard deviation (std_b) versus local mean (m_b) for a) synthetic images in clear and turbid water conditions, b) two degraded synthetic images in turbid water condition at 600nm. Im_1 is one single image and Im_3 is from the combination of two degraded images, Im_1 and Im_2 at 600nm.	118
7.13	A sample of synthetic image converted to sRGB in a) clear water, b) turbid water, and improved images in c) Set I, d) Set II, e) Set III, f) Set IV.	121
8.1	The plot of γ versus image index, for three water turbidity levels, T_0 , T_1 and T_2	123

8.2	The selection of i) original images, and ii) improved images at 600 nm for different levels of water turbidity, a) T_0 , b) T_1 and c) T_2	125
8.3	a) The plot of \mathcal{E}'_{ave} versus wavelength (λ). b) The surf plot of γ versus image index at different spectral bands.	126
8.4	The selection of images in a) turbid water (T_1), b) improved from T_1 , c) improved from T_0 , d) clear water (T_0) at i) 550 nm, ii) 700 nm.	128
8.5	The selection of images in i) original images, ii) processed with the proposed method using BS-CostFunc filter, iii) processed with local histogram equalisation with 120 kernel size, for different levels of turbid water a) T_0 , b) T_1 , c) T_2	129
8.6	The selection of colour images from two different scenes, i) image 1, ii) image 10 for a) the degraded image from T_1 , b) the improved image with narrow spectral bands from T_1 , c) the reference image (improved with narrow spectral bands from T_0), d) the image from the clear water condition (T_0).	131
8.7	The plot of colour difference between the improved colour image in wide bands form T_1 and the reference image (the improved from T_0) for 10 images.	132
8.8	The selection of colour images from two different scenes, i) image 1, ii) image 10 for a) the degraded image from T_1 , b) the improved image in narrow spectral bands from T_1 , c) the improved image in wide spectral bands from T_1 d) the reference image (improved with narrow spectral bands from T_0).	134
8.9	The plot of γ versus image index for 100 images provided by a) the ADMA company, b) the Thales Research company	136
8.10	The sample of images from the ADMA oil company a) Original degraded image, b) Improved image by the proposed algorithm with BS-CostFunc filter, c) Improved image by Photoshop.	137
8.11	The sample of images from the Thales Research company a) Original degraded image, b) Improved image by the proposed algorithm, c) Improved image by Photoshop.	138
8.12	The sample of continuous images from the ADMA oil company video sequence. a) Image 1-6, b) Image 7-12.	139

8.13	The sample of continuous images from the ADMA oil company video sequence. a) Image 13-18, b) Image 19-24.	140
8.14	The sample of continuous images from the Thales Research company video sequence. a) Image 1-6, b) Image 7-12.	141
8.15	The sample of continuous images from the Thales Research company video sequence. a) Image 13-18, b) Image 19-24.	142
9.1	The chart is describing the effects of distance (R) and turbidity (β). The region A1 corresponds to parameter values for which both resolution loss and contrast loss are significant. The regions A2 corresponds to parameter values for which only contrast loss is significant and the image contrast is $> 5\%$ (Image enhancement is applicable). The region A3 corresponds to parameter values for which only contrast loss is significant, but the image contrast is very low $< 5\%$	144

List of Important Symbols

R	Optical depth
λ	The wavelength of light
Im_λ	Degraded underwater image pixel intensity
A_λ	Direct component (Image content)
FS_λ	Forward-scatter component
BS_λ	Optical back-scatter component
F_λ	The reflectance factor of scene content
$T_0 - T_3$	Water turbidity level for multispectral images
$S_0 - S_7$	Water turbidity level for RGB images
a_λ	Extinction parameter
b_λ	Optical back-scatter parameter
γ	The parameter of optical back-scatter level
σ_{cf}	BS-CostFunc filter parameter
σ_B	Image smoothing filter parameter
σ_n	Standard deviation due to noise
\mathcal{E}_{ave}	Absolute mean estimation error
\mathcal{E}'_{ave}	Signed mean estimation error
\mathcal{E}_{std}	Standard deviation of absolute estimation error
\mathcal{E}_p^d	Difference between the spatial distribution of estimated optical back-scatter and the synthetic optical back-scatter at pixel p
p	Image pixel index
P	total number of pixels in an image
n_{mp}	Number of pixel samples in BS-MinPix filter
μ_B	Minimum of the mean value of each synthetic image block
$n_{HB}\%$	BS-Hist filter parameter
$S(\lambda)$	Illumination power spectrum
$R(\lambda)$	The spectrum of an object
ΔE_{ab}	Colour difference in CIELab for one pixel
CD_m	Mean colour difference for all image pixels
JND	Just noticeable colour difference (JND = 2.3)

Abstract

The University of Manchester

Halleh Mortazavi

2010

Degree of Doctor of Philosophy

The quality of an underwater image is degraded due to the effects of light scattering in water, which are resolution loss and contrast loss. Contrast loss is the main degradation problem in underwater images which is caused by the effect of optical back-scatter.

A method is proposed to improve the contrast of an underwater image by mitigating the effect of optical back-scatter after image acquisition. The proposed method is based on the inverse model of an underwater image model, which is validated experimentally in this work. It suggests that the recovered image can be obtained by subtracting the intensity value due to the effect of optical back-scatter from the degraded image pixel and then scaling the remaining by a factor due to the effect of optical extinction.

Three filters are proposed to estimate for optical back-scatter in a degraded image. Among these three filters, the performance of BS-CostFunc filter is the best. The physical model of the optical extinction indicates that the optical extinction can be calculated by knowing the level of optical back-scatter.

Results from simulations with synthetic images and experiments with real constrained images in monochrome indicate that the maximum optical back-scatter estimation error is less than 5%. The proposed algorithm can significantly improve the contrast of a monochrome underwater image. Results of colour simulations with synthetic colour images and experiments with real constrained colour images indicate that the proposed method is applicable to colour images with colour fidelity. However, for colour images in wide spectral bands, such as RGB, the colour of the improved images is similar to the colour of that of the reference images. Yet, the improved images are darker than the reference images in terms of intensity. The darkness of the improved images is because of the effect of noise on the level of estimation errors.

Declaration

No portion of the work referred to in this thesis has been submitted in support of an application for another degree or qualification of this or any other university or other institute of learning.

Copyright

- i. The author of this thesis (including any appendices and/or schedules to this thesis) owns any copyright in it (the “Copyright”) and s/he has given The University of Manchester the right to use such Copyright for any administrative, promotional, educational and/or teaching purposes.
- ii. Copies of this thesis, either in full or in extracts, may be made only in accordance with the regulations of the John Rylands University Library of Manchester. Details of these regulations may be obtained from the Librarian. This page must form part of any such copies made.
- iii. The ownership of any patents, designs, trade marks and any and all other intellectual property rights except for the Copyright (the “Intellectual Property Rights”) and any reproductions of copyright works, for example graphs and tables (“Reproductions”), which may be described in this thesis, may not be owned by the author and may be owned by third parties. Such Intellectual Property Rights and Reproductions cannot and must not be made available for use without the prior written permission of the owner(s) of the relevant Intellectual Property Rights and/or Reproductions.
- iv. Further information on the conditions under which disclosure, publication and exploitation of this thesis, the Copyright and any Intellectual Property Rights and/or Reproductions described in it may take place is available from the Head of School of Electrical and Electronic Engineering (or the Vice-President).

Dedication

To my family with sincere love and respect.

Acknowledgements

I am grateful for all the confidence, advice, and invaluable guidance from my excellent PhD supervisor Dr. John Oakley. He has been always understanding, encouraging and supportive. I appreciate his effort to provide financial support for this project from the department of Electrical and Electronic Eng. at The University of Manchester, and also his support to start the collaboration with the Petroleum Institute in Abu Dhabi.

I would like to thank Prof. David Foster for his constructive discussions in colour science. I sincerely appreciate his commitment to access the multispectral imaging equipment and facilities. Many thanks to Dr. Kinjiro Amano for the time and effort he dedicated to capture multispectral images. Thanks to Dr. Ivan Marin-Franch and Dr. Kamila Zychaluk for their very helpful discussions in statistics. Special thanks to Dr. Braham Barkat, the principal investigator from the Petroleum Institute (PI), for his helpful consultations in statistics specially in regression concept. I appreciate his support to acquire a sample of real underwater video from the ADMA oil company, and also to proofread the conference papers and this thesis.

Thanks to Dr. Fabrizio Lamberti, Dr. Yoav Schechner, and Dr. Hong Bu for providing sample processed images, Dr. David Attwell for his helpful discussions and consultations in natural image texture. Thanks to Dr. Hujin Yin for his comments and support, and Mr. Matthew Mould for his comments on this thesis, and all the people from the Sensing, Imaging, and Signal Processing group at the University of Manchester for creating a warm, friendly working environment.

I express my gratitude to my parents, Dr. Atta Mortazavi and Mrs. Sedighe Rafsanjani, who have always been an inspiring example for me, for their love and financial support. My heartfelt thanks goes to my husband, Dr. Behrooz Ghasemi, and my daughter, Hedye, who supported me by their love and patience throughout this journey.

I acknowledge this work is financially supported by the department of Electrical and Electronic Eng. at The University of Manchester. This work is in collaborations with the Petroleum Institute of Abu Dhabi.

List of Publications & Presentations

- H. Mortazavi, 'Underwater Image Enhancement', Subsea Instrumentation Meeting, March 2009, University of Aberdeen, Aberdeen, UK
- H. Mortazavi, 'Underwater Image Enhancement by Optical Back-scatter Compensation', Nov 2008, EEE Postgraduate Poster Conference, The University of Manchester, Manchester, UK
- H. Mortazavi and J. Oakley, Underwater image enhancement by backscatter compensation, ICMSAO2007 Conf. (2007), Abu Dhabi

Chapter 1

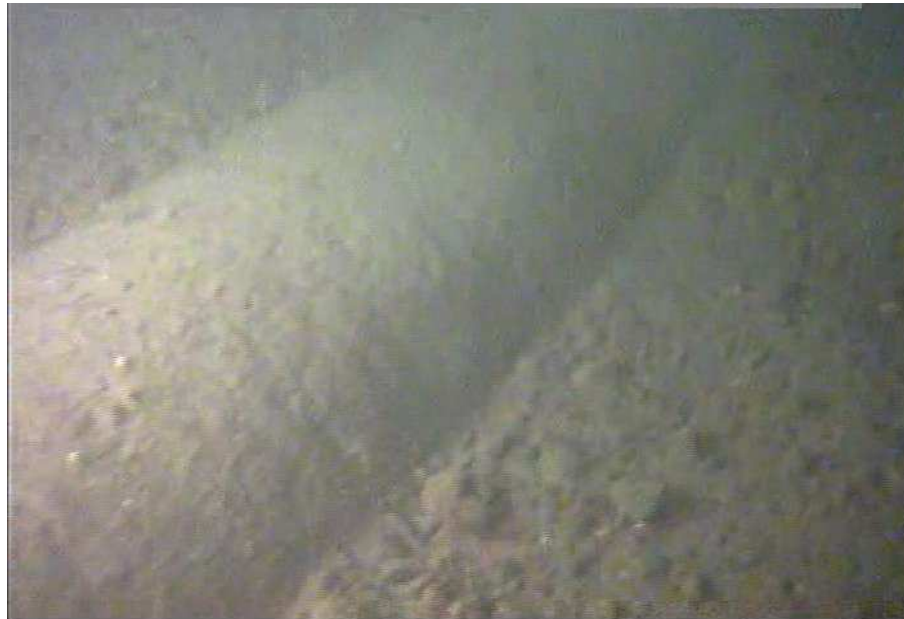
Introduction

The capability to produce high quality underwater images is demanded in many areas, such as mine detection (Rao, Mukherjee, Gupta, Ray & Phoha 2009), inspection of underwater power, telecommunication cables and pipelines (Narimani, Nazem & Loueipour 2009, Foresti 2001), research in marine biology (Dahms & Hwang 2010, Ahlen & Sundgren 2003, Cronin, Shashar, Caldwell, Marshal, Cheroske & Chiou 2003) archaeology (Arnott, Dix, Best & Gregory 2005, Kahanov & Royal 2001) and mapping (Botelho, Jr & Leivas 2008, Xu & Negahdaripour 1999).

In water medium, the visibility is often poor, and as a result the quality of images is limited. When light travels in water it interacts not only with water molecules but also with any suspended particles and sometimes air bubbles (Gutierrez, Seron, Munoz & Anson 2008), causing optical scattering and absorption. All these effects contribute to severe image degradation in form of resolution loss, contrast loss and colour changes (Hou 2009).

Figure 1.1 shows two underwater images from two different locations. Figure 1.1(a) and (b) are kindly provided by Racal Research (now Thales Research) in UK, and the ADMA oil company in Abu Dhabi respectively. It can clearly be seen that the quality of both images is poor.

Underwater imaging is often done by using a remotely operated vehicle (ROV), particularly when inspecting underwater pipelines and cables. A light source, which provides the required illumination, and a camera are both mounted on the ROV. A schematic for general underwater imaging is shown in Figure 1.2. The total light intensity that enters the camera lens and forms the image is the sum of three components, L_1 , L_2 and L_3 . L_1 is the reflected light from the scene and contains the useful image



(a)



(b)

Figure 1.1: Sample underwater images provided by the a) Racal Research (now Thales Research) in UK, b) ADMA oil company in Abu Dhabi.

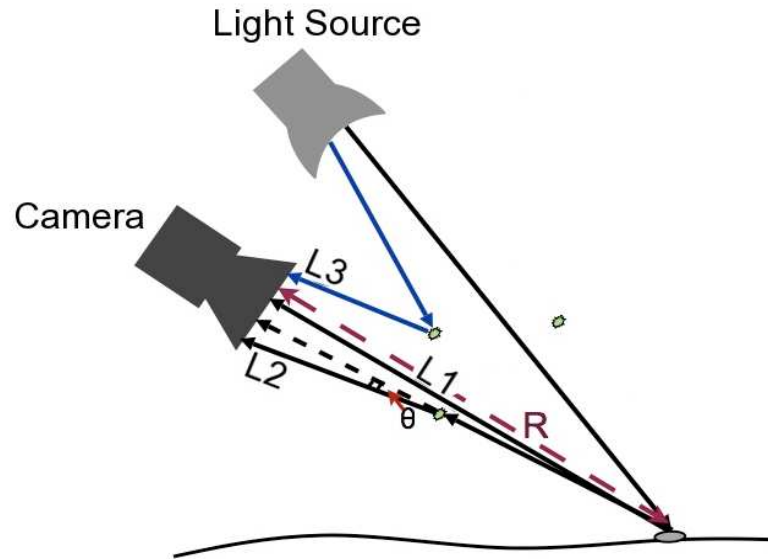


Figure 1.2: Underwater Image Geometry. $L1$ is the reflected light from the scene. $L2$ is the forward scattered light, with angle θ relative to the propagation direction. $L3$ is the optical back-scatter. R is the optical path distance.

content. $L2$ is reflected light from the scene that is scattered before reaching the camera lens. This is known as forward scattered light and given rise to the effect of image blur. $L3$ is the optical back-scatter, which is the light scattered towards the camera lens by particles between the camera and the scene. $L3$ adds extra lightness to the image and causes contrast loss.

Among the problems of contrast loss, resolution loss and colour changes in an underwater image, the contrast loss and resolution loss are the effects which degrade the apparent visibility and are most important. Therefore, to improve the visibility of an underwater image, the main degradation effect should be mitigated. Schechner & Karpel (2005) suggest that contrast loss is the significant degradation effect in an underwater image in visible wavelength. However, this seems to be an assumption and no experimental evidence is presented. The main degradation effect is investigated experimentally in this work and the experimental results will show that contrast loss is the main problem.

Several methods are available to overcome the effect of contrast loss. These methods can be categorised in to two approaches, physics-based and non physics-based. The methods in non physics-based approach process the image using no information about the physical formation of the image. Examples include unsharp masking

(Gonzalez & Woods 2008) and histogram equalisation (Kim, Kim & Hwang 2001). It is explained that contrast loss is because of optical scattering. Optical scattering depends on several parameters, such as illumination, wavelength, the optical distance and the water type (which means the size and distribution of suspended particles in water). In general the effect of contrast loss is non-stationary across the image (Schechner & Karpel 2005). Existing enhancement methods are based on the assumption that the noise is spatially invariant. Therefore, they provide only limited contrast improvement (Treibitz & Schechner 2006).

In the physics-based approach, a physical model of an image in a water medium, which is presented in Equation (1.1), explored to mitigate contrast loss.

$$I = S + B, \quad (1.1)$$

where I is the degraded image and S is the attenuated signal from the scene and B is the signal from suspended particles. The contrast of an underwater image can be improved by a subtraction of optical back-scatter from the degraded image, $I - B$. This can be achieved either by eliminating the optical back-scatter using special imaging hardware or by arithmetic processing of the image after acquisition. Examples of the former include polarization (Schechner & Karpel 2005) and signal gating (Tan, Seet, Sluzek & He 2005), which can significantly mitigate the effect of contrast loss and improve the image visibility. However, the use of such hardware-based techniques introduces extra cost and restricts applicability. Less attention has been given to the arithmetic approach, which is the subject of this thesis.

1.1 Aims and Objectives

In this work, it is shown that contrast loss is the main problem with underwater images. A forward model of an underwater image is given, which is validated in this work. A new physics-based method is proposed, based on the inverse model of an underwater image, to improve the apparent visibility of an underwater image by mitigating the effect of optical back-scatter. The proposed method is applicable to underwater images with only contrast loss problem. The method does not require any special equipment, and the images can be taken by any digital camera. This method involves using statistical properties of the image to estimate the optical back-scatter. It is shown by experimental results that the method can significantly improve the image contrast, and also can be applied to both monochrome and colour images with colour fidelity.

1.2 Outline of the Thesis

This thesis contains nine chapters, including this introduction. Below is the structure of each chapter.

Chapter 2 Literature Review This chapter presents a review of the existing work relevant to the aims of this study. First, optical scattering is explained as well as more details on the image formation process. Next, current image contrast enhancement methods, such as histogram modification, unsharp masking, polarization, signal gating and Oakley-Bu cost function are explained. Then, an explanation is given about recursive Gaussian filter and the statistical distribution of natural image texture. Finally, is a brief review on colour science concepts. This includes an explanation of the human vision system, some colour spaces, colour temperature and colour difference.

Chapter 3 Experimental Methodology In this chapter, the design and the preparations of test images are described.

Chapter 4 Degradations in Underwater Images This chapter, the impact of contrast loss and resolution loss are compared in a practical underwater situation. It is shown experimentally that contrast loss is the dominant degradation effect when compared with resolution loss.

Chapter 5 Underwater Image Model This chapter presents the mathematical forward model of a degraded underwater image and supporting experiments to validate the proposed model.

Chapter 6 Mitigation of Contrast Loss in Underwater Images In this chapter, a new method is proposed based on the inverse of an underwater image model. It is shown that to improve the contrast of an underwater image, an estimate for the level of optical back-scatter is required. Three different optical back-scatter filters are explained to estimate the level of optical back-scatter in a degraded underwater image without using any information about the physical properties of the scene.

Chapter 7 Simulations This chapter explores the performance of three optical back-scatter filters using Monte-Carlo simulations with synthetic underwater images and under different statistical assumptions. The accuracy of BS-CostFunc filter

for processing monochrome and colour images are examined. Colour fidelity is investigated for the improved colour images by the proposed method.

Chapter 8 Experimental Results This chapter evaluates the performance of the proposed method using real constrained and non-constrained underwater images. The accuracy and consistency of the estimated optical back-scatter parameter is evaluated for monochrome constrained images. Colour fidelity is investigated for the processed constrained colour images in both narrow and wide spectral bands. Examples of the improved images are presented.

Chapter 9 Conclusions and Future Works Conclusions from the simulations and experimental results are drawn and the possible future works are suggested.

Chapter 2

Literature Review

This chapter is structured as follow. Section 2.1 reviews background on the underwater imaging environment, with reference to optical scattering and underwater image geometry. A review of existing contrast enhancement methods is provided in Section 2.2. Some other techniques that are used in throughout this work are reviewed in Section 2.3. These include the statistical distribution of an image texture, recursive Gaussian filter and the fundamental concepts in colour science.

2.1 Underwater Imaging

To understand why underwater images are degraded, the propagation of light in a water medium is studied. First, light scattering and extinction are explained followed by an explanation of underwater image geometry. A physical model of the three basis intensity components of underwater image are described in more detail.

2.1.1 Scattering

Optical scattering happens when a light beam interacts with a particle. The level of optical scattering varies for different sizes of particles. The pattern of the scattering depends on the ratio of particle size to the light wavelength. Very small particles, such as molecules in the atmosphere, tend to scatter isotropically. This type of scattering can be explained by Rayleigh theory (McCartney 1976). When the size of particle is larger than the wavelength of visible light, the scattering pattern is more complex and is concentrated in the forward direction. The Mie theory is used to describe scattering by such particles (McCartney 1976). Figure 2.1 shows the pattern of scattering for

different sizes of particle.

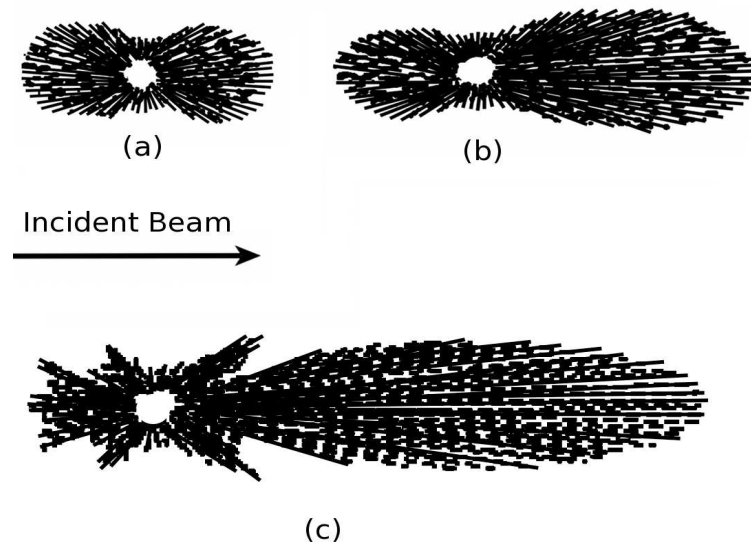


Figure 2.1: Scattering pattern for different sizes of particles. (a) size: smaller than one tenth of the wavelength of light. (b) size: approximately one fourth the wavelength of light. (c) size: larger than the wavelength of light.

Optical Forward Scatter

Light scattered in the same direction as the source light is known as optical forward scatter. When the particle diameter is larger than the scattering wavelength, the pattern of scattering usually shows some peaks at other angles. If the angle is small, then the phenomenon is known as small angle forward scattered in literature (Kopeika, I.Dror & Sadot 1998).

Optical Back-scatter

The light scattered back toward the light source from suspended particles, which are between the camera and the object, is known as optical back-scatter or back-scattered light.

2.1.2 Extinction

The term extinction means the loss of intensity during propagation through a turbid medium. Two different mechanisms contribute to extinction, absorption and scattering (Kokhanovsky 2008, McCartney 1976).

2.1.3 Underwater Image Geometry

The underwater image geometry is shown in Figure 1.2. $L1$ is the reflected light from the scene. $L2$ is the forward scattered light, with angle θ relative to the propagation direction. $L3$ is the optical back-scatter. These components are described in detail below.

Direct Component (L1)

The direct component is the direct reflected light from the scene reaching the camera lens. This carries the scene information with attenuation due to extinction. Equation (2.1) presents the physical model of the direct component (Schechner & Karpel 2004).

$$A_\lambda(x, y) = C_0 J_\lambda(x, y) \exp(-\beta_\lambda(x, y)R), \quad (2.1)$$

where C_0 is the illumination radiance, λ is the light wavelength, $J_\lambda(x, y)$ is the scene reflectance, R is the distance of optical path, and $\beta_\lambda(x, y)$ is the extinction coefficient (β_λ) at pixel position (x, y) , in which β_λ has the form

$$\beta_\lambda = \beta_\lambda^{sca} + \beta_\lambda^{abs}, \quad (2.2)$$

$$= D\pi a^2 Q_\lambda^{sca} + \beta_\lambda^{abs}, \quad (2.3)$$

where D is the particles concentration, a is the particle radius, Q_λ^{sca} is the Mie scattering factor and β_λ^{abs} is the absorption coefficient.

Forward-scatter Component (L2)

The forward-scatter component represents the light scattered forward over a small range of angles relative to the propagation direction. The forward-scatter component originates from the same scene point as the direct component, but enters the imaging device at a different angle and causes the same object point to be detected at different adjacent image points separated by a distance Y_1 as shown in Figure 2.2. This effect

is known as the adjacency effect (Kopeika 1998). The distribution of angles can be estimated by using the Fraunhofer diffraction equation for a single slit (Freeman & Hull 2003) by

$$\theta_{max} = \frac{\lambda}{d}, \quad (2.4)$$

where d is the particle diameter and λ is the light wavelength as defined before. Yura

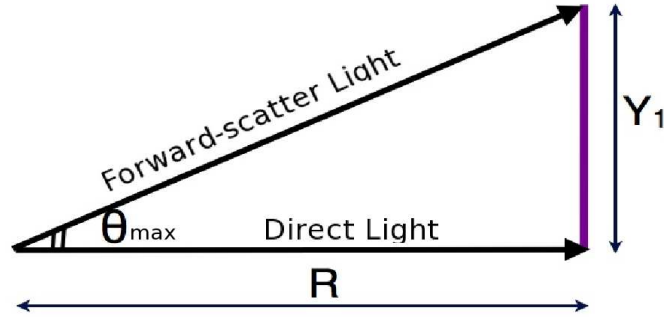


Figure 2.2: The amount of image point misplacement due to forward-scatter light is Y_1 .

(1971) and Ishimaru (1978) suggest that forward-scatter component is the cause for resolution loss (image blur), when the angle is $0^\circ < \theta_{max} \leq 1^\circ$.

An approximate value of forward-scatter component, $FS_\lambda(x, y)$, can be found (Yu & Liu 2007, Jaffe 1990) by

$$FS_\lambda(x, y) = A_\lambda(x, y) * g, \quad (2.5)$$

where g is the point-spread function (PSF) of water and $*$ denotes the convolution operation. There are several models suggested for the form of underwater PSF (Yu & Liu 2007, Voss 1991). For example, Jaffe (1990) suggested the model

$$g = (e^{-\eta R} - e^{-\beta R})F^{-1}(e^{-KR\omega}), \quad (2.6)$$

where $K > 0$ and η are empirical constants and related to water properties, and β is the extinction coefficient. The η is limited to $\eta \leq \beta$. F^{-1} is the inverse Fourier transform, and ω is the spatial frequency of image plane (It seems ω is the polar spatial frequency, as the author has not mentioned the horizontal or vertical component of ω). As Equation (2.6) shows, g comprises of two parts. The first part, $e^{-\eta R} - e^{-\beta R}$, causes

attenuation and depends on R , η and β . The second part, $e^{-KR\omega}$, is a low pass filter and introduces the spatial blur and depends on R and K . This implies for a specific θ_{max} the amount of image blur (misplacement of Y_1) depends on R . As R increases the amount of misplacement, Y_1 , increases as well. Thus, g is the cause of two effects, attenuation and image blur, and as a result forward-scatter component is a blurred and attenuated version of the direct component (Schechner & Karpel 2005).

Back-scatter Component, L3

Optical back-scatter does not originate from the scene, so it does not contain any scene information. It is the scattered light from particles between the camera and scene. Optical back-scatter adds extra illumination to the image intensity. This extra intensity causes a reduction in image contrast. The optical back-scatter component is the main contribution to contrast loss. A physical model of back-scatter component is presented in Equation (2.7)

$$BS_{\lambda}(x, y) = C_0(1 - \exp(-\beta_{\lambda}(x, y)R)). \quad (2.7)$$

It can be seen from Equations (2.3) and (2.7), that back-scatter component depends on the parameters of the optical depth, density and particle size. Varying any of these parameters causes the amount of optical back-scatter to change, resulting a change in the image contrast.

2.2 Image Enhancement Methods

The process of improving a degraded image to visibly look better is called image enhancement (Petrou & Bosdogianni 1999). It is explained that, due to the effect of optical back-scatter, the images in a scattering medium have low contrast. By improving the image contrast, it is expected to increase the visibility and discern more detail. There are different definitions for measuring image contrast. One of the common definitions for image contrast, c , is the Michelson formula (Peli 1990)

$$c = \frac{I_{max} - I_{min}}{I_{max} + I_{min}}, \quad (2.8)$$

where I_{max} and I_{min} are for the maximum and minimum image intensity values respectively.

There are different techniques to improve the contrast of an image. These techniques can be classified in to two approaches, hardware based and non-hardware based approach.

2.2.1 Hardware Based Approach

Hardware based approach requires special equipment, two common examples include polarisation and range-gated.

Range-gated

Range-gated or time-gated is one of the hardware methods to improve the image quality and visibility in turbid conditions (Caimi, Kocak, Dalgleish & Watson 2010, Tan, Sluzek, L. & Jiang 2007, Liu, Chen & Xia 1994). In range-gated underwater imaging system the camera is adjacent to the light source, while the underwater target is behind the scattering medium (Tan et al. 2005). The operation of range-gated system is to select the reflected light from the object that arrives at the camera, and to block the optical back-scatter light (Li, Wang, Bai, Jin, Huang & Ding 2009).

Range-gated system includes a broad-beam pulse as the illumination source, a high speed gated camera and a synchronization gate duration control (Li et al. 2009). Tan et al. (2005) presented a sample plot of the timing of range-gated imaging in their work. The authorised copy of the plot is shown in Figure 2.3.

A range-gating process starts when the laser sends a pulse onto the object. As the light travels the camera gate is closed. Thus, the back-scattered light will not be captured. The fast electronic shutter of the gated camera is time delayed and only opens for a very short period of time. When the laser pulse returns to the camera after hitting the object, the camera gate opens. In this case, the camera is exposed only to the reflected light from the object. Once the laser pulse is over, the camera gate closes again. The opening or closing of the camera gate is based on the prior information about the object location (Tan et al. 2007).

Speckle noise is the main problem in these images. The interference between the reflected light waves back from a rough surface causes the speckle noise. For the non-coherent light this speckle pattern can not be detected, whereas for the coherent light the speckle pattern is detectable. As the laser beams are highly coherent, the speckle noise is evident in these images. Recent range-gated system improved to suppress speckle noise (Li et al. 2009), and also use high sampling rates, which allow for 3-D

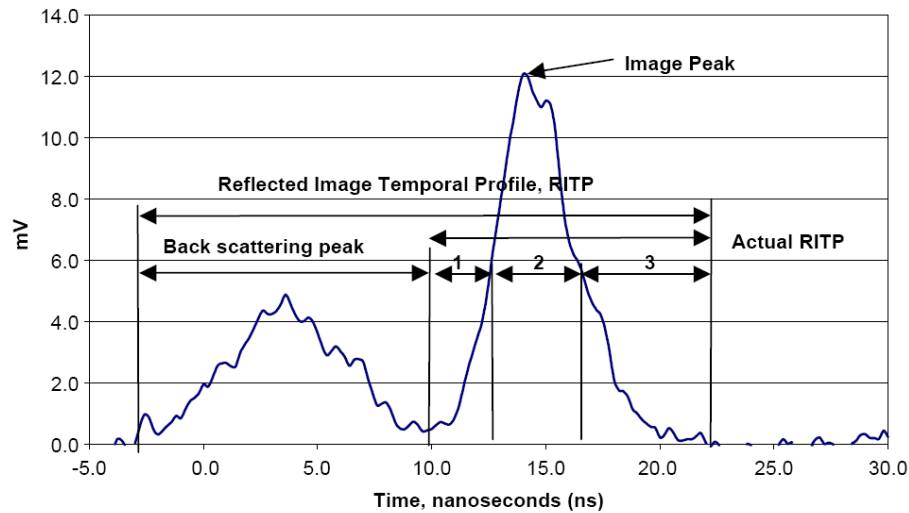


Figure 2.3: The authorised copy of the timing plot of range-gated imaging system from (C.S. Tan & He 2005). Reflected Image Temporal Profile (RITP) in time domain, for clear water condition with attenuation coefficient, $c=0.26/m$; absorption coefficient, $a=0.04/m$ 1. Front RITP, 2. Middle RITP, 3. Tail RITP.

image reconstruction (Caimi et al. 2010).

Polarisation

Light has three properties, intensity, wavelength, and polarisation. The human vision system and some animals can detect polarisation and use it in many different ways such as enhancing visibility (Yemelyanov, Lin, Pugh, Jr. & Engheta 2006). Natural light is initially unpolarised, but light reaching to a camera often has biased polarisation due to scattering and reflection (Lin, Yemelyanov, Jr. & Engheta 2004). Light polarisation conveys different information of the scene (Lin et al. 2004). Inspired by animal polarisation vision, a polarisation imaging technique has been developed. To collect light polarisation data, polarisation-sensitive imaging and sensing systems are required (Lin et al. 2004).

Preliminary studies showed that back-scatter light can be reduced by polarisation (Lewis, Jordan & Roberts 1999, Treibitz & Schechner 2006). Some studies assume the reflected light from the object is significantly polarised rather than the back-scatter (Tyo, Rowe, Jr. & Engheta 1996) and in some other studies the contrary is assumed (Treibitz & Schechner 2009). Also, in some studies active illumination, a polarised

light source, is used (Treibitz & Schechner 2006), whereas in other study passive illumination, ambient light, is used for imaging (Chang, Flitton, Hopcraft, Jakeman, Jordan & Walker 2003). Polarisation difference imaging (PDI) method process the intensity of two images obtained at two orthogonal polarisations (Lin et al. 2004, Tyo et al. 1996). Schechner & Karpel (2005) introduced a method which is based on the physical model of visibility degradations to recover underwater images using raw images through different states of polarising filter. In this method visibility can be restored significantly, but remains some noise due to pixels falling on distant objects. A technique is developed to reduce the noise (Schechner & Averbuch 2007). This method is developed to capture images faster, and as a result may be able to estimate a rough 3D scene structure (Treibitz & Schechner 2009).

2.2.2 Non-hardware Based Approach

In non-hardware based approach, no special imaging equipment is required and only digital image processing tools are used. Two common examples include histogram equalisation and unsharp masking.

Histogram Equalisation

Histogram equalisation (HE) is the most common enhancement method because of its simplicity and effectiveness (Kim et al. 2001). The operation of HE is to redistribute the probabilities of gray levels occurrences in such a way that the histogram of the output image to be close to the uniform distribution (Colombo & Jaarsma 1980). Histogram equalisation does not consider the content of an image, only the gray level distribution.

Different HE methods have been developed (Levman, Alirezai & Khan 2003). These methods can be generally classified in to two categories, global and local (Alparslan & Ince 1980, Abdullah-Al-Wadud, Kabir, Dewan & Chae 2007). Global HE processes the histogram of the whole image. Although it is effective, but it has important limitation (Kim et al. 2001). Global HE stretches the contrast over the whole image, and sometimes this causes loss of information in dark regions (Abdullah-Al-Wadud et al. 2007). To overcome this limitation, a local HE technique developed (Alparslan & Ince 1980, Kim et al. 2001, Zhu, Chan & Lam 1999). Local HE uses a small window that slides sequentially through every pixel of the image. Only blocks of the image that fall in this window are processed for HE and the gray level mapping is done for the

centre pixel of that window (Abdullah-Al-Wadud et al. 2007). Local HE is more powerful, but requires more computation. Local HE sometimes causes over enhancement in some parts of the image, and also increases the image noise (Abdullah-Al-Wadud et al. 2007). Some methods have been developed to speed up the computation, such as partially overlapped HE (POSHE) and block based binomial filtering HE (BBFHE) (Lamberti, Montrucchio & Sanna 2004).

HE is designed for monochrome (single channel) images. Extending HE to color images is not straightforward (Weeks, Sartor & Myler 1999, Forrest 2005). The simplest method is to apply HE to each colour channel, R, G and B separately. However, this doesn't take into account the correlations between channels, and as a result causes colour changes (Buzuloiu, Ciuc, Rangayyan & Vertan 2001). The other method is to convert the colour space to hue, saturation, intensity (HSI) colour space and apply HE to intensity and saturation, leaving the hue unchanged (Duan & Qiu 2004, Buzuloiu et al. 2001). Recent methods have been developed to extend HE to images with any number of dimensions (Kim & Yang 2006, Forrest 2005).

Unsharp Masking

Unsharp masking (UM) is the other common image enhancement method (Levi & Mossel 1976, Gasparini, Corchs & Schettini 2007, Ferrari, Flores & Garcia-Torales 2010, Lee, Kim, Park, Suryanto & Ko 2008). In this method the image is improved by emphasizing the high frequency components in the image (Jain 1989, Badamchizadeh & Aghagolzadeh 2004, Gonzalez & Woods 2008).

The UM method is derived from an earlier photographic technique and involves subtracting the blurred version of an image from the image itself (Gonzalez & Woods 2008). This is equivalent to adding a scaled high-pass filtered version of the image to itself (Tao, Lin, Bao, Dong & Clapworthy 2009) as shown in Equation (2.9). The high pass filtering is usually done with a Laplacian operator (Sivaswamy, Salcic & Ling 2001).

$$y(m, n) = x(m, n) + \hat{\lambda}z(m, n), \quad (2.9)$$

where $x(m, n)$ is the original image, $\hat{\lambda}$ is a constant, greater than zero, that changes the grade of sharpness as desired and $z(m, n)$ is the high-pass filtered version of the original image.

Although this method is easy to implement, it is very sensitive to noise and also causes digitizing effects and blocking artifacts (Gasparini et al. 2007). Different methods of UM have been introduced to mitigate these problems. Non-linear filters, such as polynomial (Gasparini et al. 2007) and quadratic filters (Sivaswamy et al. 2001) are used instead of the high pass filter in the UM algorithm (Badamchizadeh & Aghagolzadeh 2004). Adaptive UM uses a variable factor $\hat{\lambda}$ and the value of this factor is controlled by neighborhood pixel values (Polesel, Ramponi & Mathews 2000). In the adaptive method, the low contrast details are more enhanced than the high contrast details (Badamchizadeh & Aghagolzadeh 2004). Unsharp masking tends to introduce colour distortion, when applied to colour images (Cheikh & Gabbouj 2000). Lee et al. (2008) introduce a method to sharpen the image appearance without distorting the colour and amplifying the noise.

Simple Contrast Loss (Oakley and Bu Cost Function)

Oakley and Bu (Oakley & Bu 2007) introduce a statistical method using the standard deviation of the normalised brightness of an image to detect the presence of optical back-scatter in a degraded image. It is assumed that the level of the optical back-scatter is constant throughout the image. This algorithm is based on finding the minimum of a global cost function (Oakley & Bu 2007).

The proposed algorithm for optical back-scatter estimation is to find the minimum value of a cost function that is a scaled version of the standard deviation of the normalised intensity.

The key feature of this method is that it does not require any segmentation as it uses a global statistic rather than the sample standard deviation of small blocks.

The enhanced version of an image has the form:

$$\hat{I} = m(I - b), \quad (2.10)$$

where I is the degraded image, b is an estimate of the optical back-scatter contributed part of the image, \hat{I} is the modified image and m is the scaling parameter. The estimated value of optical back-scatter has been shown

$$\operatorname{argmin}\{S(b)\}, \quad (2.11)$$

where

$$S(b) = \frac{1}{P} \sum_{p=1}^P \left(\frac{I_p - \bar{I}_p}{\bar{I}_p - b} \right)^2 GM\{(\bar{I}_p - b)^2 : p = 1, 2, \dots, P\}. \quad (2.12)$$

p is the pixel position, P is the total number of pixels, I is the degraded image, \bar{I} is the smooth version of the image, which is calculated by recursive Gaussian filter with σ_{cf} filter parameter, and b is the value of optical back-scatter. $GM\{\cdot\}$ denotes the geometric mean which may be computed from

$$GM\{x_p : p = 1, 2, \dots, P\} = (x_1 x_2 \dots x_P)^{\frac{1}{P}}. \quad (2.13)$$

From Equations (2.12) and (2.13), $S(b)$ can be written as:

$$S(b) = \frac{1}{P} \sum_{p=1}^P \left(\frac{I_p - \bar{I}_p}{\bar{I}_p - b} \right)^2 \exp \left(\frac{1}{P} \sum_{p=1}^P \ln(\bar{I}_p - b)^2 \right). \quad (2.14)$$

2.2.3 Comparison of Enhancement Methods

Contrast loss spatially varies for underwater images. This is because active illumination, i.e. a light source, is normally used for underwater imaging, since natural illumination is often not sufficient. The active light source illuminates the scene in a nonuniform way. The part in the direction of the light source is well illuminated and the other areas are less illuminated. This causes a nonuniform distribution of optical back-scatter. The other cause of spatial variation in contrast is that in an image, the objects at a greater distance from the camera have more contrast loss than closer objects.

Unsharp masking and histogram equalisation are both spatially invariant and as a result can apply limited correction in such cases. Also, these methods generally introduce some noise in the enhanced image. The sample images from real underwater situation are processed by POSHE and BBFHE methods¹ and presented in Figure 2.4. It can be seen that small details, as well as noise, are over enhanced.

The simple contrast loss method is designed for compensating the effect of optical back-scatter for images in air. The printed by permission sample of the processed image with simple contrast loss² is shown in Figure 2.5 (a). In the simple contrast model it is assumed that the level of optical back-scatter is constant across the image

¹The images are kindly processed by Dr. Fabrizio Lamberti with his original code.

²The image is processed by Dr. Hong Bu.

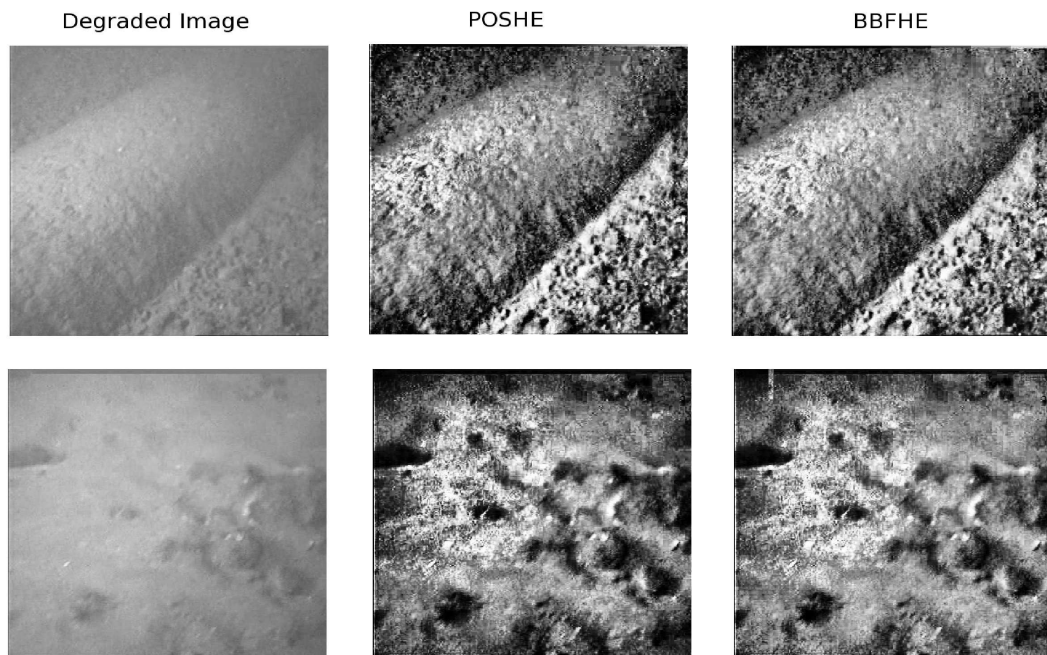


Figure 2.4: From left to right, each row contains the sample of a degraded underwater image, the printed by permission sample of processed images by POSHE and BBFHE methods.

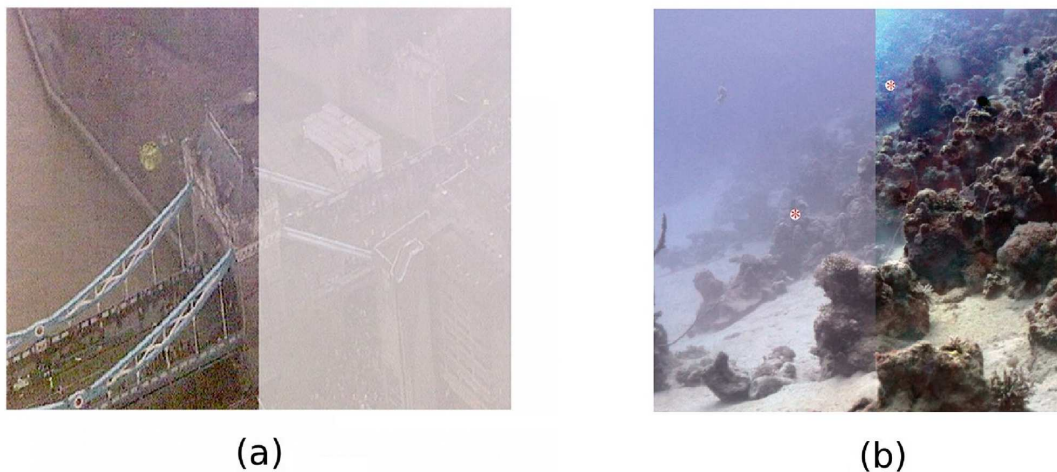


Figure 2.5: The printed by permission sample of a) the degraded image (right side) and improved image (left side) by simple contrast loss method. b) the degraded image (left side) and improved image (right side) by polarisation method.

pixels. This assumption can not be used for images in water, because of the difference of imaging situation between underwater and air medium. The illumination for images in air is the diffused light from the sun, which has an invariant distribution. Also, the optical depth in air is more than images in water. It is in a matter of kilometer in air, whereas in water is in a matter of meter. Moreover, the scattering patterns in water is different with air, because the size of scattering particles are bigger than the particles in air. As a result simple contrast loss is not a suitable method for improving underwater images.

Range-gated and polarisation methods are both spatially variant and can significantly improve underwater images. However, these methods require special equipments for imaging. The printed by permission sample of the processed image by polarisation, which is published in (Schechner & Karpel 2004), is presented in Figure 2.5 (b).

2.3 Other Technical Background

2.3.1 Recursive Gaussian Filter

Gaussian filters are widely used in different areas of image processing and computer vision (Farneback & Westin 2006, S. Tan & Johnston 2003, D. Demigny & Pons 2002, Johnson 2003). Recursive approximation of Gaussian filtering was first introduced by Deriche (1992) and can be performed in the spatial domain (L.J. van Vliet & Verbeek 1998, Zhou 2004). The recursive Gaussian filter is fast. The computation complexity of a recursive Gaussian filter with order N , is $2N$ (L.J. van Vliet & Verbeek 1998), and the computation complexity is independent of the size of the spatial constant, σ . The recursive filter has two steps, forward and backward recursion (Young & van Vliet 1995). The input data, $in_{[n]}$, is first filtered in the forward direction. The output of this result, $w_{[n]}$, is then filtered as in the backward direction, $out_{[n]}$. The forward recursive equation is defined by:

$$w_{[n]} = Bin_{[n]} + \frac{b_1w_{[n-1]} + b_2w_{[n-2]} + b_3w_{[n-3]}}{b_0}. \quad (2.15)$$

The backward recursive filter is defined by:

$$out_{[n]} = Bw_{[n]} + \frac{b_1out_{[n+1]} + b_2out_{[n+2]} + b_3out_{[n+3]}}{b_0}. \quad (2.16)$$

The coefficient b_0, b_1, b_2, b_3 and B are defined by:

$$b_0 = 1.57825 + 2.44413q + 1.4281q^2 + 0.422205q^3, \quad (2.17)$$

$$b_1 = 2.4441q + 2.8561q^2 + 1.26661q^3, \quad (2.18)$$

$$b_2 = -(1.428q^2 + 1.26661q^3), \quad (2.19)$$

$$b_3 = 0.422205q^3. \quad (2.20)$$

$$B = 1 - b_1 - b_2 - b_3. \quad (2.21)$$

$$q = \begin{cases} 0.98711\sigma & \text{if } \sigma \geq 2.5, \\ 3.97156 - 4.14554\sqrt{1 - 0.26891\sigma} & \text{otherwise.} \end{cases} \quad (2.22)$$

2.3.2 Statistical Distribution of Image Texture

There are different distributions used to generate image textures³ such as the Uniform, Gaussian, Poisson, Log-normal and Beta distributions. The Poisson distribution is discrete, whereas the Gaussian, Log-normal and Beta are continuous. However, the Uniform distribution can be either continuous or discrete.

The Poisson and Log-normal distributions have been used as image models in (Pal & Pal 1991, Y. Zimmer & Akselrod 2000). Both the Poisson and the Log-normal distributions are positively skewed⁴. They have a long tail on the right side of the histogram, because the variable is free to vary from 0 to $+\infty$ (Balakrishnan & Nevzorov 2003). The main parameter for the Poisson distribution is the expected number of occurrences (κ) and for the Log-normal distribution are the mean (μ) and standard deviations (σ). Figures 2.6(a) and (b) present a sample of the Log-normal and the Poisson distributions respectively.

The continuous uniform distribution is always used as a reference to a clear enhanced image (Kim & Yang 2006). The Uniform distribution has low kurtosis⁵ as shown in Figure 2.6(c).

The Gaussian distribution is common and simple and is often used in image synthesis (Oakley & Bu 2007, K.V. Mardia & Goitía 2006). The main parameters are the mean (μ) and the standard deviations (σ). The probability density function of the

³Image texture means the distribution of grey values in the image.

⁴Skewness is a measure of the asymmetry of the probability distribution. The distribution is said to be positively skewed, when the mass of the distribution is concentrated on the left and the right tail is longer.

⁵Kurtosis is a measure of whether the data are peaked or flat relative to a normal distribution. A data set with high kurtosis tend to have a distinct peak near the mean and have heavy tails.

Gaussian distribution is bell shaped, with a peak at the mean value. The variable in a Gaussian distribution can vary between $-\infty$ and $+\infty$. A sample of the Gaussian distribution is presented in Figure 2.6(d).

The Beta distribution is constrained to be within the range $[0, 1]$ and has two main positive parameters α_{Beta} and β_{Beta} . The Beta distribution has a great diversity of shapes with different parameters values (Ghahramani 2000), as shown in Figure 2.6(e). It can be seen that for α_{Beta} and β_{Beta} both less than one, the distribution has a U shape. For α_{Beta} and β_{Beta} both greater than one, the graph has a single hump.

In a natural image, the quantised intensity value of pixels is continuous (Weiss & Freeman 2007) and is constrained in the interval $[0, 255]$ or $[0, 1]$. The mean intensity value of the image is low. The image histogram has heavy tails, high kurtosis and is positively skewed (Attewell & Baddeley 2007, Srivastava, Lee, Simoncelli & Zhu 2003).

The probability density function (pdf) of the Gaussian, Poisson and Log-normal are not constrained, but they can be truncated to the range $[0, 1]$. This leads to inaccuracy in the model. Therefore, the Gaussian, Poisson and Log-normal are not the perfect match for image texture. The uniform distribution is not a good choice either, because it has low kurtosis (Attewell & Baddeley 2007), while natural images have high kurtosis (Attewell & Baddeley 2007). In recent studies, it has been shown that the distribution of reflectance within a range of real texture is not Gaussian (Attewell & Baddeley 2007, Weiss & Freeman 2007, Srivastava et al. 2003) and the textures are better described by Beta distributions (Attewell & Baddeley 2007).

In this study the Beta distribution is chosen to represent the texture of each image block. To generate a natural texture with a Beta distribution, it is required to define the value of α_{Beta} and β_{Beta} parameters carefully in order the pdf matches the characterisation of the natural texture.

2.4 Colour

2.4.1 Human Visual System (HVS)

Colour can be defined as an attribute of visual sensation of light on the human eye (Chou & Liu 2008). The perception of surface colour depends on the interaction of light source, non emitting object and the human visual system (Fairchild 2005). Light from a light source with a specific power spectrum illuminates the object and is then

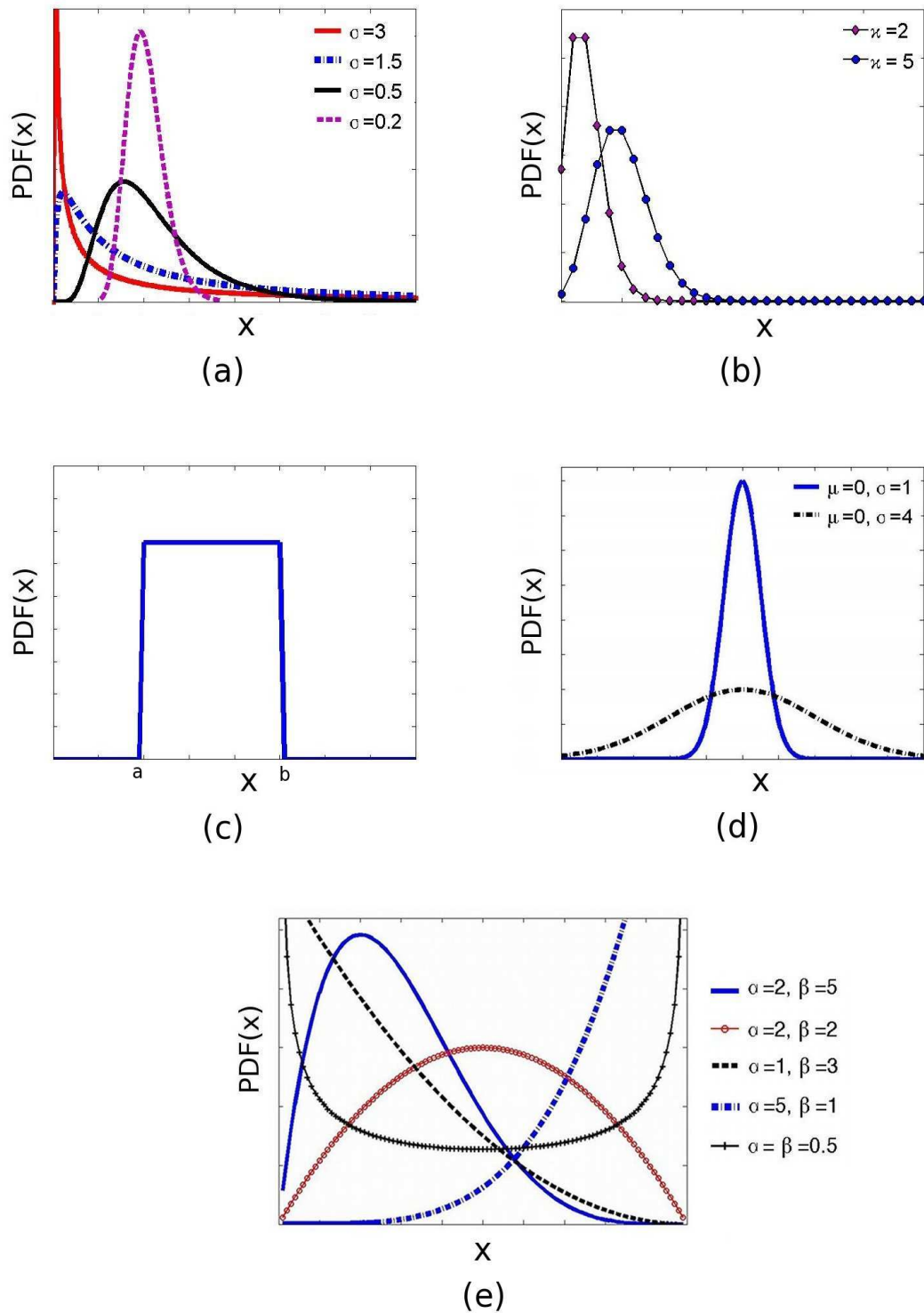


Figure 2.6: Probability Distribution Function of a) the Log-normal distribution with zero mean and different values of σ b) the Poisson distribution with two different parameters value of κ c) the Uniform distribution d) the Gaussian distribution with zero mean and two different values of σ e) the Beta distribution with different values of α_{Beta} & β_{Beta} .

reflected back with a specific spectral power depending on the object reflection properties toward the eye. In the eye, the light is focused by eye lens on the retina, which has a layer of photoreceptor cells. The light stimulates photoreceptor cells with different spectral sensitivities. There are four types of photoreceptors, one type of rod and three types of cones. Three types of cones are known as the S, M and L cones, which are short, medium and long wavelength sensitive respectively. When there is a well-lit condition, the cones are highly active and rods are inactive (Hirakawa & Parks 2005). The neural responses from these three types of cones are combined together and are sent to brain for further processing. Thus, the colour perception of each point from an object is associated with the responses of the three cones.

2.4.2 Colorimetry

Since the development of a variety of colour devices such as colour monitors, scanners, printers, digital cameras and copiers, accurate colour reproduction is demanded (Lee, Ahn & Kim 2000).

The perception of colour is a psychophysical phenomenon, so the colour should be measured in such a way that the results associate with the visual sensation of a normal human. The science and technology of quantifying colour based on the human colour perception is called as colorimetry (Hirakawa & Parks 2005). The basis of colorimetry is the trichromatic theory, which states that three components are sufficient to specify a colour and not the detailed distribution of light energy across the visible spectrum (Krauskopf 2001). The trichromatic theory was developed before it was known that the human vision has three receptors to sense colour.

A colour space specifies a colour by a set of coordinates, which are mostly three dimensional, but four dimensional colour spaces are also used (li Hu, bing Deng & shan Zou 2010). A review of the colour spaces that are relevant to this study is given below.

2.4.3 CIE Colour Spaces

CIE is the abbreviation for "The Commission Internationale de l'Eclairage", which is the primary organisation responsible for standardisation of colour metrics and terminology (Sharma & Trussell 1997). The CIE has defined a system that classifies colour according to the HVS (human visual system). The core of the CIE colour spaces is

CIEXYZ, which was created in 1931. In CIEXYZ the trichromatic theory is mathematically formulated to give tristimulus values (or three coordinates) of X, Y and Z for specifying a colour, C_λ (Kang 2006). The CIE tristimulus specification or CIEXYZ is based on additive colour mixture, which can be presented by

$$C_\lambda = X + Y + Z, \quad (2.23)$$

where X, Y and Z are defined as

$$X = k \int_{\lambda} R(\lambda)S(\lambda)\bar{x}(\lambda)d\lambda, \quad (2.24)$$

$$Y = k \int_{\lambda} R(\lambda)S(\lambda)\bar{y}(\lambda)d\lambda, \quad (2.25)$$

$$Z = k \int_{\lambda} R(\lambda)S(\lambda)\bar{z}(\lambda)d\lambda, \quad (2.26)$$

$$k = \frac{100}{\int_{\lambda} R(\lambda)S(\lambda)\bar{y}(\lambda)d\lambda}. \quad (2.27)$$

$S(\lambda)$ is for the illumination power spectrum, $R(\lambda)$ is the object spectrum, which can be from the reflectance, transmittance or radiance (Kang 2006). The scalar k, which is defined by Equation (2.27), is a normalising constant, which is usually chosen to give a value of 100 for Y. $\bar{x}(\lambda)$, $\bar{y}(\lambda)$ and $\bar{z}(\lambda)$ are the colour matching functions, CMF's. CMF's are a series of functions related to the spectral sensitivities of three cones and are established and presented in CIE publications ⁶.

Metamerism

The representation of colour from the high dimensional spectrum to three dimensional space results in loss of information (Lee et al. 2000). Therefore, two different materials can have identical tristimulus values, while having different reflectance functions. This is known as metamerism in the literature (Nimeroff & Yurow 1965, Foster, Amano, Nascimento & Foster 2006).

Chromaticity

The quality of a color regardless of its intensity is expressed in terms of the chromaticity coordinates (Ohno 2000). The most common chromaticity coordinates is x, y, z ,

⁶<http://www.cie.co.at/main/freepubs.html>

which are defined by

$$x = \frac{X}{(X + Y + Z)}, \quad (2.28)$$

$$y = \frac{Y}{(X + Y + Z)}, \quad (2.29)$$

$$z = \frac{Z}{(X + Y + Z)}. \quad (2.30)$$

The plot of y versus x is commonly used for presenting the chromaticity diagram.

Correlated Colour Temperature

The colour of a light source is measured and expressed by the correlated colour temperature (CCT) (Wyszecki & Stiles 1982, Ohno 2000) in the unit of Kelvin (K). The concept of colour temperature is not related to the temperature of the viewed object. It is derived from the relationship between the temperature of a black body, an imaginary perfect emitter, and the appeared colour of that illuminant (Hernandez-Andres, Jr. & Romero 1999).

As well as colour matching functions, colourimetric illuminants are standardized by the CIE (Sharma & Trussell 1997). The CIE illuminants D65 and D50 are two daylight illuminants corresponding to CCT of 6500 K and 5000 K respectively. The CIE illuminant A represents the CCT of 2856 K and closely approximates the spectra of incandescent lamps (Ohno 2000).

CIELAB

CIELAB is another colour space that the CIE has developed to be used for the specification of colour difference (Fairchild 2005) and (Pointer 2002). CIELAB is perceptually uniform, which means that equal changes in the tristimulus values correspond to equal changes of about the same visual perception (Sharma & Trussell 1997). CIELAB has three coordinates, L^* , a^* , b^* , which are the lightness, approximate redness-greenness, and approximate yellowness-blueness respectively (Fairchild 2005). L^* , a^* and b^* can be found by transformations from CIEXYZ with tristimulus values X, Y and Z as

$$L^* = 116f\left(\frac{Y}{Y_n}\right) - 16, \quad (2.31)$$

$$a^* = 500\left[f\left(\frac{X}{X_n}\right) - f\left(\frac{Y}{Y_n}\right)\right], \quad (2.32)$$

$$b^* = 200\left[f\left(\frac{Y}{Y_n}\right) - f\left(\frac{Z}{Z_n}\right)\right], \quad (2.33)$$

where

$$f(t) = \begin{cases} t^{\frac{1}{3}} & \text{if } t > 0.008856, \\ 7.787t + \frac{16}{116} & \text{otherwise.} \end{cases}$$

X_n , Y_n and Z_n are the tristimulus values of the reference white point.

Colour Difference

Colour difference is expressed as ΔE_{ab} and is measured in CIELAB as the Euclidean distance between their coordinates (Pointer 2002, Ohno 2000). ΔE_{ab} can be presented by

$$\Delta E_{ab} = \sqrt{(\Delta L^*{}^2 + \Delta a^*{}^2 + \Delta b^*{}^2)}. \quad (2.34)$$

The human visual system (HVS) has limited sensitivity in discriminating small differences in colour. The threshold that the human vision perceptually distinguish the difference is known as JND, just noticeable difference, and is around 2.3 (Chou & Liu 2008, Stokes, Fairchild & Berns 1992).

2.4.4 RGB and sRGB Colour Spaces

The RGB colour space is an additive model, where colour is specified in terms of three primary colours, red (R), green (G) and blue (B) associated at wavelengths of 700, 546.1 and 435.8 nm (Sharma & Trussell 1997). The RGB colour space is used in different colour industries such as computer, television, and camera (Yu & Chen 2006, Chaves-Gonzalez, Vega-Rodrigueza, Gomez-Pulidoa & Sanchez-Perez 2010). Basically, each imaging device has its own RGB colour space depending on the spectral sensitivity of its colour sensors (Haeghen, Naeyaert, Lemahieu & Philips 2000). This means that the RGB colour space is device dependent.

The international standard sRGB colour space is first proposed with respect to the response of a reference CRT display by Hewlett-Packard and Microsoft (Anderson, Motta, Chandrasekar & Stokes 1996). The aim of sRGB is to reproduce and share an accurate colour over different imaging devices and internet (Spaulding & Holm 2002).

2.4.5 Multispectral Imaging

The colour of an object is strongly dependent on its spectral reflectance. Colour comparison in the RGB domain is not suitable for a precise colour matching, as the RGB colour space has some limitations (Hardeberg, Schmitt & Brette 2002). An example is device metamerism (Cheung, Westland, Li, Hardeberg & Connah 2005). Multispectral imaging is a solution for an accurate colour comparison (Yamaguchi, Haneishi & Ohyama 2008). Recent improvements in commercial multispectral imaging systems make it possible to use multispectral images in several applications. For example multispectral imaging is applied in colour matching for car industry (Wagner 2007), underwater studies (Zawada 2003), detecting early bruises in fruits (ElMasry, Wanga, Vigneaultc, Qiaoa & ElSayed 2008), dermatology treatment (Roode, Noordmans, Verdaasdonk & Sigurdsson 2006) and the water industry (Govender, Chetty & Bulcock 2007).

Multispectral images are a set of digital bands captured at several narrow spectral bands. Therefore, multispectral images provide the reflectance spectra of a scene for each image pixel (Valero, Nieves, Nascimento, Amano & Foster 2007). There are several techniques that are used to capture multispectral images. For example a monochrome camera with a rotating filter, or a liquid crystal tunable filter (Yamaguchi et al. 2008). The tristimulus values of X, Y and Z from a set of multispectral images can be calculated using equations (2.24) - (2.26) (Westland & Ripamonti 2004).

Chapter 3

Experimental Methodology

Several test images are required for different experiments throughout the thesis. In this chapter, the design of these test images and their preparation are described. Two different types of test images are used, non-constrained and constrained test images as explained in following.

3.1 Non-constrained Test Images

Non-constrained test images are extracted from real underwater video streams, which are kindly provided by the Racal Research (now Thales Research) in UK, and the ADMA company in Abu Dhabi. The rate of image generation is 25 frames/sec and the images are saved in BMP format. The dimensions of the images are $(466 \times 703 \times 3)$ and $(433 \times 601 \times 3)$ for the Thales Research and the ADMA company respectively. The images are gamma encoded. Before processing the images are converted to double-precision in MATLAB and the gamma encoding is reversed by raising each pixel value to the power of 2.2.

3.2 Constrained Test Images

Constrained test images are captured in a controlled underwater environment in the laboratory. A water tank experiment is designed to provide a controlled underwater environment, which resembles a realistic underwater situation. The main objective of water tank experiment is to design the imaging system in such a way that different scenes can be captured, while keeping the level of optical back-scatter unchanged. Optical back-scatter varies with several parameters such as optical depth, wavelength,

size and density of scattering particles in water (McCartney 1976). In the water tank experiment all these parameters are fixed in order to have a constant level of scattering during the imaging.

3.2.1 Water Tank Experimental Setup

Figure 3.1 shows water tank apparatus. A rectangular water tank made of 7mm thick glass with size $0.76m \times 0.38m \times 0.39m$ is chosen to represent the underwater environment. The size of water tank is limited by practical constraints. The tank holds approximately 100 litres of water. Tap water is used to fill the water tank at temperature of 20° with approximate refractive index of 1.33. The tap water represents the clear water condition. Turbid water is prepared by adding scattering particles to the tap water in order to represent scattering situation. The refractive index is assumed to be unchanged when adding scattering particles, as the refractive index is subject only to a very small variation (Bogucki, Domaradzki, Stramski & Zaneveld 1998).

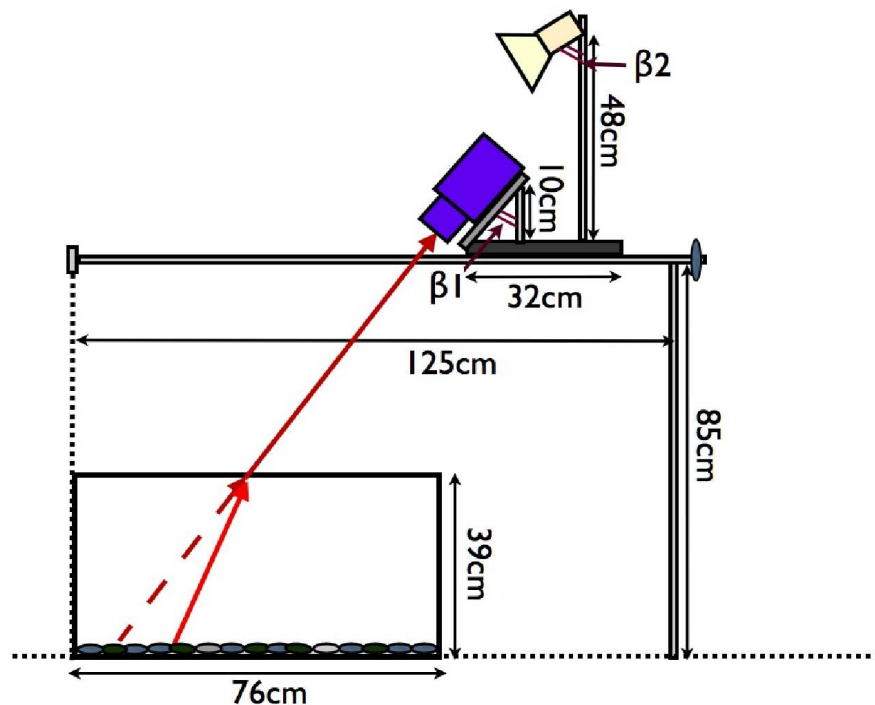


Figure 3.1: The schematic design of water tank experiment.

The scattering particles are chosen to represent marine scattering particles. The scattering in deep water is dominated by particles in the size range $1-20\mu m$ (McCartney

1976, Sullivan, Twardowski, Donaghay & Freeman 2005, Reynolds, Stramski, Wright & Wozniak 2008). The concentration of marine particles varies depending on different parameters such as depth, geographical status and season (Sheldon, Prakash & Sutcliffe 1972, Ahn & Grant 2007). In a previous study (Jiang 2004), emulsion paint was used as a source of scattering particles. Emulsion paint is a water-based paint, mainly Titanium Dioxide (TiO₂), and is used for painting interior or exterior surfaces. The shape of the particles are spherical or near spherical with diameter ranging from $0.2\mu\text{m}$ to $2.5\mu\text{m}$ (Jiang 2004). The volume density of TiO₂ is $4.25\text{g}/\text{cm}^3$.

A translation stage is designed to represent a ROV, that holds both the camera and light source in a specific angle and height relative to the water tank, while translating both camera and light source backward and forward in known steps. Different scenes from water tank can be captured while keeping the optical path constant. Different designs are available for the moving part of the translation stage such as gear, lead screw and step motor. All of these methods can provide accurate smooth movements, but with various levels of complication and cost. The lead screw is the simplest design with low cost and minimum number of parts and is chosen here. The translation stage with lead screw is made of different parts, a lead screw with a turning handle, a screw nut, a pair of base rods, a translation board, camera and light source arm and a wall clamp. To design the lead screw, the thread size is required. The thread size is chosen as 2mm . This allows the capture of more than 100 continuous images over the water tank length. The lead screw is attached with a screw nut to one of the horizontal base rods. A turning handle is attached to the other end of the lead screw, to turn the lead screw and move the translation board linearly. The translation board is made of PVC (Polyvinyl chloride) and has dimensions of $30\text{cm} \times 30\text{cm}$ in order to have enough space for both types of camera bases and the light source arm. The translation board is held with four guider, made of PTFE (Polytetrafluoroethylene), on the base horizontal rods. The horizontal rods are made of steel and are of length 120cm . The size is chosen considering the length of the water tank (76cm) plus the length of the translation bar (30cm) plus some extra space (14cm). The horizontal rods are attached to the wall with a wall clamp on one side and a pair of vertical base rods on the other side. The vertical base rods are made of steel with height of 85cm . The height is chosen to be about half of the height of a person. The light source arm is attached to the translation board, and a threaded hole is provided on the translation board in order to fit the camera bases (both of the cameras have the same threaded).

A halogen lamp is used as the light source. The lamp is 75 watt, 240V and made by

General Electric (GE) company. Water plants, gravel and a resolution (optical) target are used as scene content. There are different standard optical targets available such as the NBS chart and the USAF chart, which are shown in Figures 3.2(a) and (b). NBS

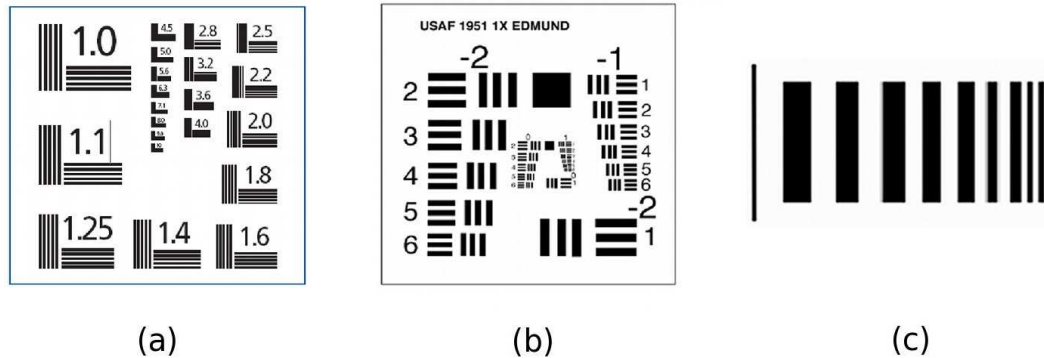


Figure 3.2: Resolution charts. a) The NBS chart b) The USAF chart c) A general resolution chart with low frequency bars.

stands for the National Bureau Standards. The patterns are of black bars on a white background. The bars and spaces are of equal width. The chart is printed on glossy photographic paper. The spatial frequency range is from 1.0 cycle/mm to 18 cycle/mm. Each pattern is made up of two orthogonal groups of five parallel bars. The number written next to each pattern is the corresponding spatial frequency in cycle/mm. USAF stands for the United States of America Air Force. USAF chart is produced by Edmund Optics company¹. This chart is similar to the NBS chart, but each pattern is made up of three bars and contains a much wider range of spatial frequencies. This chart is usually produced on either photographic film or on a thin metal film (e.g. Chrome), but both are placed on a glass substrate. Unlike the NBS chart, the number next to each set of bars in the USAF chart is not a direct measure of the spatial frequency. Also, an optical target can be made by printing parallel black and white bars of different frequencies. In this experiment, an optical target chart bar, which is shown in Figure 3.2(c), is produced on high quality glossy paper in order that it can be used in water. This optical target chart bar has several parallel bars of lower spatial frequencies than is available in the NBS and the USAF charts.

Different cameras are used in the water tank experiment to capture test images in RGB and multispectral formats. As the size of water tank is limited in the laboratory, the camera is placed out of water to keep the water undisturbed when moving the

¹www.edmundoptics.com

camera. The procedure for capturing RGB and multispectral test images are explained as below.

3.2.2 RGB Test Images

A RGB charged coupled device (CCD) camera, the Canon PowerShot Pro90 IS, is used to capture RGB test images. The camera specification is available in Appendix A. Figure 3.3 shows the experimental arrangement to capture RGB test images. The

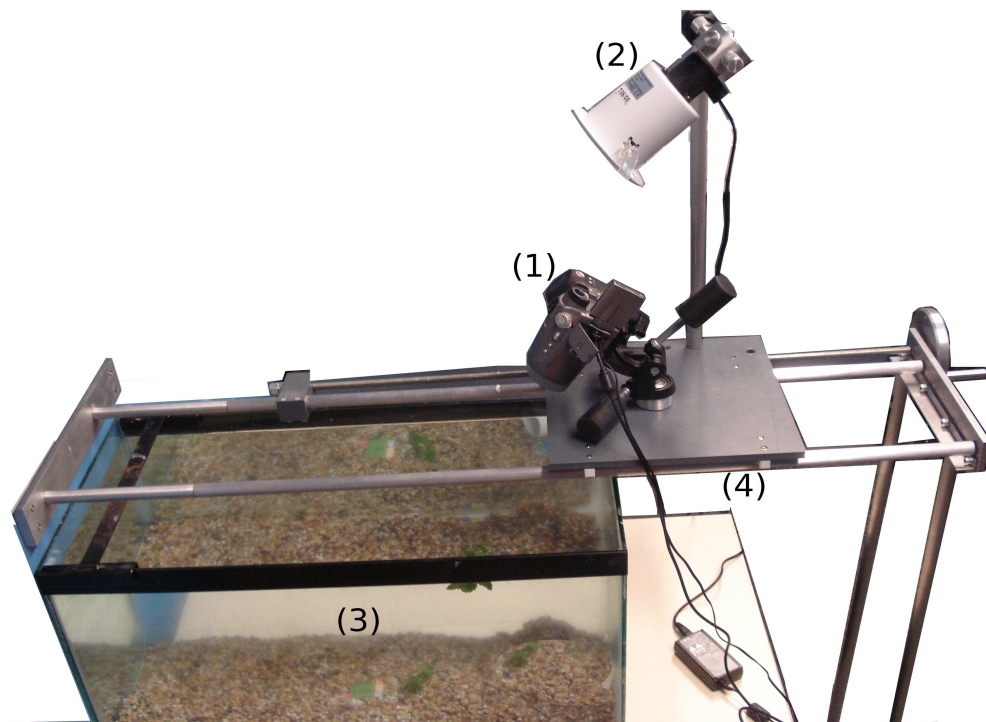


Figure 3.3: The experimental arrangement to capture RGB test images. 1) Canon PowerShot Pro90 IS camera. 2) Halogen lamp 3) Water tank 4) Translation stage.

angle of camera and halogen lamp are set to $\beta_1 = 32^\circ$ and $\beta_2 = 35^\circ$ respectively (β_1 and β_2 are labeled in Figure 3.1). β_2 is slightly more than β_1 in order to prevent heating of the camera. The optical path between the camera lens and the bottom of water tank is 49.75cm , of which 15.3cm is in air and 34.45cm is in water. The camera manual focus is set to between 0.5m and 1m and the shutter speed is set automatically by the camera. The spatial distance between the camera locations for capturing two adjacent images is 2mm .

Different levels of turbid water are made by adding different amounts of emulsion

paint to water, which are described in Table 3.1. Two images are captured for all water turbidity levels, S_0 - S_5 .

Image Series	S_0	S_1	S_2	S_3	S_4	S_5
Water Turbidity (gr/100litres)	0	0.1	0.2	0.3	0.4	0.5

Table 3.1: Different levels of water turbidity for RGB test images.

3.2.3 Multispectral Test Images

In multispectral images, the wavelength can be assumed constant for each monochrome image in narrow spectral band with central wavelength λ . Therefore, by using multispectral images the parameter wavelength is kept constant. A hyperspectral imaging system is used to record multispectral test images. Although a multispectral camera would be sufficient for this experiment, but a hyperspectral camera is chosen instead as it was practically available.

Hyperspectral imaging system consists of a hyperspectral camera, and a filter. The hyperspectral camera is Hamamatsu ORCA-ER C4742-80-12AG, which is a B/W CCD digital camera. The filter is a fast tunable liquid-crystal filter, Varispec, model VIS-10, Cambridge Research & Instrumentation, Inc., Massachusetts, which consists of optics module and electronics controller module. The optics module is mounted in front of the camera and the electronics controller module provides the interface to the host computer. The wavelengths of the light it transmits are electronically controllable, providing rapid, vibrationless selection of any wavelength in the visible (VIS) and near-infrared (NIR) tuning ranges. The filter can be set to 10nm or 20nm spectral bandwidth. Figures 3.4(a) and (b) shows the hyperspectral camera and the optics module of the filter, which is mounted in front of the camera, respectively. Details of the hyperspectral camera specifications are given in Appendix A. Figure 3.4 shows the experimental arrangement to capture multispectral test images. The angle of multispectral camera and halogen lamp are set to $\beta_1 = 42^\circ$ and $\beta_2 = 45^\circ$ respectively. The optical path between the camera lens and the bottom of water tank is 122.08cm, of which 77cm is in air and 45cm is in water. The camera aperture and focus are set to 4.0 and 1.15 respectively.

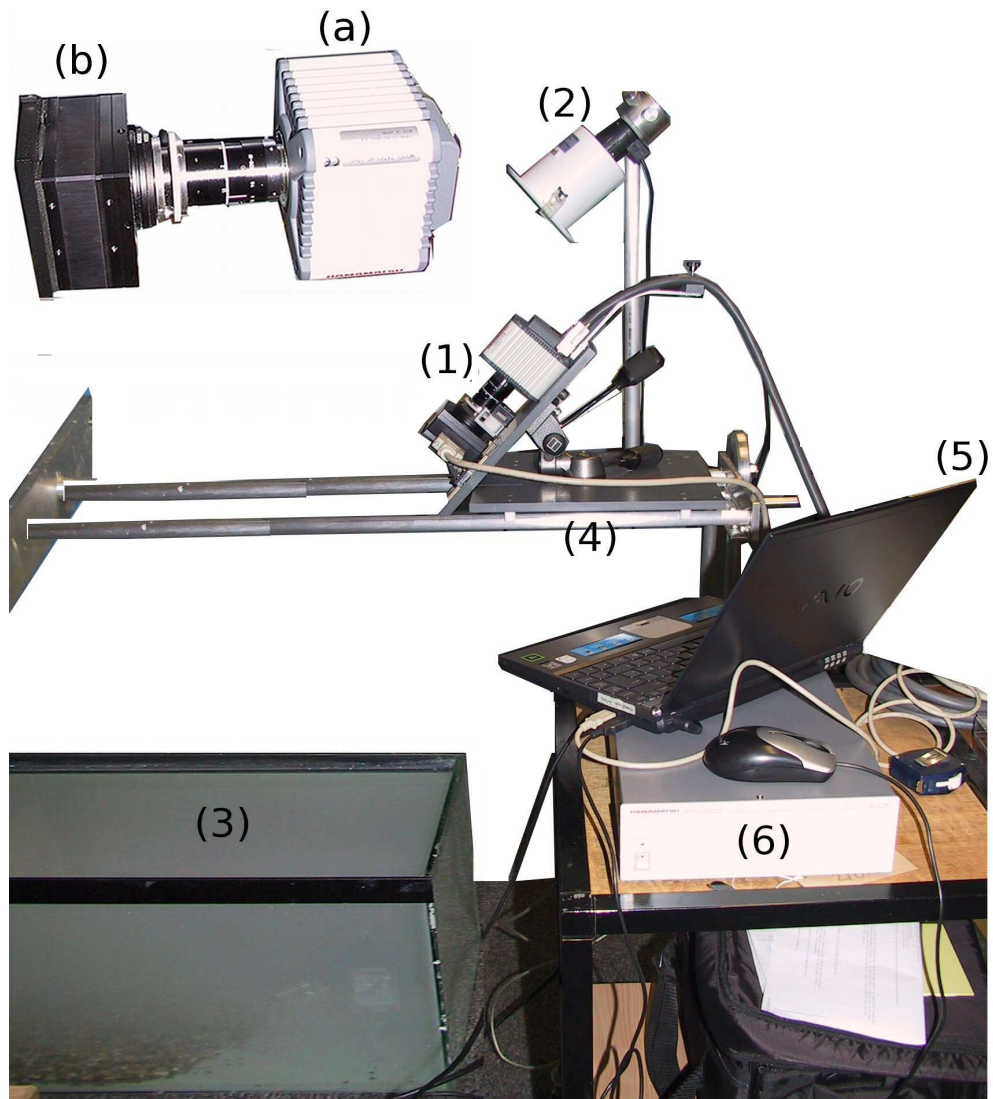


Figure 3.4: The experimental arrangement for capturing multispectral images. 1-a) Hyperspectral Camera, 1-b) VariSpec optics, 2) Halogen lamp, 3) Water tank, 4) Translation stage, 5) Host computer, 6) The electronics controller module.

Four series of multispectral test images are captured in different water conditions at 20° water temperature, as described in Table 3.2. Each series contains 10 continuous monochrome images in size (1024 × 1344) at visible spectrum [400nm 720nm] over a narrow spectral band of bandwidth 10nm. The bandwidth of 10nm provides sufficient accuracy for most colour spectra (Sharma & Trussell 1997). The spatial distance between two camera locations for capturing two adjacent images is 4mm. Also a dark image is captured, when the camera is covered completely by a black cloth at visible spectrum [400nm 720nm] in a narrow spectral band of bandwidth 10nm to estimate for the dark current noise and at respective wavelengths.

Before processing multispectral images, the dark current noise is subtracted from the image to remove any biased which is due to the dark current noise (Zawada 2003). Then, the images are converted from 12 bits to 8 bits.

Image Series	T_0	T_1	T_2	T_3
Water Turbidity (gr/100litres)	0	0.3	0.7	0.9

Table 3.2: Different levels of water turbidity for capturing multispectral test images.

Chapter 4

Degradations in Underwater Images

Previously, it has been shown that optical scattering causes underwater images to be degraded in terms of both overall contrast and spatial resolution. Contrast loss is mainly due to the effect of optical back-scatter, L_3 , and resolution loss is mainly due to the effect of optical forward-scatter, L_2 as explained in Section 2.1.3. In order to improve a degraded underwater image, the main degradation effect must be mitigated. Now, the question is which of these two effects, contrast loss or resolution loss, has the biggest degradation effect in an underwater image? To answer this question, the impact of contrast loss and resolution loss should be compared in a the practical underwater situation.

This chapter is structured as follows. Section 4.1 illustrates the impact of L_2 and L_3 on image degradation. In Section 4.2 an experiment is conducted to characterise the effect of L_2 and L_3 in practical underwater conditions. It is shown experimentally that contrast loss is the dominant degradation effect compared to resolution loss.

4.1 The Impact of L_2 and L_3 in Image Degradation

According to the image geometry shown in Figure 1.2, the intensity of an underwater image pixel is composed from three components, L_1 , L_2 and L_3 , which are direct ($A_\lambda(x, y)$), forward-scatter ($FS_\lambda(x, y)$) and back-scatter ($BS_\lambda(x, y)$) components respectively. Hence, an underwater image, $Im_\lambda(x, y)$, at a spatial pixel position (x, y) and a specific wavelength λ can be presented as shown in Equation (4.1) (Trucco & Olmos-Antillon 2006, Yu & Liu 2007).

$$Im_\lambda(x, y) = A_\lambda(x, y) + FS_\lambda(x, y) + BS_\lambda(x, y). \quad (4.1)$$

It was explained in Chapter 2 that L_1 contains the image information, while L_2 and L_3 individually degrade image quality in forms of resolution loss and contrast loss respectively. A target bar chart in a non scattering condition (e.g. air medium) and its corresponding line plot are shown in Figure 4.1. This bar chart is used to show the form of each component in a scattering medium.

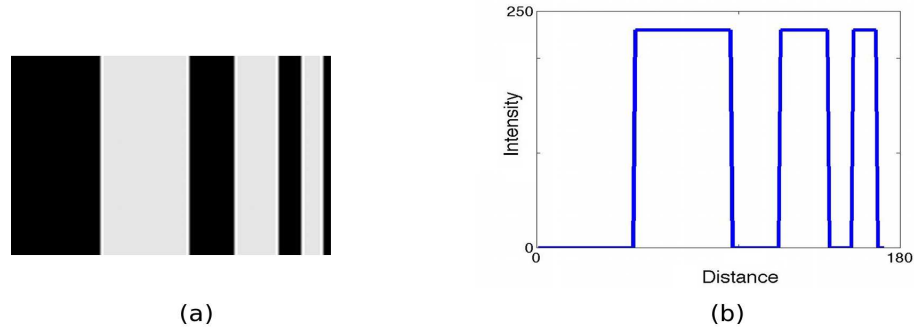


Figure 4.1: (a) A target bar chart in a non scattering medium. (b) The line plot of the target bar chart.

A degraded image structure for the bar chart is shown in Figure 4.2. In this figure, it is shown how each component, L_1 , L_2 and L_3 , contributes to form a degraded image. In this example the values of L_1 , L_2 and L_3 , are calculated utilising Equations (2.1), (2.5) - (2.7) using parameters based on typical conditions. A Gaussian filter with standard deviation relative to θ is used to model the effect of image blur for L_2 (Figure 4.2(d)). The line-plot of the intensity of a degraded image is shown in Figure 4.2(e). This is the combination of the three components, L_1 , L_2 and L_3 . Line plots of the intensity of components L_1 , L_2 and L_3 are individually shown in Figures 4.2(a), (b) and (d) respectively. Figure 4.2(c) shows only the effect of contrast loss, which is the combination of L_1 and L_3 . Comparing Figures 4.2(c) and (d), it can be seen that the two degradation effects, contrast loss and resolution loss, are different. In contrast loss the spatial fluctuations caused by the bar chart pattern are clearly visible, and just the absolute intensity is increased. However, with resolution loss, the transitions are smoothed with respect to the original bar chart image.

The dominant degradation effect depends on the relative contribution of each component. Two different situations, high L_2 , giving mostly resolution loss, and high L_3 , giving mostly contrast loss, are illustrated in Figures 4.3(a) and (b) respectively. Situations with mostly resolution loss would arise when there are big scattering particles and a short optical depth. Conversely situations with mostly contrast loss would arise

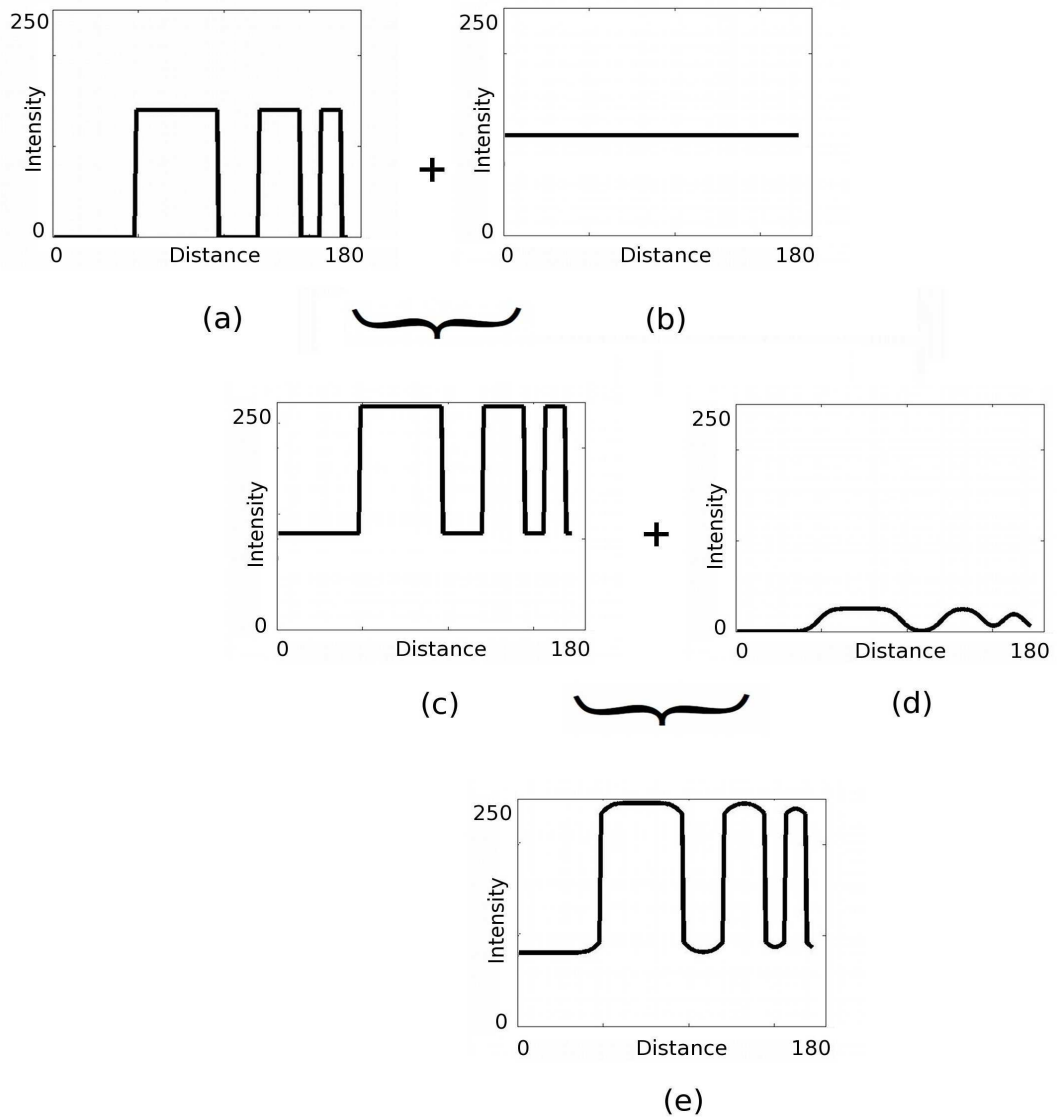


Figure 4.2: The structure of a degraded underwater image. The values of optical distance and extinction coefficient are $R = 1m$ and $\beta = 0.5m^{-1}$. (a) Direct component, L_1 . (b) Back-scatter component, L_3 . (c) The combination of direct and back-scatter components. (d) Forward-scatter component, L_2 . (e) The combination of three components, which represents the degraded underwater image line plot.

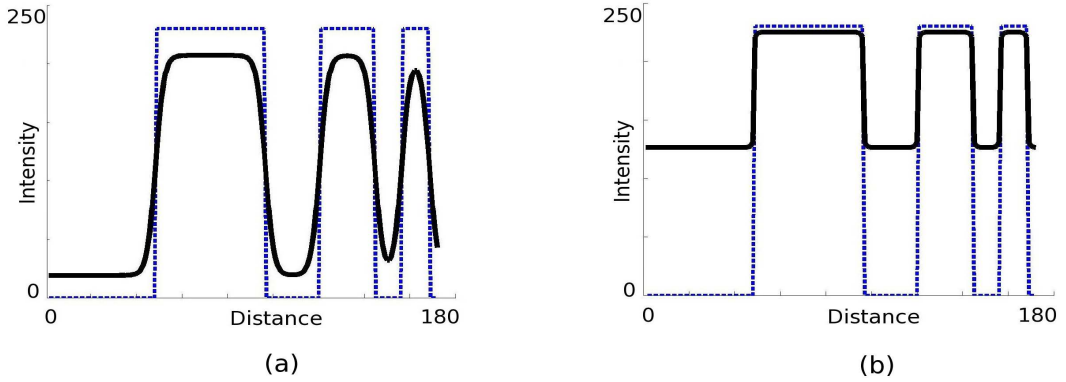


Figure 4.3: The line plot of original image (dotted line) and the line plots of two degraded images (solid line) with two different degradation effects (a) Resolution loss (b) Contrast loss.

when there are small scattering particles and long optical depth.

4.2 Experimental Characterisation

The aim of this section is to compare experimentally the effects of contrast loss and resolution loss in real underwater conditions in order to find which of these two effects causes the most significant degradation effect. It is not possible to measure these two effects separately in real situations. Therefore, an experiment is designed to provide a controlled underwater environment in order to have the scattering condition similar to a real underwater environment such as seawater, ocean in the laboratory. The experimental setup is as explained in Section 3.2.2.

Contrast loss strongly depends on the product βR as explained by Equation (2.7). To reconstruct the same level of contrast loss, the product βR in this experiment should be the same as the value of βR in real condition.

The optical depth in this experiment is shorter than that in real imaging conditions. It is around 35cm in this experiment, while in real underwater imaging it is at least 2 meters. Therefore, a higher value of β is used to compensate for the shorter range of R . Higher β can be easily achieved by having higher particles concentrations (density) as shown in Equation (2.3).

As explained in Section 2.1.3, resolution loss (image blur) depends on the amount of misplacement, and the misplacement depends on the scattering angle, θ_{max} , and optical depth, R . Assume, that misplacement $Y1$ is caused by the scattering particles with

scattering angle of θ_1 and in distance of R_1 . For a shorter distance of R_2 , ($R_2 < R_1$), the scattering angle, θ_2 , should be wider ($\theta_2 > \theta_1$) in order to have same amount of misplacement, and as a result same level of image blur. The scattering angle θ_{max} has inverse relation with particle diameter in a specific wavelength as shown in Equation (2.4). Hence, for a wider θ_{max} , a smaller scattering particle diameter is required.

In this experiment the optical depth in scattering medium is about 35cm, which is at least ten times shorter than the optical path in real situation. Therefore, particle size and density are selected at least ten times smaller and ten times higher in density than in the real situation respectively. The scattering particles in seawater and ocean are in size $1\mu m - 20\mu m$ (McCartney 1976), as a result the particles in this experiments should be selected in size range of $0.1\mu m - 2\mu m$. Emulsion paint (EP) is used as scattering particles in this experiment. Emulsion paint particles were used as scattering particles in previous studies (McNeil, Hanuska & French 2001, Jiang 2004) as well.

The density of particles varies in different seas and oceans. Yura (1971) gives an estimated value of $\beta = 0.1m^{-1}$ for seawater at $\lambda=480nm$. If $R \simeq 4m$, an estimated value of the product βR in real condition and in 480nm would be 0.4.

To provide different particles density in this experiment, different values of βR are used by adding different amounts of particles weight to water. Table 3.1 presents different densities of emulsion paint particles that are used to provide different levels of turbidity, $S_0 - S_5$, in this experiment. The estimated value of βR for S_5 is calculated as $\beta R \approx 0.49$ at S_5 . This is found by using $\beta = 1.4132(m^{-1})$ at 0.5 gr/100litres of emulsion paint at green colour channel from previous work (Jiang 2004) and considering $R=35cm$. The value of βR in real turbid water is $\beta R = 0.4$. Therefore, the maximum value of $\beta R \approx 0.49$ at S_5 in this experiment is higher than $\beta R = 0.4$ in real turbid water condition. An optical target, shown in Figure 4.4, is used to measure the con-

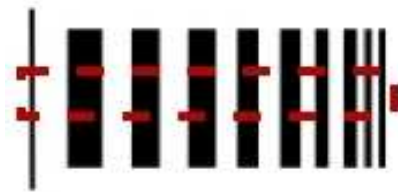


Figure 4.4: Experimental optical target.

trast and spatial resolution in different conditions. Contrast is calculated by Equation (2.8). Image spatial resolution quantifies how close lines can be resolved in an image.

The image resolution can be measured using the modulation transfer function (MTF) measured using an optical target. The MTF at each line pair with specific frequency f can be calculated by

$$MTF_f = \frac{c_f}{c_{ref}} \times 100, \quad (4.2)$$

where c_f is the contrast of a line pair at a specific frequency f , and c_{ref} is the contrast of the lowest frequency line pair. The resolution of different images can be compared by the value of the bandwidths estimated from the MTF chart. The frequency in which the MTF chart reaches to $\frac{100}{\sqrt{2}}$ is the image bandwidth (100 is the maximum value at the MTF chart and $\frac{1}{\sqrt{2}}$ is for when the power gets to 50%).

4.2.1 Results and Conclusion

Six images are captured from optical target at six water conditions, S_0 to S_5 . The first image is taken in clear water condition, S_0 , and the rest of the images are taken in low to high level of water turbidity, S_1 to S_5 . Images corresponding to the middle

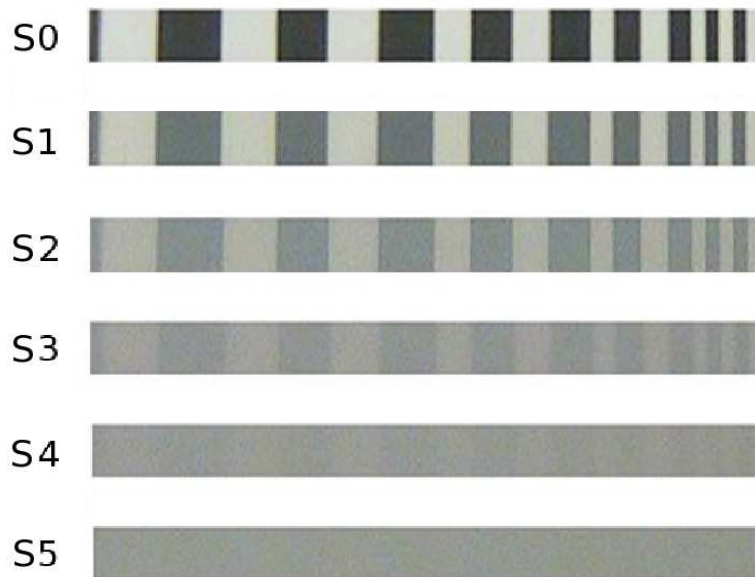
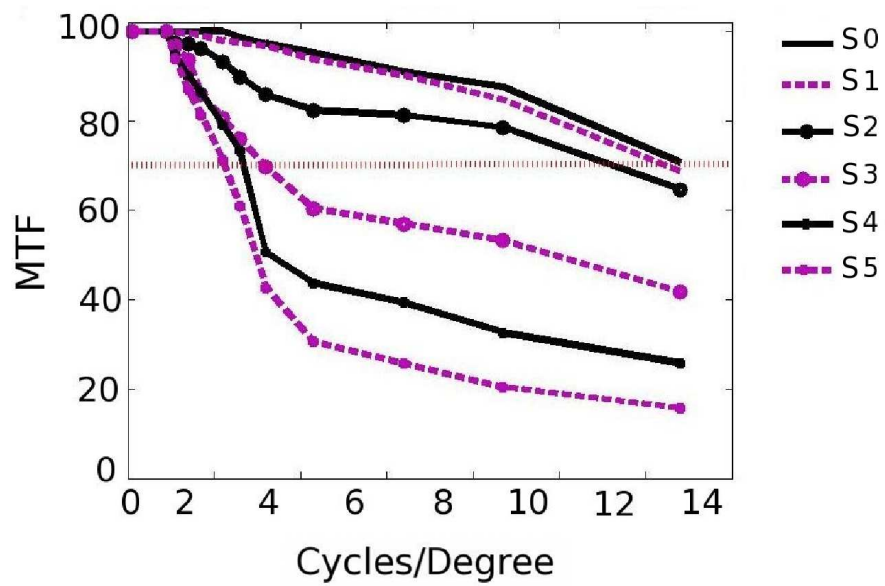


Figure 4.5: Sample images from the target bar at different water conditions. S_0 is for clear water and S_1 - S_5 are for low to high water turbidity respectively.

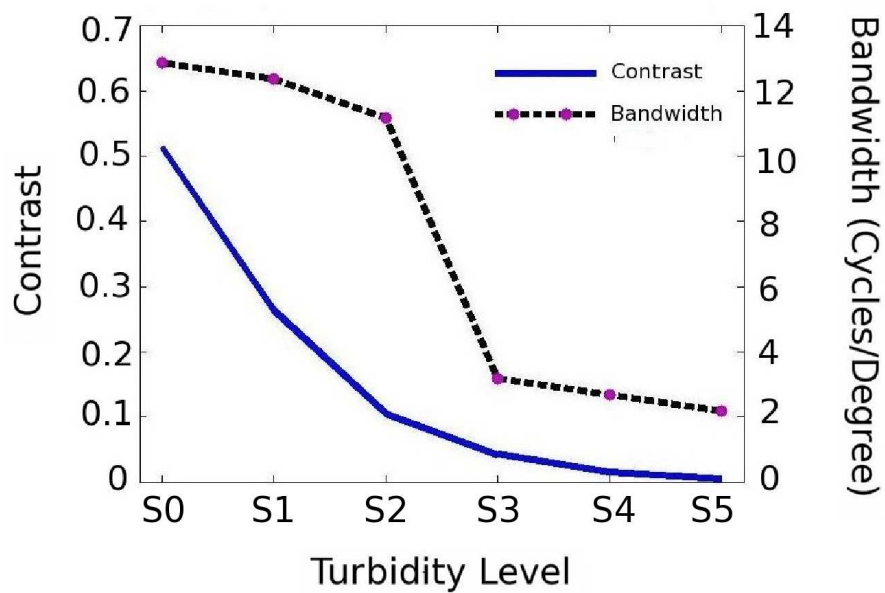
part of the optical target, as defined by the red dashed line in Figure 4.4, are shown in Figure 4.5 for different water conditions. It can be seen that as the water turbidity is increasing, the image quality is decreasing.

The image contrast is calculated for different levels of turbid water by using Equation (2.8). The image bandwidths at different levels of water turbidity are found from the correspondence MTF charts, which are presented in Figure 4.6(a). Figure 4.6(b) presents the contrast and bandwidth with respect to different levels of water turbidity by the solid line and the dashed line respectively. The image contrast starts to decrease from S_1 and becomes very low at S_5 . For example the image contrast at S_3 is around 10% of the image contrast in clear water, S_0 . The plot of bandwidth shows that the image resolution does not change significantly at S_1 and S_2 . The image bandwidth starts to decrease from S_3 , where the bandwidth drops to nearly 20% of the bandwidth of S_0 . Comparing the plots of contrast and bandwidth, it can be seen that the contrast loss is evident for all levels of water turbidity, whereas the resolution loss can not be detected for S_1 and S_2 . Therefore, for low level of water turbidity the dominant degradation effect is contrast loss. For higher levels ($> S_3$) both contrast loss and resolution loss are evident. However, by the time the resolution loss is significant, the image contrast is already less than 10%. In this situation, even if the image could be compensated for the effect of resolution loss, the image quality still remains poor due to very low contrast.

In summary the results show that of the two degradation effects, contrast loss and resolution loss, the contrast loss is the main problem in underwater images. As a result, the quality of an underwater image should be improved by compensating the effect of contrast loss.



(a)



(b)

Figure 4.6: (a) The MTF charts for different levels of turbid water. (b) The plot of contrast and bandwidth with respect to the turbidity level.

Chapter 5

Underwater Image Model

The model of a degraded underwater image is given by Equation (1.1). In this chapter the validity of the image model is investigated experimentally. This chapter is structured as follows. Section 5.1 is the explanation of the forward model of an underwater image. In Section 5.2, it is shown that image recovery is possible using an inversion procedure. Section 5.3 is concerned with the design of the water tank experiment. It includes the experimental design, error analysis and experimental procedures, as well as experimental results.

5.1 Forward Model of Image Formation

The formation of an image in a turbid medium, which only has contrast loss problem, is reviewed in this section. In a scattering medium, the intensity of a degraded image at pixel spatial position (x, y) and at particular wavelength (λ) is denoted by $Im_\lambda(x, y)$. This can be represented as the sum of two components, the actual image contribution from the object, $A_\lambda(x, y)$, and the optical back-scatter, $B_\lambda(x, y)$ (Tan & Oakley 2001).

$$Im_\lambda(x, y) = A_\lambda(x, y) + B_\lambda(x, y). \quad (5.1)$$

In diffuse light conditions $A_\lambda(x, y)$ and $B_\lambda(x, y)$ can be calculated from

$$A_\lambda(x, y) = C_0 R_\lambda(x, y) \exp(-\beta_\lambda(x, y)R), \quad (5.2)$$

$$B_\lambda(x, y) = C_0(1 - \exp(-\beta_\lambda(x, y)R)), \quad (5.3)$$

where C_0 is the illumination radiance, $R_\lambda(x, y)$ is the scene reflectance function, $\beta_\lambda(x, y)$ is the extinction coefficient and R is the distance from the camera to the object (Tan & Oakley 2001).

The Taylor series expansion of $\exp(x)$ can be written

$$\exp(x) \approx 1 + x + \frac{x^2}{2!} + \dots + \frac{x^n}{n!}. \quad (5.4)$$

When $0 < x \ll 1$, then $\exp(x) \approx 1 + x$.

In moderate scattering conditions $0 < \beta_\lambda(x, y)R < 1$, the approximations of equations (5.2) and (5.3) are

$$A_\lambda(x, y) = C_0 R_\lambda(x, y)(1 - \beta_\lambda(x, y)R), \quad (5.5)$$

and

$$B_\lambda(x, y) = C_0(1 - (1 - \beta_\lambda(x, y)R)), \quad (5.6)$$

$$= C_0 \beta_\lambda(x, y)R. \quad (5.7)$$

Combining Equations (5.5) and (5.7), $Im_\lambda(x, y)$ can be written as

$$Im_\lambda(x, y) = C_0 R_\lambda(x, y)(1 - \beta_\lambda(x, y)R) + C_0 \beta_\lambda(x, y)R, \quad (5.8)$$

$$= C_0(\beta_\lambda(x, y)R + (1 - \beta_\lambda(x, y)R)R_\lambda(x, y)). \quad (5.9)$$

When an image is captured by camera, the camera introduces a scaling factor. Therefore, the image from the camera, $I_\lambda(x, y)$, has the form

$$I_\lambda(x, y) = \zeta Im_\lambda(x, y), \quad (5.10)$$

where ζ is a scaling constant introduced by the camera. Combining Equations (5.9) and (5.10), $I_\lambda(x, y)$ can be written as

$$I_\lambda(x, y) = \zeta C_0(\beta_\lambda(x, y)R + (1 - \beta_\lambda(x, y)R)R_\lambda(x, y)). \quad (5.11)$$

To simplify this expression the first term on the left hand side in Equation (5.11), $\zeta C_0 \beta_\lambda(x, y)R$, is written as $b_\lambda(x, y)$ and the scaling component, $\zeta C_0(1 - \beta_\lambda(x, y)R)$,

is written as $a_\lambda(x, y)$. Equation (5.11) then becomes

$$\boxed{I_\lambda(x, y) = b_\lambda(x, y) + a_\lambda(x, y)R_\lambda(x, y)}, \quad (5.12)$$

where $b_\lambda(x, y)$ is a parameter representing optical back-scatter and $a_\lambda(x, y)$ is a parameter representing the combined effects of camera gain, illumination and extinction. Equation (5.12) represents the simplified forward model of an image in a scattering medium.

5.2 Image Recovery (Inversion Model)

Recovery of the estimated value of the content of an image pixel, $\hat{I}_\lambda(x, y)$, can be achieved by rearranging Equation (5.12) to give

$$\hat{I}_\lambda(x, y) = \frac{I_\lambda(x, y) - b_\lambda(x, y)}{a_\lambda(x, y)}. \quad (5.13)$$

5.3 Water Tank Experiment

Before starting the experimental design and procedure, an explanation is given about the Fixed Path image vector and the regression method.

5.3.1 Fixed Path

In some imaging situations the optical path remains approximately constant and only the scene reflection varies. For example, assuming a flat seabed, when an underwater camera is mounted on a Remotely Controlled Vehicle (ROV) and translated over the sea bed at a constant height and angle. This situation is illustrated in Figure 5.1. It can be seen that for each camera location, the angle and height of camera remain constant at β_1 and h_1 respectively. Therefore, for each image pixel position the optical path remains constant in different camera locations. The optical path for image pixel $p(x, y)$ at different imaging locations, (1), (2), ..., (n), is d_1 . In this special case it is possible to obtain a vector of intensity values for each image pixel coordinates that correspond to different camera locations. This vector will be referred to as a fixed path intensity vector. Figure 5.2 represents the image pixel coordinates for a sample of a fixed path intensity vector, $V(p(x, y, 1), p(x, y, 2), \dots, p(x, y, n))$. This imaging situation may be simulated in a laboratory environment by using a water tank.

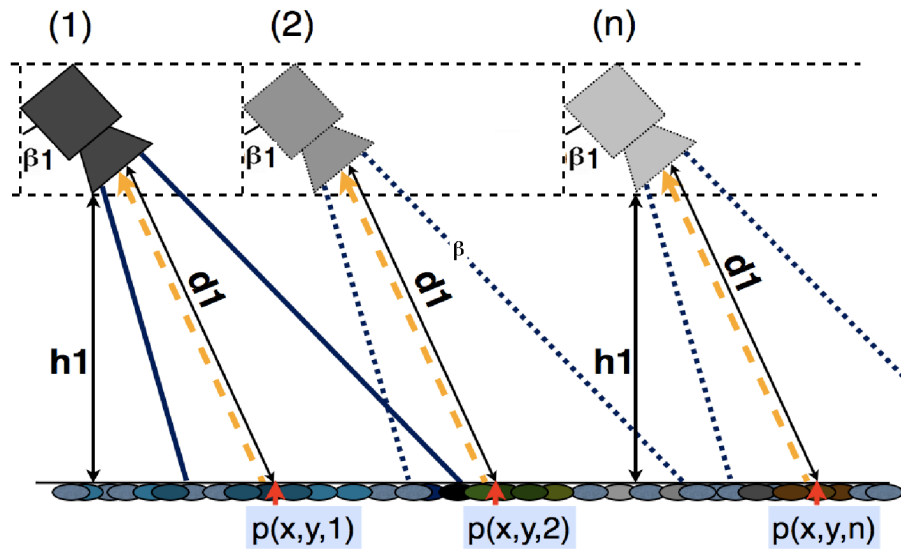


Figure 5.1: The camera position is fixed at angle of β_1 and height of h_1 for capturing images from different locations of seabed. The optical path remains constant at d_1 while the seabed pattern is changing for different camera locations.

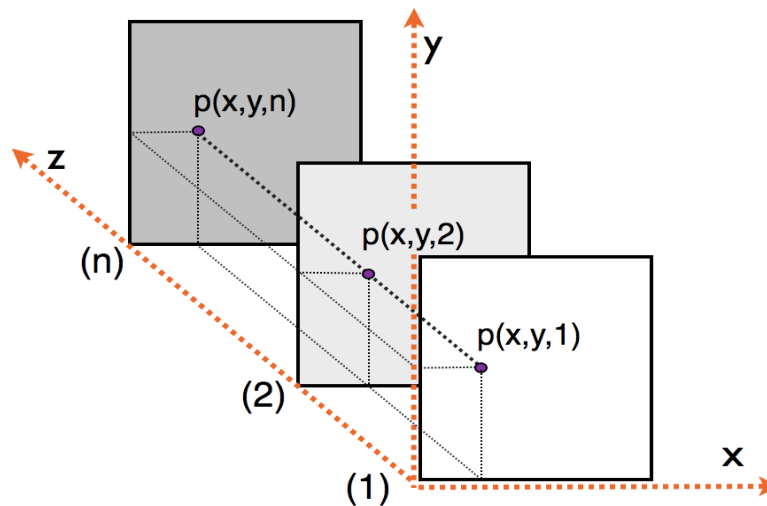


Figure 5.2: The schematic form of an image pixel coordinates for a sample of Fixed Path Vector, $v(p(x, y, 1), p(x, y, 2), \dots, p(x, y, n))$.

5.3.2 Regression Method

Assume that there are two fixed path vectors available, where the first one, V_i , is for the scene intensity of a constant scattering medium and the second one, V_f , is for the intensity of the corresponding scene from a non scattering medium. According to Equation (5.12), the regression line (best fitting line) of the plot of V_i versus V_f has the slope and Y-intercept of $a_\lambda(x, y)$ and $b_\lambda(x, y)$ respectively.

Therefore, the estimated values of $a_\lambda(x, y)$ and $b_\lambda(x, y)$ at any point (x, y) can be obtained from this regression line without having any information about the physical properties of the scene. This estimation method is referred to as the Regression method in this work. The certainty of the regression estimation can be found by calculating the prediction error (σ_{PE}^2) (Gilchrist 1984):

$$\sigma_{PE}^2 = \frac{e^2}{(n - 2)}, \quad (5.14)$$

where n is the number of samples and e is the difference between the actual and predicted value:

$$e = I_\lambda(x, y) - \hat{I}_\lambda(x, y). \quad (5.15)$$

To investigate the linear forward model of an underwater image, two Fixed Path vectors, V_i and V_f , taken from real underwater images, are required. The imaging situation for the Fixed Path vector requires a controlled underwater environment. Therefore, a water tank experiment is designed to capture underwater images for the Fixed Path vector analysis.

5.3.3 Experimental Design

The main objective of water tank experiment is to design the imaging system in such a way that different scenes can be captured, while keeping the level of optical back-scatter unchanged. It is explained in Chapter 4 that optical back-scatter varies with several parameters such as optical depth, wavelength, size and density of scattering particles in water. In the design of water tank experiment it is important to keep all these parameters unchanged, in order to have a constant optical back-scatter during the imaging.

The experimental arrangement for multispectral images, is described in Section 3.2.3. The intensity value of one pixel in a specific position, (x, y) , from various images of turbid water can provide the vector information $V_i(x, y)$. We also need the

information of the scene reflectance for corresponding clear image pixels to give the vector $V_f(x, y)$. This can be done either by taking pictures of the same camera locations from water tank with no water, or water tank filled with tap water only (clear water condition). The latter is chosen, because the optical path for a specific camera location changes when the water tank is empty. The change in optical path causes a path difference of about 15.55cm (equivalent here to 1920 pixels) in scene x-y position, which leads to significant image registration error. Moreover, the refractive index is subject only to a very small variation when adding scattering particles to water (Bogucki et al. 1998). The refractive index is assumed to be unchanged when adding scattering particles.

5.3.4 Experimental Errors

Although the experiment is designed in such a way to record the pixels intensity values accurately, there are some unavoidable errors in the imaging system which cause variations in measured pixel intensity. Therefore, the underwater image model of Equation (5.12) can be written as

$$I_\lambda(x, y) = b_\lambda(x, y) + a_\lambda(x, y)F_\lambda(x, y) + err, \quad (5.16)$$

where err is the total experimental error. There are two main sources of error in this experiment, camera noise, N_{camera} , and image registration error, N_{ImReg} .

$$err = N_{camera} + N_{ImReg}. \quad (5.17)$$

Camera Noise

A CCD (charge-coupled device) digital camera converts the photons coming to camera sensors to electrons and then to bits (Liu, Szeliski, Kang, Zitnick & Freeman 2008). Noise can be introduced during each of these steps of acquisition and conversion. A general model of CCD camera noise, N_{camera} , can be given by

$$N_{camera} = N_D + FPN + N_R + N_S + N_Q, \quad (5.18)$$

where N_D is for the dark current noise, FPN is for the fixed pattern noise, N_R is for the read out noise, N_S is for the shot noise and N_Q is for the quantization noise (Healey & Kondepudy 1994).

Dark current noise occurs due to current leakage in each pixel of the CCD sensor and is constant over time. Fixed pattern noise is the non uniformity of the dark current noise in pixel geometry arising in sensor fabrication. Dark current noise and fixed pattern noise can be corrected by subtracting the dark image from the captured image (Lukas, Fredrich & Goljan 2006). The dark image is obtained by capturing an image when the camera lens is fully blocked (no light reaches to camera sensors).

Readout noise is added to the signal when reading out charges collected by the pixel (Reibel, Jung, Bouhifd, Cunin & Draman 2003) and has Gaussian distribution (Withagen, Groen & Schutte 2007).

Shot noise arises because the number of photons reach to camera sensors at a specific time are different, even when the time-averaged intensity is identical. The distribution of photons in a specific time follows the Poisson distribution (Irie, McKinnon, Unsworth & Woodhead 2008). In the Poisson distribution, when the number of counts is high, the variance is equal to mean, $\sigma^2 = \mu$.

Quantization noise is introduced by the analog-to-digital conversion (ADC) and has a uniform distribution (Withagen et al. 2007).

Camera noise has zero mean ($\mu = 0$) and is represented by the root square of variance, $\sigma_{N_{camera}}$. However, to calculate the sum of different sources of noise, the values are added in variance (Reibel et al. 2003). The calculation of the total camera noise $\sigma_{N_{camera}}^2$ is presented in Equation (5.19).

$$\sigma_{N_{camera}}^2 = \sigma_{N_D}^2 + \sigma_{FPN}^2 + \sigma_{N_R}^2 + \sigma_{N_S}^2 + \sigma_{N_Q}^2, \quad (5.19)$$

where $\sigma_{N_D}^2$, σ_{FPN}^2 , $\sigma_{N_R}^2$, $\sigma_{N_S}^2$ and $\sigma_{N_Q}^2$ are for dark current noise, fixed pattern noise, readout noise, shot noise and quantization noise respectively.

Image Registration Error

Image registration error is a common problem when two images are captured from the same scene at different times (Robinson & Milanfar 2004), different viewpoints or with different sensors (Zitova & Flusser 2003). Image registration problem can be during registration process or geometric registration process (Moller & Posch 2008).

The error due to the registration process depends on the CCD sensors fabrication. The error due to the geometric registration process exists, because of the accuracy level in translation steps. As the image resolution is high, even a very small inaccuracy in translation steps may cause the pixel to be misregistered. Figure 5.3 illustrates the

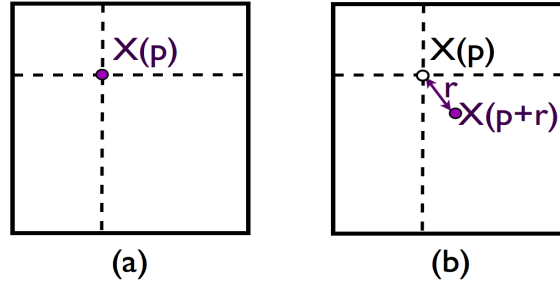


Figure 5.3: The pixel $X(p)$ in (a) is misregistered to $X(p+r)$ in (b). The registration error is r pixel position.

effect of image registration error. Pixel $X(p)$ in image (a) is misregistered in image (b) by r distance and has the new spatial position, $X(p+r)$.

In this experiment, the geometric registration is the main source of the image registration error. The question is how much variation is introduced to the pixel intensity due to the misregistration of r spatial distance. A statistical tool is utilized to analyse the image pixels and measure for the amount of pixel intensity variation, σ_{Reg}^2 . This can be calculated by the expected value of the square difference of the intensity between the two pixels, $X(p)$ and $X(p+r)$, as presented in Equation (5.20).

$$\sigma_{Reg}^2 = E[(X(p) - X(p+r))^2]. \quad (5.20)$$

Equation (5.20) can be expanded as

$$\begin{aligned} \sigma_{Reg}^2 &= E[(X(p) - X(p+r))^2], \\ &= E[X(p)^2 + X(p+r)^2 - 2X(p)X(p+r)], \\ &= E[X(p)^2] + E[X(p+r)^2] - 2E[X(p)X(p+r)]. \end{aligned}$$

As X is a stationary image, $E[X(p)^2] = E[X(p+r)^2]$. Therefore,

$$\boxed{\sigma_{Reg}^2 = 2(E[X(p)^2] - E[X(p)X(p+r)])}. \quad (5.21)$$

The value of σ_{Reg}^2 is calculated for different values of r , varying from 0 to 100, for the sample image in clear water condition. The plot of the results are shown in Figure 5.4. It can be seen that $\sigma_{Reg}^2 = 0$ for $r = 0$, and then as r increases, image registration error, σ_{Reg}^2 , increases as well. In fact this shows that as r increases, the product of

$E[X(p)X(p+r)]$ decreases, because there is less correlation between the two pixels.

When the image contrast for a specific value of r is getting lower, the difference between pixel values decreases, which means the value of $E[(X(p) - X(p+r))^2]$ is getting lower. Assume $X(p)$ is the value of pixel in p position in a clear condition and $Y(p)$ is the pixel value for the same pixel position, p , in a general scattering condition, then

$$Y(p) = a_1X(p) + b_1, \quad (5.22)$$

where a_1 is the scaling factor due to extinction (loss of contrast) and b_1 is the offset value due to scattering. Therefore,

$$X(p) = \frac{1}{a_1}(Y(p) - b_1). \quad (5.23)$$

$X(p)$ of Equation (5.23) for pixel positions, p and $p+r$, can be substituted in Equation (5.20):

$$\begin{aligned} \sigma_{Reg}^2(X) &= E[(X(p) - X(p+r))^2], \\ &= E\left[\left(\frac{1}{a_1}(Y(p) - b_1) - \frac{1}{a_1}(Y(p+r) - b_1)\right)^2\right], \\ &= \frac{1}{a_1^2}E[(Y(p) - Y(p+r))^2], \\ &= \frac{1}{a_1^2}\sigma_{Reg}^2(Y). \end{aligned}$$

Therefore,

$$\sigma_{Reg}^2(Y) = c'^2\sigma_{Reg}^2(X), \quad (5.24)$$

where c' is the coefficient due to slope of the line, which represents the extinction and as a consequence the degradation of contrast. Here, the value of coefficient c' is chosen to be the proportion of image contrast in clear (c_1) and scattering condition (c_2), $c' = \frac{c_2}{c_1}$ for simplicity.

In this experiment the translation stage is designed to translate the camera with accurate steps, but still it introduces around 5 pixels registration error¹. The variance due to 5 pixels misregistration ($r = 5$) in clear water condition (high contrast) is found from the plot of σ_{Reg}^2 versus r in Figure 5.4, in which $\sigma_{Reg}^2(r = 5) = 120$. This value

¹Each full turn (360°) of the turning handle translates the camera about 2mm, and this corresponds to the length of 20 pixels. The personal error of turning the handle is assumed to be a quarter of the turning area $\frac{360^\circ}{4} = 90^\circ$, and this corresponds to $\frac{20}{4} = 5$ pixels.

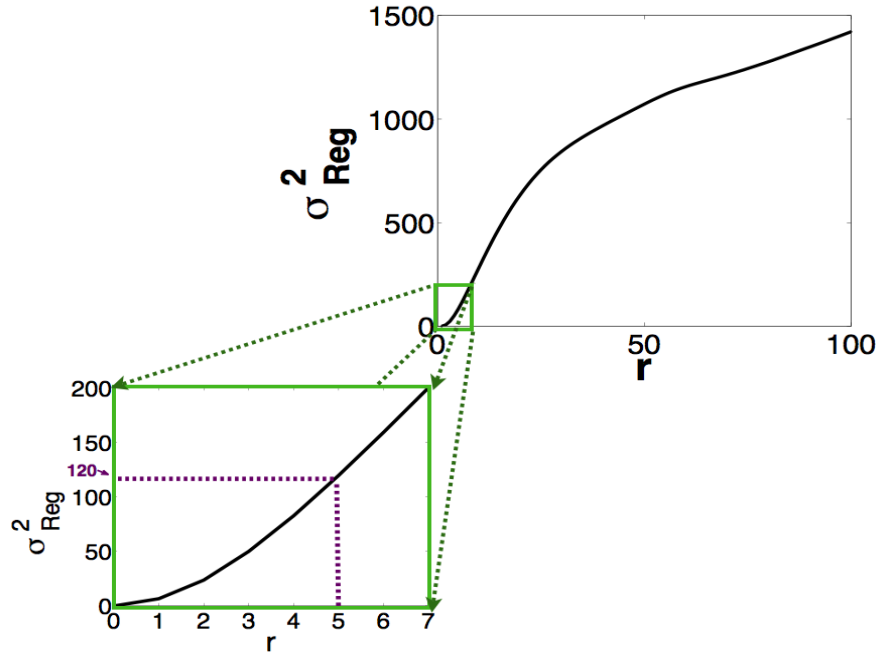


Figure 5.4: The plot of σ_{Reg}^2 versus r in clear water condition for sample image (first camera position) at $600nm$.

is expected to be lower for turbid water condition, $\sigma_{Reg}^2 = c'^2 \times 120$.

Calculations of Experimental Errors

In this experiment the amount of different sources of camera noise are as follow. The multispectral images are corrected for the dark current and fixed pattern noise by deducing the dark image from the main multispectral images. Also, the value for read out noise² and quantization noise³ are very low and are negligible. Therefore, two dominant sources of noise, shot noise and image registration noise, are used to calculate for the total experimental error, err .

$$err = \sqrt{\sigma_{N_S}^2 + c'^2 \sigma_{Reg}^2}. \quad (5.25)$$

The value of shot noise is $\sigma_{N_S} = \sqrt{18000}_{(electrons)}$, as shown in camera specification in Table A.2. The conversion between *electrons* and *counts(nbits)* units is

$$counts(nbits) = \frac{(electrons)}{camera\ gain},$$

² $\sigma_{N_R}^2 = 8^2_{electrons} = 0.01_{counts}$
³ $\sigma_{N_Q}^2 = 0.006$

where camera gain is

$$cameragain = \frac{Full\ well\ capacity}{2^n}, \quad n: \text{ is the number of bits.}$$

Here $n = 8$, and the value of full well capacity is $18000_{(electrons)}$ (Table A.2). As a result the value of camera gain is $\frac{18000}{(2^8)} = 70.31$. The converted value of shot noise in $counts(8bits)$ unit is $\sigma_{N_S} = \frac{\sqrt{18000}}{70.31} = 1.9$. The value of err in clear water condition ($c' = 1$) can be calculated by substituting the values of $\sigma_{N_S}^2$ and σ_{Reg}^2 in Equation(5.25):

$$\begin{aligned} err &= \sqrt{\sigma_{N_S}^2 + \sigma_{Reg}^2}, \\ err &= \sqrt{(1.9^2) + 120}, \\ err &= 11.12. \end{aligned}$$

5.3.5 Experimental Procedure

Four series of images are captured using the Hamamatsu camera at different levels of water turbidity, $T_0 - T_2$, at 20° water temperature. Each series contains 10 continuous monochrome images in a narrow spectral band of bandwidth $10nm$.

5.3.6 Results and Discussions

The sample of captured images in clear and turbid water conditions are shown in Figure 5.5.

A sample pixel position is selected in spatial position of $(244, 350)$. The intensity value of this pixel varies as the camera position changes. Figure 5.6 shows how the value of this pixel changes from the first image, which is taken at first camera position, to the last image.

The parameters $(b_\lambda(x, y)$ and $a_\lambda(x, y))$ in Equation (5.12) are estimated by the regression method for the sample pixel position of $(244, 350)$ at $600nm$ and for medium level of turbidity, T_2 . Figure 5.7 shows the scatter plot and the regression line of V_i versus V_f for the pixel position of $(244, 350)$ at $600nm$ for medium level of turbid water. It can be seen that some of the data points are dispersed around the regression line, which is due to the effect of the expected experimental error.

The amount of dispersion is calculated for the pixel position $(244, 350)$ and is $\sigma_{dispersion} = 4.45$. The expected experimental error for different levels of water turbidity at $600nm$ is calculated and presented in Table 5.1. It can be seen that the expected

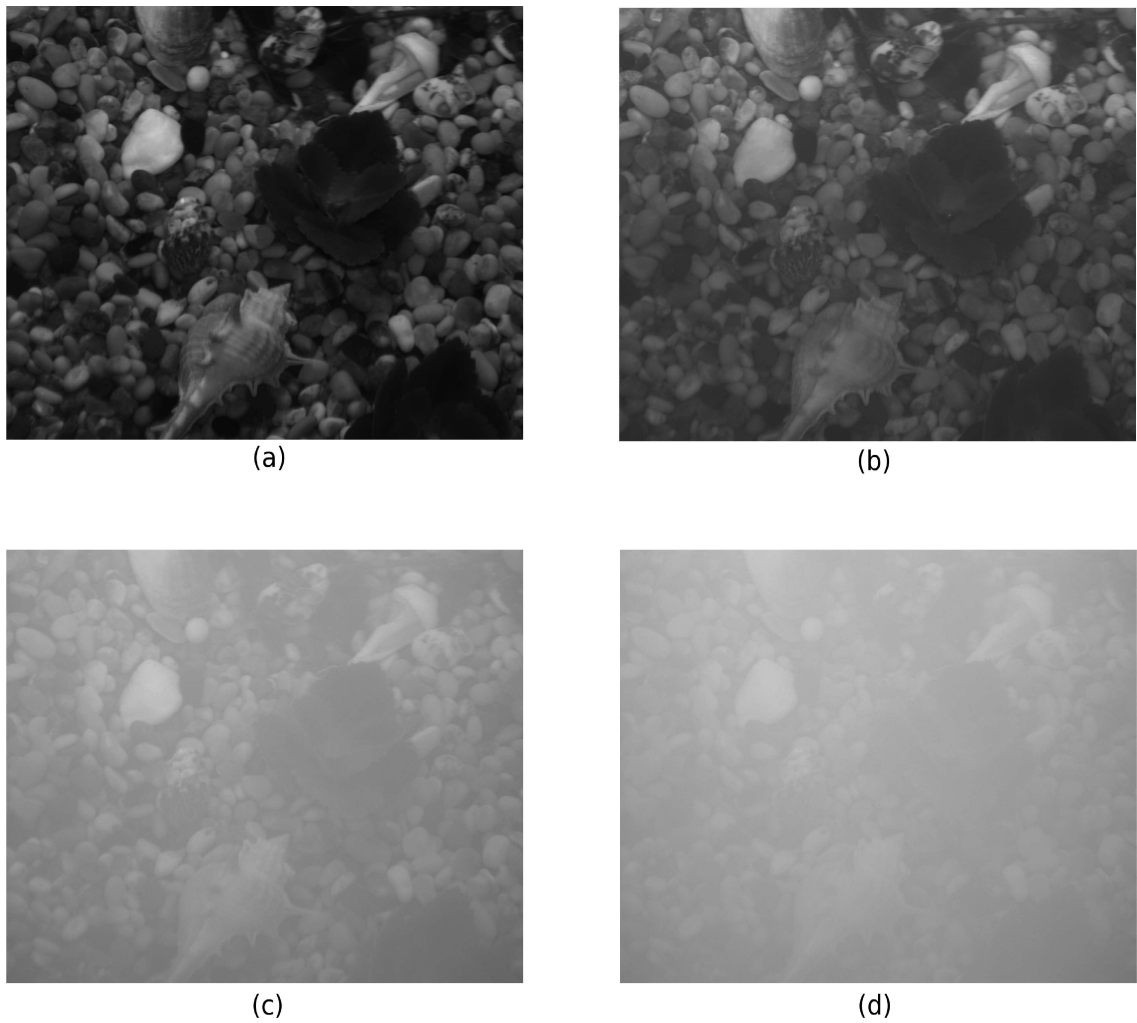


Figure 5.5: Sample of captured images (1024×1344) in 600nm wavelength at first camera position in a) Clear water condition b) Low level of turbid water, T_1 ($0.3gr/100litres$) c) Medium level of turbid water, T_2 ($0.7gr/100litres$) d) High level of turbid water, T_3 ($0.9gr/100litres$).

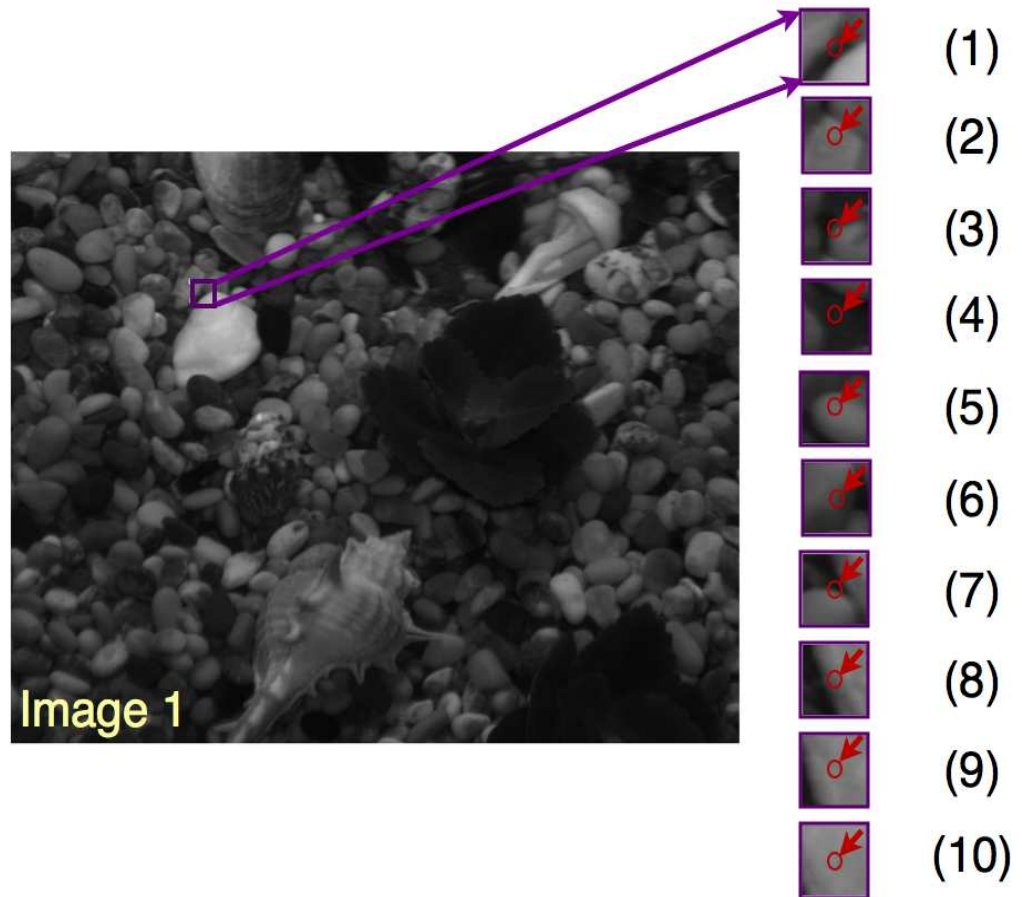


Figure 5.6: A block of 40×40 (226 : 266, 330 : 370) of neighboring pixels of pixel position (244, 350) is selected and shown for all 10 images. The content of the sample image pixel in position of (244, 350) in main image ((18, 20) in sample image block) is shown for different camera locations.

experimental error for T_2 water turbidity at 600 is $err_{T_2}(600nm) = 4.62$. By comparing the values of $err_{T_2}(600nm)$ and $\sigma_{dispersion}$, it can be concluded that the amount of dispersion for pixel position (244, 350) at 600nm and for T_2 water turbidity is within the expected experimental error.

	c'_{T_1}	err_{T_1}	c'_{T_2}	err_{T_2}	c'_{T_3}	err_{T_3}
550nm	0.7411	8.3374	0.3230	4.0160	0.2583	3.4085
600nm	0.8182	9.1621	0.3846	4.6217	0.2740	3.5521
650nm	0.7839	8.7946	0.3603	4.3805	0.3283	4.0675
700nm	0.7491	8.4233	0.3833	4.6084	0.3321	4.1045

Table 5.1: The calculated value for the expected experimental error and c' coefficient at different wavelengths and different level of water turbidity.

The values of $a_{600nm}(244, 350) = 0.1857$ and $b_{600nm}(244, 350) = 156.9$ can be found from the slope and Y-intercept of the regression line respectively. The values of $a_{600nm}(244, 350)$, $b_{600nm}(244, 350)$ and $err_{T_2}(600nm)$ are substituted in Equation (5.16). Therefore, $I_{600nm}(244, 350)$ equation can be written as

$$I_{600nm}(244, 350) = 156.9 + 0.1857 \times F_{600nm}(244, 350) \pm 4.62. \quad (5.26)$$

The prediction error of the estimated values is calculated using Equation (5.14), $\sigma_{PE}^2 = 4.98^2$. The intensity variation of 4.98 in range of [0 255] shows 1.9% deviation from the actual value, which means the method can predict the parameters value with 98.1%⁴ accuracy at 600nm.

The results so far showed that underwater image model is valid for one pixel position, (244, 350), at 600nm and for medium level of turbid water.

Next, the validity of the underwater image model is investigated for all image pixel positions at the same conditions by calculating the amount of dispersion. It is expected that the amount of dispersion for all pixel positions be about the expected experimental error, $err_{T_2}(600nm)$. Figure 5.8 shows the dispersion value for all image pixel positions for medium level of water turbidity at 600nm. The median value of dispersion for all pixel positions is calculated and is 3.85. It can be seen that this value is within the range of the predicted dispersion value, $err_{T_2}(600nm) = 4.62$. Therefore, it can be seen that underwater image model at 600nm and in medium level of turbid water is not

⁴ $100 \times \frac{4.98}{255} = 1.9\%$, $100\% - 1.9\% = 98.1\%$

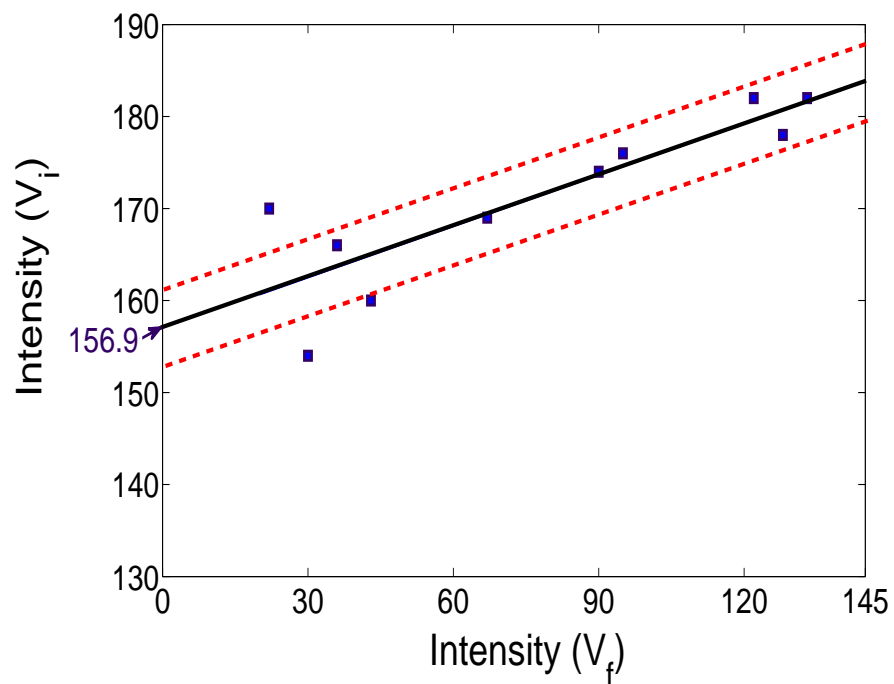


Figure 5.7: The plot of V_i versus V_f . V_i is the Fixed Path vector in turbid water condition and V_f is the Fixed Path vector in clear water condition. The estimated value of extinction and optical back-scatter are about 0.1857 and 156.9 respectively. The black solid line is for the regression line and the two red dashed lines in position of ± 4.62 from the regression line are defining the estimation intervals.

only valid for one pixel position, but also it is valid for all of the image pixel positions. However, for few pixel positions the dispersion value is higher than expected experimental error. This happens when the statistical solution fails to estimate accurately, as an example, when the value of data points at V_i are close to each other. To calculate for

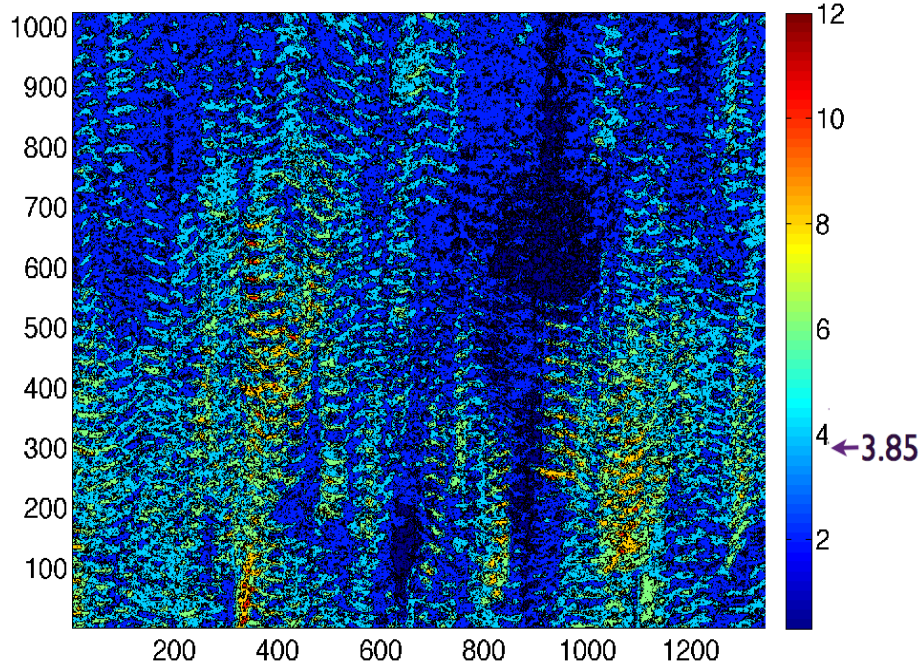


Figure 5.8: Dispersion value for all pixel positions at $600nm$, and for medium water turbidity, T_2 . The median dispersion for all pixel positions is 3.85 and the expected experimental error is 4.62.

the prediction error among all pixel positions, first the prediction error for each image pixel position is calculated, then the median value of the prediction error is calculated, $\sigma_{PE}^2(T_2)_{600nm} = 4.3^2$. This is 1.7% deviation in intensity range of $[0 \ 255]$ from actual value, which shows 98.3% accuracy.

Furthermore, the validity of underwater image model is investigated for different levels of water turbidity, low (T_1) and high (T_3), and also for different wavelengths. The camera spectral response and the camera filter transmittance vary with respect to wavelength. Also, the image contrast is changing for different water turbidity. All these contribute to variations in the camera noise and registration error, and so to variation in the total expected error. The value of total expected error, err , at different conditions

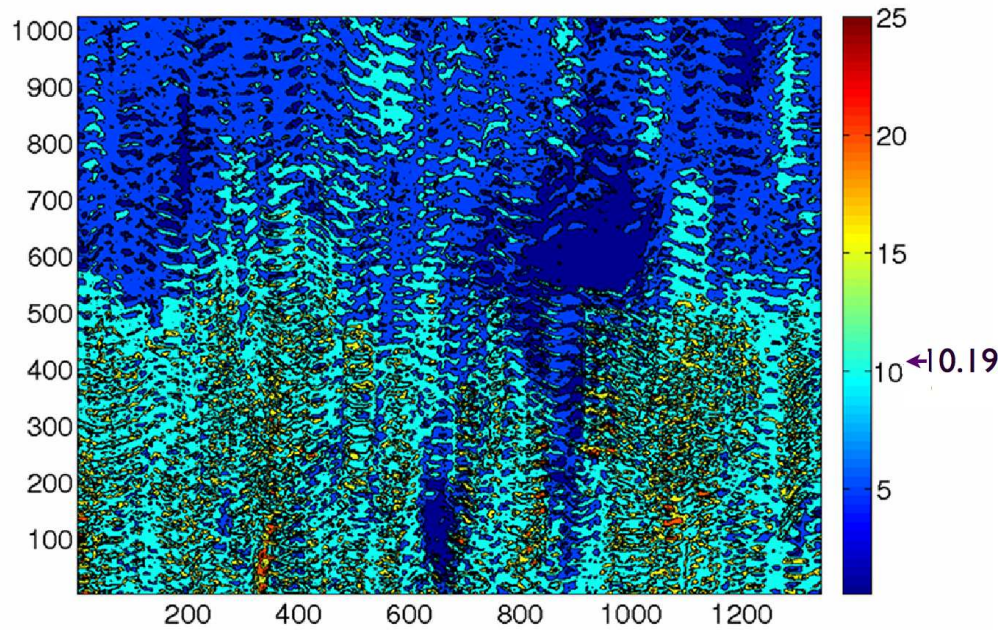
are calculated and presented at Table 5.1. Figure 5.9 shows the plots of dispersion for all pixel positions for two different levels of water turbidity, T_1 and T_3 , at $600nm$. The expected experimental error for two different levels of water turbidity at $600nm$ can be found at Table 5.1, $err_{T_1}(600nm) = 9.16$ and $err_{T_3}(600nm) = 3.55$. The median value of dispersion for all image pixel positions for $L1$ and $L3$ level of water turbidity are 10.19 and 2.28 respectively. It can be seen that these values are within the range of the expected experimental error for different levels of water turbidity.

The median value of prediction error of the estimated values for two different levels of turbid water, T_1 and T_3 , and at $600nm$ are calculated, $\sigma_{PE}^2(T1)_{600nm} = 11.45^2$ and $\sigma_{PE}^2(T3)_{600nm} = 2.54^2$. These values represent 4.5% and 0.9% prediction error for T_1 and T_3 at $600nm$ respectively.

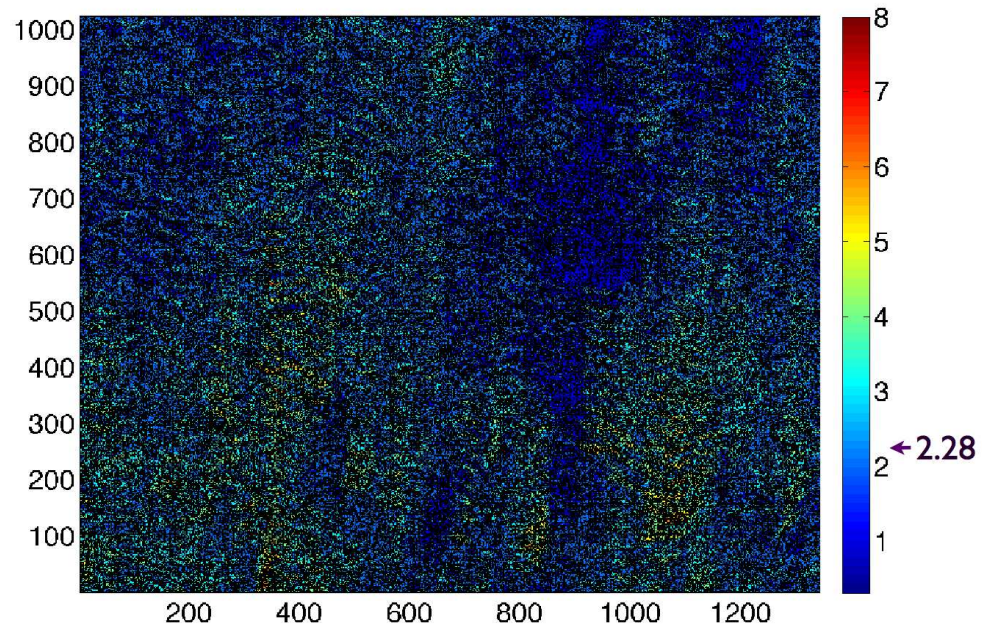
Figures 5.10 and 5.11 show the plots of dispersion for all pixel positions for medium level of water turbidity, T_2 , and at $550nm$ and $650nm$, $700nm$ respectively. The expected experimental error for three different wavelengths for $L2$ level of water turbidity can be found at Table 5.1, $err_{T_2}(550nm) = 4.01$, $err_{T_2}(650nm) = 4.38$ and $err_{T_2}(700nm) = 4.6$. The median value of dispersion for all image pixel positions for $T2$ level of water turbidity and at $550nm$ and $650nm$, $700nm$ are 3.39, 4.21 and 4.62 respectively. It can be seen that these values are within the range of expected experimental error.

The median value of prediction error of the estimated values for T_2 level of water turbidity at $550nm$, $650nm$, $700nm$ are calculated, $\sigma_{PE}^2(T2)_{550nm} = 3.79^2$, $\sigma_{PE}^2(T2)_{650nm} = 4.7^2$ and $\sigma_{PE}^2(T2)_{700nm} = 5.17^2$. These values represent 1.48%, 1.84% and 2.02% prediction error for T_2 at $550nm$, $650nm$, $700nm$ respectively.

It can be seen from the results that the dispersion is within the range of expected error, and remains consistent over variation of water turbidity and wavelength. The prediction error is calculated in each condition and is less than 5%. Therefore, the validation of the proposed underwater image model (Equation (5.12)) is confirmed with at least 95% accuracy and Equation (5.13) can be used in the proposed underwater image enhancement method.



(a)



(b)

Figure 5.9: Dispersion value for all pixel positions at $600nm$ for a) Low level of turbid water, T_1 . The median dispersion for all pixel positions is 10.19 and the expected experimental error is 9.16. b) High level of turbid water, T_3 . The median dispersion for all pixel positions is 2.28 and the expected experimental error is 3.55.

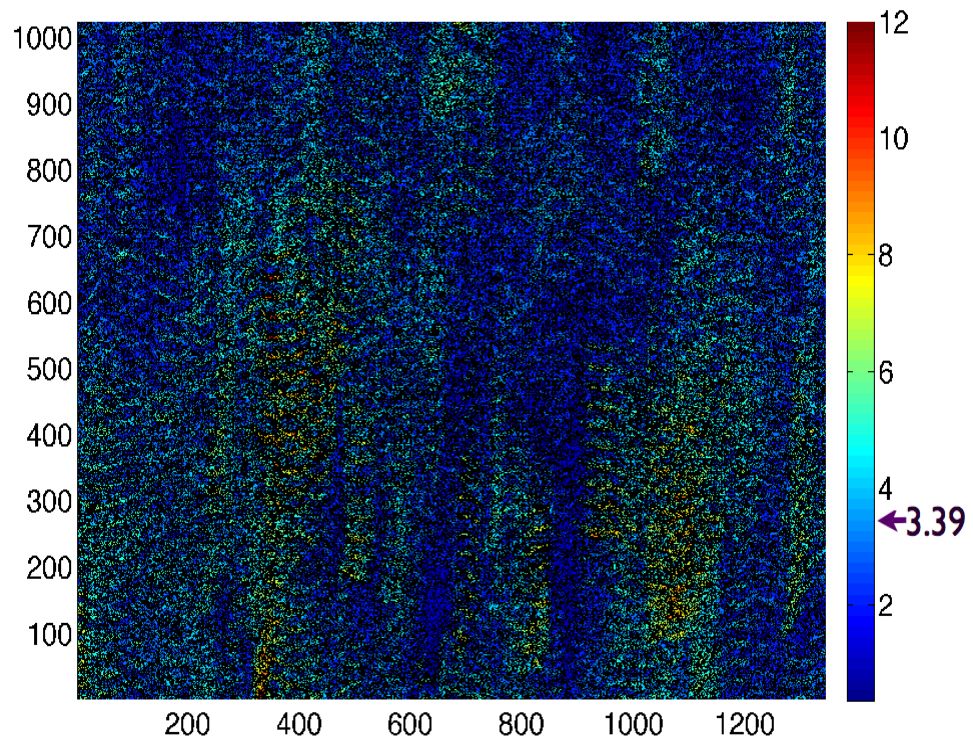
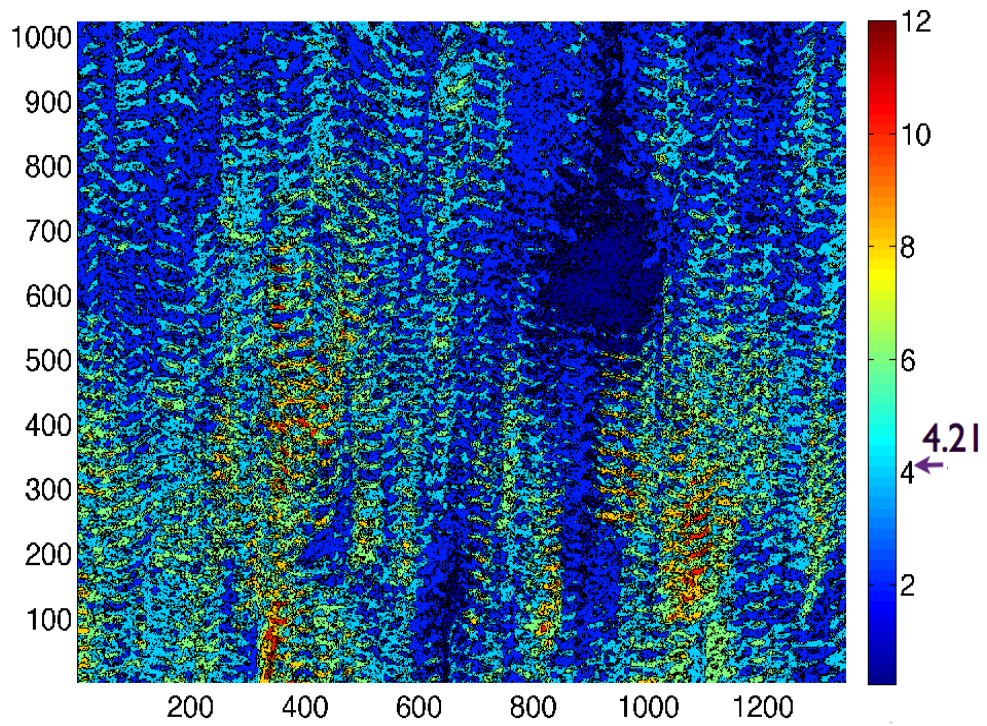
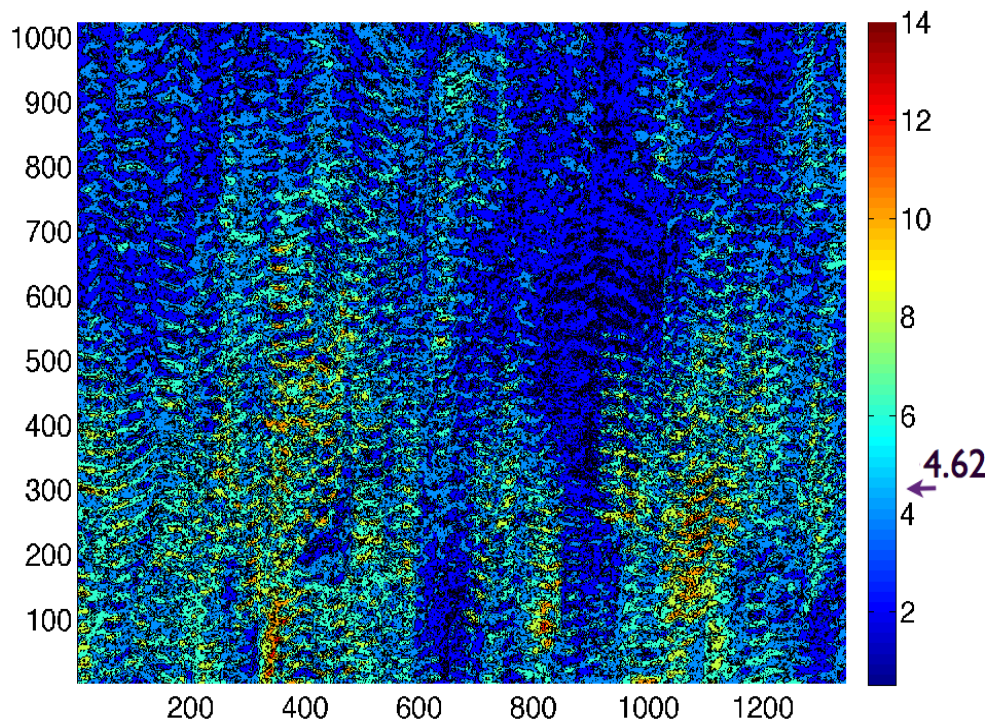


Figure 5.10: Dispersion value for all pixel positions at $550nm$ for medium level of turbid water, T_2 . The median dispersion for all pixel positions is 3.39 and the expected experimental error is 4.01.



(a)



(b)

Figure 5.11: Dispersion value for all pixel positions for medium level of turbid water, T_2 , at a) 650nm. The median dispersion for all pixel positions is 4.21 and the expected experimental error is 4.38. b) 700nm. The median dispersion for all pixel positions is 4.62 and the expected experimental error is 4.60.

Chapter 6

Mitigation of Contrast Loss in Underwater Images

In this chapter a new physics-based approach is proposed to improve the quality of an underwater image by mitigating the contrast loss. The contrast loss in underwater images is due to the effect of optical back-scatter.

The proposed method is based on Equation (5.13), by which the contrast loss can be mitigated by subtracting optical back-scatter, $b_\lambda(x, y)$, from the degraded underwater image and then multiplying the image by a scaling parameter, $\frac{1}{a_\lambda(x, y)}$. The key issue is how to estimate $b_\lambda(x, y)$. The aim of this chapter is to propose different methods to address this issue for monochrome underwater images. The proposed methods use statistical techniques and digital image processing tools and do not require a prior physical information about the scene. The operation of subtraction is in fact a kind of filtering. Hence, the methods for estimating $b_\lambda(x, y)$ in this work are called back-scatter filters (BS filters). For the purpose of simplifying the notation, the abbreviation form of $b_\lambda(x, y)$ and $a_\lambda(x, y)$, which are respectively b_λ , a_λ , are used in this section.

This chapter is structured as follows. Section 6.1 explains the estimation of b_λ . This includes the model of optical back-scatter variation throughout a degraded image. Also, the proposed BS filters are explained. Section 6.1.2 explains the method for estimating the value of a_λ .

6.1 Estimation of b_λ and a_λ

Several studies have been done to estimate b_λ in a turbid medium. Oakley & Satherley (1998) propose an estimation method to recover degraded images in adverse atmospheric conditions. This involves analysis of the pixel intensity as a function of range. Schechner & Karpel (2005) propose a method for estimating b_λ in underwater images. This involves analysis of images taken with different orientations of polarising filter. Both of these methods require additional physical information about the scene.

Oakley & Bu (2007) propose a new statistical method, based on the minimisation of a cost function, to estimate for the level of b_λ in the degraded image, without using any physical information of the scene. However, in this work b_λ is assumed to be spatially constant for images in air. This assumption is not valid for underwater images, as the optical back-scatter is spatially variant (Schechner & Karpel 2004).

In this work, three BS filters are proposed. Each filter provides an estimate of b_λ by using statistical solutions and digital image processing tools, without using any physical information about the scene. The proposed BS filters are denoted here by BS-MinPix, BS-Hist and BS-CostFunc filter. The BS-MinPix filter estimates b_λ in one pixel position (x, y) only and does not require the shape of optical back-scatter variation in a degraded image. The BS-Hist and BS-CostFunc filters estimate the function of b_λ for the whole image. First, the model of the optical back-scatter and extinction spatial distribution of image is explained. Then, the various BS filters are explained.

6.1.1 Optical Back-scatter Model

The spatial distribution of optical back-scatter is unknown. The physical model of the optical back-scatter, which is presented in Equation (2.7), suggests that optical back-scatter follows the scene illumination spatial distribution and is independent of the scene content. The spatial distribution of scene illumination depends on the light source, which is used to provide the required illumination in underwater imaging. The part of the scene that is directly in front of the beam, is illuminated more and the surroundings are less illuminated. This produces a hump at the part with high illumination.

Figure 6.1(a) shows an image from an underwater scene that is illuminated by a searchlight in clear water. The middle part of the image, which is in the direction of the searchlight, is well illuminated, but the sides are darker. The line-plot of one of the middle lines (line 400) of the image is plotted and presented in Figure 6.1(b) by

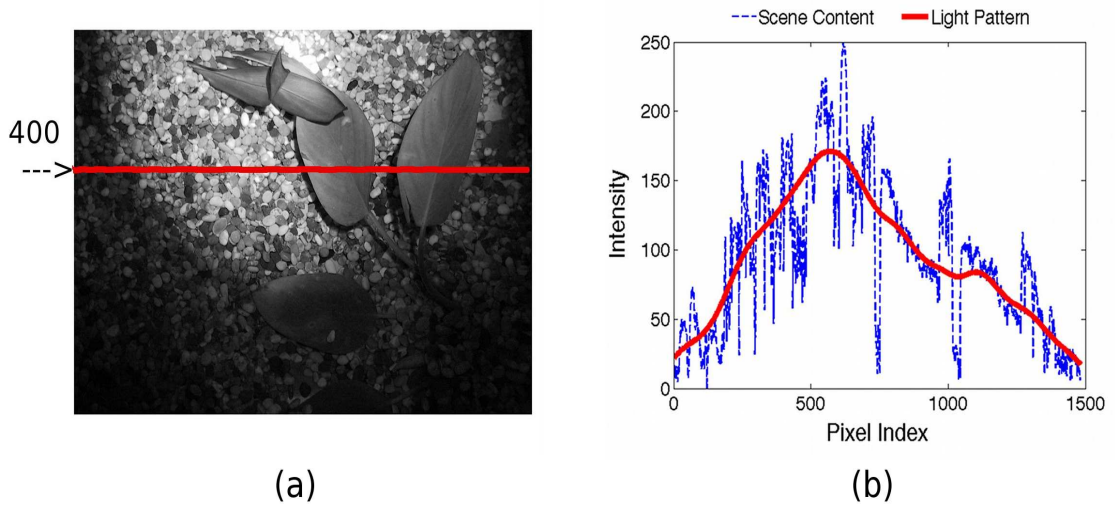


Figure 6.1: a) A sample of underwater image in clear water condition, where the scene is illuminated by a search light. b) The line-plot of row=400 of the original image (dashed line) and the line-plot of row=400 of the filtered image by a low pass filter.

a dashed line. This profile can be regarded as the sum of two spatial distributions. A high frequency, which is due to variation in the scene content, is superimposed on a low frequency, which is due to the illumination profile. The low frequency can be extracted from the image by applying a low pass (averaging) filter (LPF) to the image, either in time or space. The solid line in Figure 6.1(b) presents the line plot of the filtered image by a LPF. It can be seen that the plot has a shape that is similar to a truncated raised cosine function.

The general model of a degraded underwater image, which is given in Equation (5.11), is reproduced here. A lowpass filter with kernel function g is applied. The resulting image can be written as

$$I_\lambda(x, y) * g = (\zeta C_0 [\beta_\lambda(x, y)R + (1 - \beta_\lambda(x, y)R)R_\lambda(x, y)]) * g, \quad (6.1)$$

$$\bar{I}_\lambda = (\zeta C_0 \beta_\lambda R) * g + [\zeta C_0 (1 - \beta_\lambda R)R_\lambda] * g. \quad (6.2)$$

For the purpose of simplifying the notation, the abbreviated form of $I_\lambda(x, y)$, $\beta_\lambda(x, y)$ and $R_\lambda(x, y)$, which are respectively I_λ , β_λ and R_λ , are used in this part. The symbol $*$ denotes the two dimensional convolution operation. The low pass filter gives a smoothed version of the image. Hence, in this work \bar{I}_λ is used instead of the term

$I_\lambda * g$. It is explained in Section 5.1 that ζ is a constant value. If it is assumed that the range R is constant for all pixel positions, then $\beta_\lambda R$ is a constant value for same water turbidity, and as a result Equation (6.2) can be written as

$$\bar{I}_\lambda = \zeta\beta_\lambda R(C_0 * g) + \zeta(1 - \beta_\lambda R)[(C_0 R_\lambda) * g]. \quad (6.3)$$

$C_0 * g \simeq C_0$. The reflectance factor, R_λ , for the scene content is assumed to be a stationary random field with mean \bar{R}_λ . $(C_0 R_\lambda) * g \simeq C_0 \bar{R}_\lambda$ because C_0 is the illumination radiance and has low spatial frequency (LSP). R_λ has high spatial frequency and after convolving with g , is \bar{R}_λ , which is a nearly constant value. As a result Equation (6.3) can be written as

$$\bar{I}_\lambda = \zeta[\beta_\lambda R + (1 - \beta_\lambda R)\bar{R}_\lambda]C_0. \quad (6.4)$$

The term $\zeta[\beta_\lambda R + (1 - \beta_\lambda R)\bar{R}_\lambda]$ is a constant value, and for simplicity it can be written as γ_1 .

$$\gamma_1 = \zeta[\beta_\lambda R + (1 - \beta_\lambda R)\bar{R}_\lambda]. \quad (6.5)$$

Therefore, Equation (6.4) can be simplified to

$$\bar{I}_\lambda = \gamma_1 C_0. \quad (6.6)$$

The general model of back-scatter light, which is given in Equation (5.7), is reproduced here considering the camera gain, ζ and after applying a lowpass filter with kernel function g as

$$b_\lambda(x, y) * g = (\zeta C_0 \beta_\lambda(x, y) R) * g. \quad (6.7)$$

For the purpose of simplifying the notation, the abbreviation form of $b_\lambda(x, y)$, which is b_λ , is used.

Considering $\zeta\beta_\lambda R$ as a constant value, which is simplified to γ_2 , then

$$b_\lambda * g = \zeta\beta_\lambda R(C_0 * g). \quad (6.8)$$

$b_\lambda * g$ is approximately the same as b_λ , since b_λ comprises only low spatial frequency components.

$$b_\lambda = \gamma_2 C_0. \quad (6.9)$$

Comparing equations (6.6) and (6.9) suggests that

$$C_0 = \frac{b_\lambda}{\gamma_2} = \frac{\bar{I}_\lambda}{\gamma_1}. \quad (6.10)$$

Therefore, the spatial distribution of optical back-scatter can be written as

$$\boxed{b_\lambda = \frac{\gamma_2}{\gamma_1} \bar{I}_\lambda = \gamma \bar{I}_\lambda.} \quad (6.11)$$

An illustration is given in Figure 6.2 to show the scale difference between the spatial distribution of optical back-scatter and illumination. Figure 6.2(a) presents a sample underwater image in size of 1024×1344 . The sample image is chosen from T_3 test images in 600nm. Figure 6.2(b) presents the line-plots of row=500 for original image with a dash-dotted line, the smoothed image with a dashed line, and finally the estimated level of optical back-scatter, which is found by the regression method with a solid line. It can be seen that the optical back-scatter has the same spatial distribution as image illumination, but with a different scale factor. Figure 6.2(b) presents the comparison between $b_\lambda(x, y, \gamma)$ and $\bar{I}_\lambda(x, y)$ for only one image row. The comparison for all of the image rows is done by plotting with a contour plot. Figures 6.2(c) and (d) present the contour plots of $b_\lambda(x, y, \gamma)$ and $\bar{I}_\lambda(x, y)$ for all image rows respectively.

6.1.2 Extinction Model

The definition of a_λ , which is given in Equation (5.2), is reproduced here considering the camera gain, ζ and after applying a lowpass filter with kernel function g as

$$a_\lambda * g = (\zeta C_0 (1 - \beta_\lambda R) R_\lambda) * g. \quad (6.12)$$

$a_\lambda * g$ is approximately the same as a_λ , since a_λ comprises low spatial frequency components. The approximations of $R_\lambda * g$ and $C_0 * g$ are as explained earlier.

$$a_\lambda = (\zeta - \zeta \beta_\lambda R) \bar{R}_\lambda C_0. \quad (6.13)$$

On the other hand by rearranging Equation (6.5), \bar{R}_λ can be written as

$$\bar{R}_\lambda = \frac{\gamma_1 - \zeta \beta_\lambda R}{\zeta (1 - \beta_\lambda R)}. \quad (6.14)$$

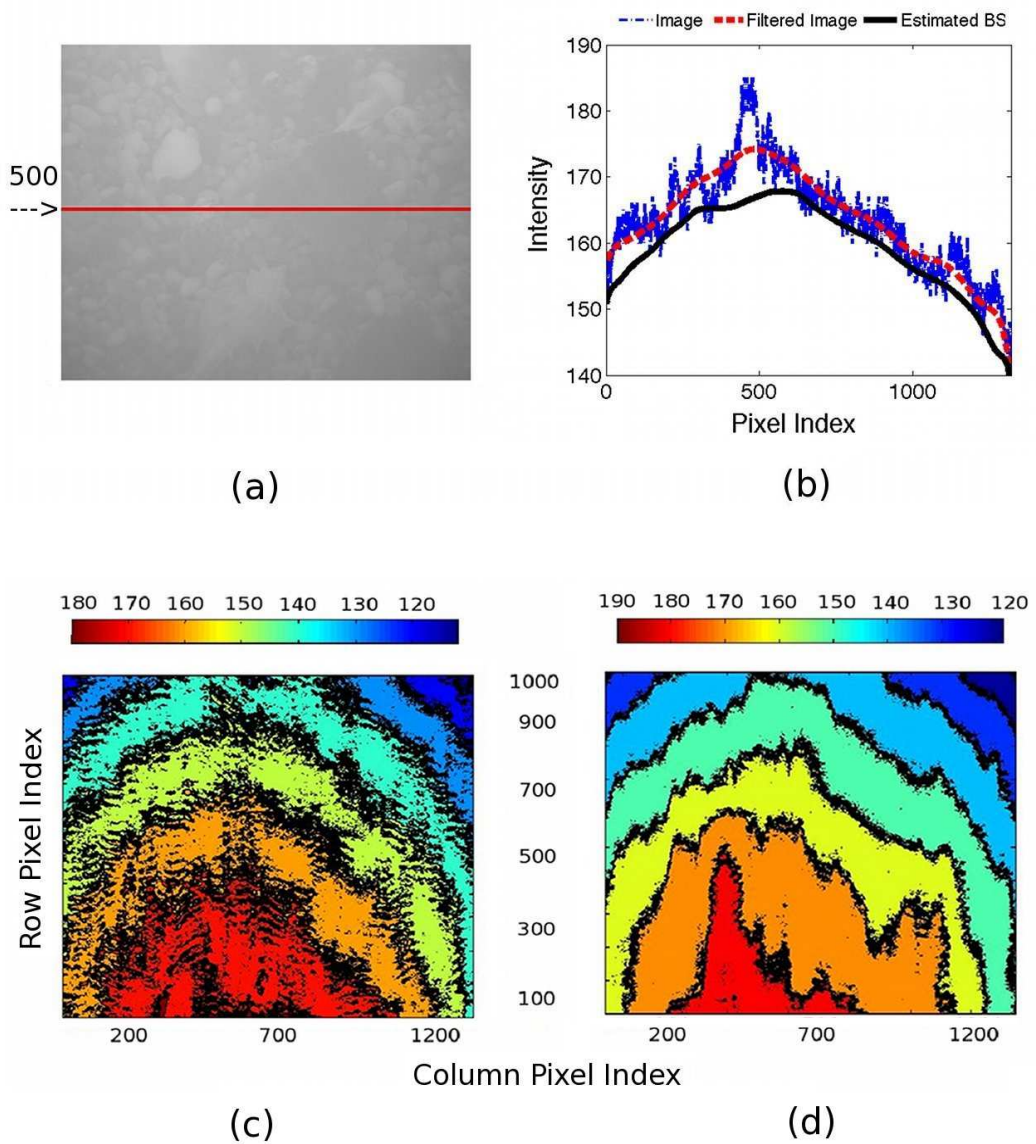


Figure 6.2: a) The sample image in size of 1024×1344 from from T_3 test images in 600nm. b) The line-plots of row=500 for I_λ with a dash-dotted line, \bar{I}_λ with a dashed line, and b_λ with a solid line. c) The contour plot of the estimated optical back-scatter. d) The contour plot of the smoothed image.

By substituting Equation (6.14) in Equation (6.13), a_λ can be written as

$$a_\lambda = C_0(\zeta - \zeta\beta_\lambda R) \frac{\gamma_1 - \zeta\beta_\lambda R}{\zeta - \zeta\beta_\lambda R}. \quad (6.15)$$

By substituting γ_2 and $\frac{\bar{I}_\lambda}{\gamma_1}$ instead of $\zeta\beta_\lambda R$ and C_0 respectively, then

$$a_\lambda = \frac{(\zeta - \gamma_2)(\gamma_1 - \gamma_2)(\bar{I}_\lambda)}{(\zeta - \gamma_2)(\gamma_1)}, \quad (6.16)$$

$$= \frac{\gamma_1 - \gamma_2}{\gamma_1} \bar{I}_\lambda, \quad (6.17)$$

$$= 1 - \frac{\gamma_2}{\gamma_1} \bar{I}_\lambda. \quad (6.18)$$

Considering Equation (6.11), then

$$a_\lambda = 1 - \gamma \bar{I}_\lambda = 1 - b_\lambda. \quad (6.19)$$

Equations (6.11) and (6.19) show that to estimate b_λ and a_λ , the smoothed version of the image and a constant parameter, γ are required. The smoothed version of the image is obtained using a recursive Gaussian filter with standard deviation of a relatively large value of σ_B (Mortazavi & Oakley 2007, Oakley & Bu 2007). γ is the only unknown parameter. Therefore, by finding γ the optical back-scatter and extinction distribution function are known. The aim of the BS-Hist and BS-CostFunc filters is to find γ .

6.1.3 BS-MinPix Filter

Assume that there are several images with different image contents. Suppose at least one pixel in spatial position of (x, y) from these images falls on a dark object. Therefore, the pixel value is $R_\lambda(x, y) \approx 0$. According to Equation (5.12), when $R_\lambda(x, y) \approx 0$ the value of this dark image pixel in a turbid medium should represent the level of optical back-scatter, $b_\lambda(x, y)$. An example of this can be found in practice, when underwater images are captured from different scenes by a camera with a fixed angle and height on a ROV system in the same turbid water environment.

On this basis a rank filter is used to take the minimum pixel value from a set of degraded sample pixels of the same level of optical back-scatter. These sample of pixels can be from one pixel position at different images with same level of optical back-scatter. Therefore, in this method n_{mp} images, where $n_{mp} > 1$, with same level of optical scattering and different scene content are required.

6.1.4 BS-Hist Filter

This method is similar to histogram modification. It is explained in Section 5.3.4 that when an image is captured by a CCD camera, camera noise is added during the process of acquisition and conversion. Therefore, the image pixels represent both the reflected light from the scene and the added camera noise. The pixel values of image content in a turbid medium are mostly high due to the extra value added to image content because of the effect of optical back-scatter. Therefore, the histogram of a degraded image is mostly concentrated at the right part in visible range. But, in real imaging condition the image histogram has an additional small area at low pixel values, which is due to the effect of camera noise. In BS-Hist filter the idea is to modify the output image histogram in such a way to keep that part of the image histogram due to camera noise out of visible range.

The algorithm used in the BS-Hist filter is to calculate the value of γ (from Equation 6.11) by keeping $n_{HB}\%$ of the histogram of $\hat{I}_\lambda(x, y)$ from Equation (5.13) out of visible range [0 255].

6.1.5 BS-CostFunc Filter

Oakley & Bu (2007) introduced a new statistical method, Oakley-Bu cost function, to detect a constant level of optical back-scatter in a degraded image, which is taken in adverse atmosphere conditions such as fog or haze. In this work, the algorithm is extended to be used for a variable distribution of optical back-scatter. The extended algorithm is found by substituting Equation (6.11), instead of b in Equation (2.14) as shown below

$$S_\lambda(\gamma) = \frac{1}{P} \sum_{p=1}^P \left(\frac{I_\lambda(p) - \bar{I}_\lambda^{cf}(p)}{\bar{I}_\lambda^{cf}(p) - \gamma \bar{I}_\lambda(p)} \right)^2 \cdot \exp \left(\frac{1}{P} \sum_{p=1}^P \ln(\bar{I}_\lambda^{cf}(p) - \gamma \bar{I}_\lambda(p))^2 \right), \quad (6.20)$$

where p represents each image pixel in spatial position of (x, y) . It is shown mathematically in Appendix B that the extended cost function has a minimum value at γ . Therefore, the value of γ can be estimated by Equation (6.20).

Note that there are two types of the smoothed images in Equation (6.20), in which both of them are smoothed by recursive Gaussian filter with two different filter parameters. Oakley & Bu (2007) have shown that the performance of cost function is more accurate, when a small filter parameter, σ_{cf} , is used for \bar{I}_λ^{cf} . \bar{I}_λ is used to extract the illumination variation from the image, and as a result the image should be highly

smoothed in order to have no image content. Therefore, a large filter parameter σ_B is required for \bar{I}_λ .

Chapter 7

Simulations

In this chapter, the performances of the algorithm of BS filters are explored using Monte-Carlo simulation with synthetic underwater images. The efficiency of the algorithms in terms of accuracy and reliability is determined.

This chapter is structured as follows. In Section 7.1, the method for synthesis synthetic underwater images in monochrome and colour is explained. Section 7.2 evaluates the performances of BS filters under different statistical assumptions. The results of improving degraded monochrome synthetic images using BS-CostFunc, as well as examples of the improved monochrome images are presented. Section 7.3 is concerned with the amount of colour difference introduced to the improved images by processing synthetic colour images, both in narrow and wide spectral bands, with the proposed method.

7.1 Synthetic Underwater Image

Synthetic underwater images are simulated based on the model of an underwater image given by Equation (5.12). A synthetic degraded underwater image in a specific central wavelength of λ , $I_{syn}(\lambda)$, can be presented by

$$I_{syn}(\lambda) = a_{syn}(\lambda)Im_{syn}(\lambda) + b_{syn}(\lambda), \quad (7.1)$$

where $Im_{syn}(\lambda)$ is the synthetic underwater image in clear water condition, $a_{syn}(\lambda)$ is the scaling factor due to the optical extinction and $b_{syn}(\lambda)$ is the synthetic optical back-scatter function in a specific wavelength.

From the study of several real continuous underwater images (Mortazavi 2006), it

is found that the spatial distribution of light intensity can be simulated by a positive truncated cosine function. In this work, it is assumed that the spatial variation is in one direction, only across image rows. Image content is formed from different surfaces, where the appearance of each surface is a function of illumination and reflectance (I. Motoyoshi & Adelson 2007). A synthetic clear underwater image is represented by

$$Im_{syn} = \hat{I}_{syn} S_{syn}(\lambda) \cos(\theta), \quad \frac{-\pi}{2} < \theta < \frac{\pi}{2} \quad (7.2)$$

where \hat{I}_{syn} represents the reflected light from the scene content, $S_{syn}(\lambda)$ is the illumination power spectrum and $\cos(\theta)$ is the spatial distribution of the light intensity across an image row.

7.1.1 Formation of Image Content (\hat{I}_{syn})

In this work, it is assumed that image content is constituted from more than one surface. A check board pattern is used to represent different surfaces with different textures in a synthetic image. This pattern is simple and is used in previous work (Oakley & Bu 2007) to generate synthetic images. Therefore, image content, $\hat{I}_{syn}(\lambda)$, is composed from $M \times N$ blocks, where each block is in size $m \times n$ and can have a different mean value with respect to the other blocks. To make each image block corresponds to a natural image texture, it is required to find a statistical distribution that matches the distribution of a natural texture. The Beta distribution is chosen for this purpose, since the distribution of reflectance within a range of real textures are better described by the Beta distributions as explained in Section 2.3.2.

To generate a natural texture with a Beta distribution, it is necessary to define the value of α_{Beta} and β_{Beta} parameters carefully in order that the pdf matches that of the natural texture.

Setting the Beta Distribution Parameters

Attewell & Baddeley (2007) study natural texture distributions and estimate parameters values of the Beta distribution, α_{Beta} and β_{Beta} , for four different types of environment, Woodland, Beach, Urban and Interior. The result of their work is presented in Table 7.1.1. It can be seen that the mean intensity has a relatively low value and the values of α_{Beta} and β_{Beta} are greater than one for all of the environments. The data from Attewell & Baddeley (2007) is limited to just four types of texture. Thus, the textures

Environment	α_{Beta}	β_{Beta}	Mean (μ_B)	STD(σ_B)
Woodland	1.91	22.6	0.08	0.06
Beach	2.04	7.57	0.21	0.13
Urban	1.35	10.72	0.11	0.11
Interior	1.29	2.3	0.36	0.22

Table 7.1: Estimated values of Beta distribution parameters based on Attewell & Baddeley (2007) study for four different types of environments, Woodland, Beach, Urban and Interior.

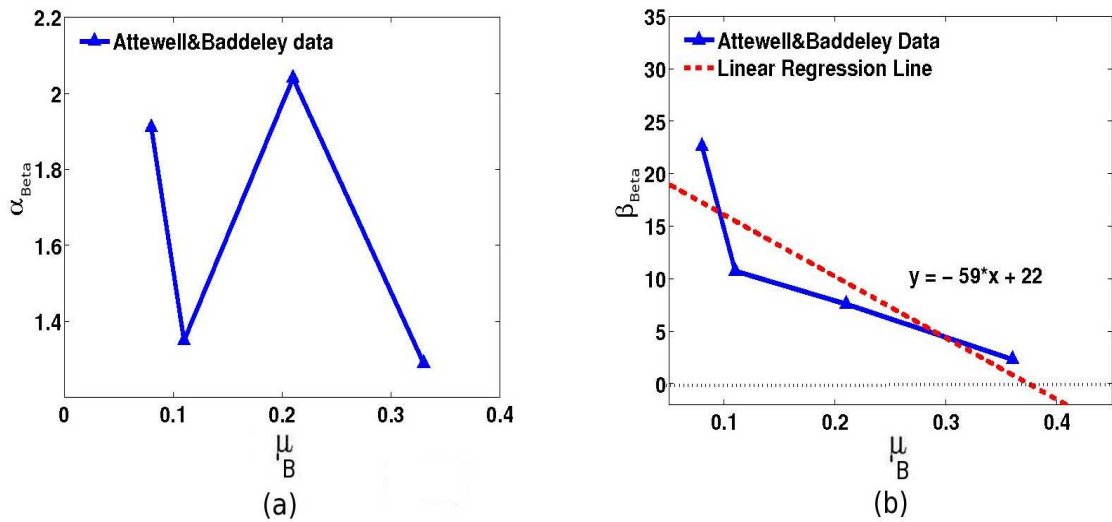


Figure 7.1: a) The plot of μ_B and α_{Beta} , b) The plot of μ_B and β_{Beta} , for natural textures data from Attewell & Baddeley (2007) data.

are limited to have four values of mean intensity, whereas a range of different mean intensities is required to find a comprehensive texture model.

The extended model of Attewell & Baddeley (2007) data, which is presented below, can be used to synthesise various natural textures. To construct the extended model of Attewell & Baddeley (2007) data, the relationships of mean, μ_B , with Beta parameters, α_{Beta} & β_{Beta} , are investigated. Figure 7.1 shows the plots for α_{Beta} and β_{Beta} versus mean (μ_B) for Attewell & Baddeley (2007) data. The β_{Beta}/μ_B plot shows a monotonic relationship, whereas the α_{Beta}/μ_B does not. The linear regression line of the β_{Beta}/μ_B plot is found and plotted as a dashed line in Figure 7.1(b). This line has the

form

$$\beta_{Beta} = -59\mu_B + 22, \quad (7.3)$$

which by rearranging can be written as

$$\mu_B = \frac{22 - \beta_{Beta}}{59}. \quad (7.4)$$

The range of valid β_{Beta} for the natural texture is $\beta_{Beta} > 1$. Because, for $\beta_{Beta} > 1$ the distribution has a hump, which is common in natural textures. As a result, the range of μ_B is $0 < \mu_B < 0.36$ ($0.36 = \frac{22-1}{59}$). Equation (7.5) is used as an extended model of Attewell & Baddeley (2007) data.

$$\beta_{Beta} = -59\mu_B + 22, \quad 0 < \mu_B < 0.36. \quad (7.5)$$

The mean intensity of each image block, μ_B , is calculated from a uniform distribution within a range $[0.01, 0.36]$ unless stated. The upper range is limited to 0.36, because of the limitation of $\beta_{Beta} > 1$. The lower range is chosen arbitrary ($\mu_B > 0$). The value of β_{Beta} can be simply estimated from Equation (7.5) for different mean values. The value of α_{Beta} can be calculated by using the relationship between the β_{Beta} and α_{Beta} parameters in the Beta distribution (Ghahramani 2000), which is given by Equation (7.6).

$$\alpha_{Beta} = \frac{\mu_B \beta_{Beta}}{1 - \mu_B}. \quad (7.6)$$

7.1.2 Synthetic Optical Back-scatter

The spatial distribution of an optical back-scatter function follows the spatial distribution of light variation across the image as explained in Section 6.1.1. The optical back-scatter function, $b_{syn}(\lambda)$, can be simulated by

$$b_{syn}(\lambda) = \gamma_s \cos(\theta) S b_{syn}(\lambda), \quad \frac{-\pi}{2} < \theta < \frac{\pi}{2} \quad (7.7)$$

where γ_s is the parameter used to set the level of synthetic optical back-scatter intensity, $\cos(\theta)$ is as defined before and $S b_{syn}(\lambda)$ is the optical back-scatter spectrum.

Figure 7.2 presents an example of the spatial distribution of synthetic light and synthetic optical back-scatter function of one row for a specific wavelength. The values are set to $S_{syn}(\lambda) = 1$, $S b_{syn}(\lambda) = 1$, $\gamma_s = 0.8$ and the intensity variation function is $\cos(\frac{\pi x}{1.5w} - \frac{\pi}{3})$, where w is for the size of an image row.

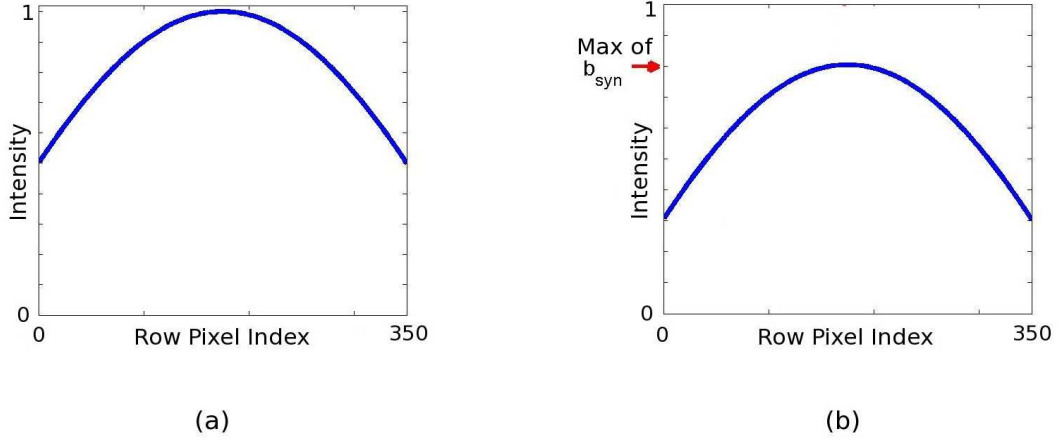


Figure 7.2: a) A sample pattern of intensity variation across an image row generated by $\cos(\frac{\pi x}{1.5w} - \frac{\pi}{3})$, where w is for the width of an image row. In this example $w = 350$. b) A sample of synthetic optical back-scatter function, $b_{syn} = 0.8 \cos(\frac{\pi x}{1.5w} - \frac{\pi}{3})$.

7.1.3 Synthetic Underwater Image

By substituting Equations (7.2) and (7.7) in Equation (7.1), $I_{syn}(\lambda)$ can be written as

$$I_{syn}(\lambda) = [\hat{I}_{syn}(\lambda) S_{syn}(\lambda) + \gamma_s S b_{syn}(\lambda)] \cos(\theta), \quad -\frac{\pi}{2} < \theta < \frac{\pi}{2} \quad (7.8)$$

Figure 7.3 illustrates the formation of a sample synthetic underwater monochrome image. As explained in Section 5.3.4, in a real imaging situation there are always some noise contributions added to image during image acquisition. This added noise contributes to a variation in pixel intensities. To have an accurate model of image, noise is also added to generate the synthetic image as presented in Equation (7.9). Camera noise can be generally simulated by a Gaussian distribution with zero mean $\mu_n = 0$ and standard deviation of σ_n (Petrou & Bosdogianni 1999).

$$I_{syn}(\lambda) = [\hat{I}_{syn}(\lambda) S_{syn}(\lambda) + \gamma_s S b_{syn}(\lambda)] \cos(\theta) + noise. \quad -\frac{\pi}{2} < \theta < \frac{\pi}{2} \quad (7.9)$$

7.2 Monochrome Simulations

Monochrome images are used to explore the performance of the BS filters algorithm for optical back-scatter estimation using Monte-Carlo simulation under different statistical assumptions. Numerous synthetic monochrome images similar to the image shown in Figure 7.3(e) are generated. The spatial distribution of light variation is assumed to

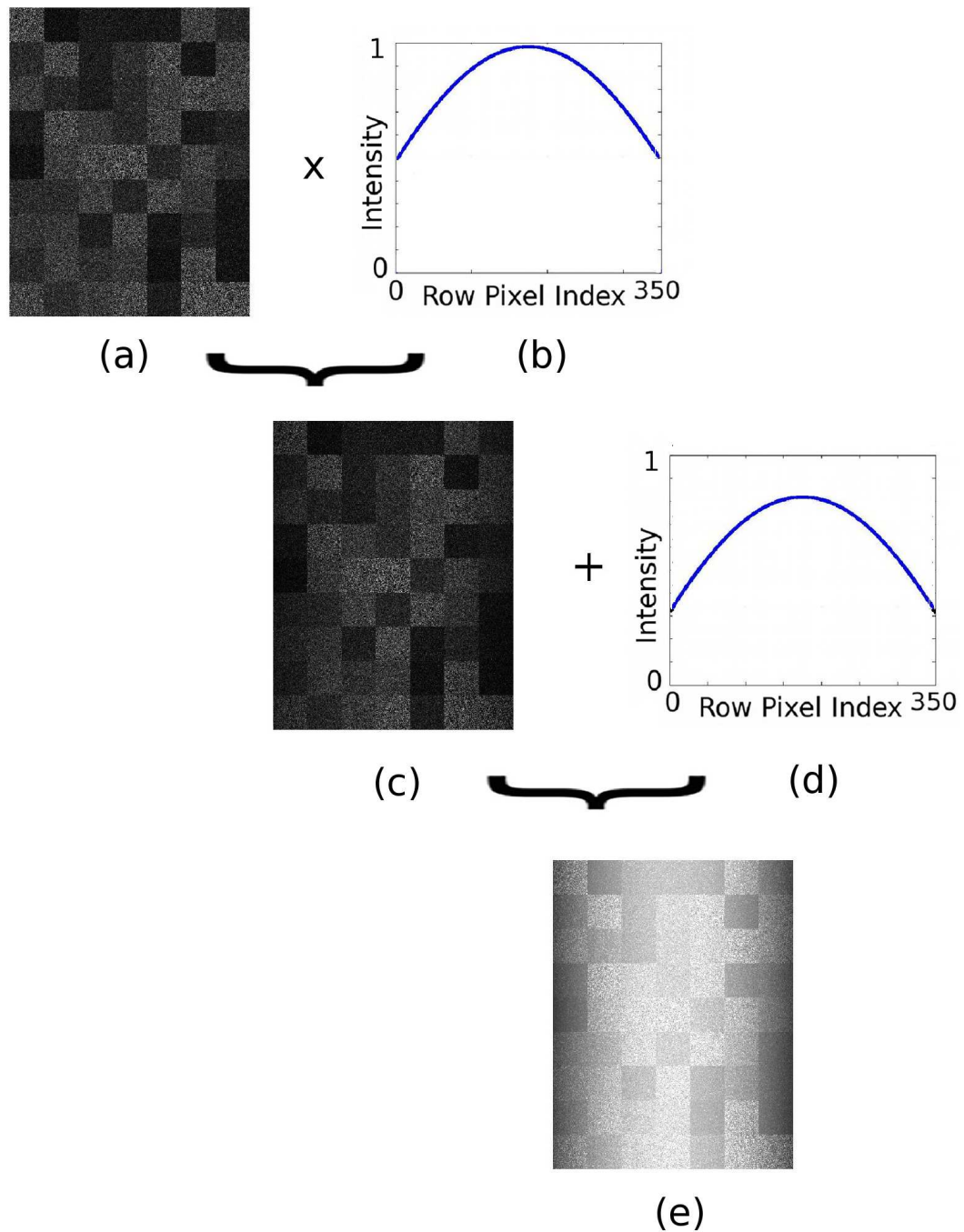


Figure 7.3: The formation of a synthetic monochrome underwater image. a) Synthetic image texture consisted of several blocks. The pixels intensity of each image block follow Beta distribution. b) The line plot of the light intensity variation. c) Synthetic underwater image in clear water condition under direct illumination, where its pattern is shown in (b). d) The line plot of the intensity of optical back-scatter variation. e) Synthetic degraded underwater image.

be known, $\cos(\theta)$, for all simulations unless it is stated. For monochrome images, λ is invariant as a result $S_{syn}(\lambda)$ and $Sb_{syn}(\lambda)$ are set to 1 unless it is stated.

7.2.1 Performance Evaluation

The performances of the BS filter algorithms are evaluated as following. The estimation error in each pixel position, p , is defined as the difference between the real value of optical back-scatter, b , and the estimated value of optical back-scatter, \hat{b}

$$\mathcal{E}_p = b_p - \hat{b}_p. \quad (7.10)$$

Absolute estimation error, \mathcal{E}_i , across all image pixels is calculated by

$$\mathcal{E}_i = \sqrt{\frac{1}{P} \sum_{p=1}^P (b_p - \hat{b}_p)^2}, \quad (7.11)$$

where P is the total number of image pixels. Sometimes, it is required to keep the sign of the estimation error to know whether it is underestimated, positive value of \mathcal{E}_i , or overestimated, which is negative value of \mathcal{E}_i . For this reason \mathcal{E}'_i is defined to calculate for the signed estimation error as

$$\mathcal{E}'_i = \frac{1}{P} \sum_{p=1}^P \mathcal{E}_p. \quad (7.12)$$

The mean estimation errors, absolute (\mathcal{E}_{ave}) and signed (\mathcal{E}'_{ave}) values, for N images are calculated as presented in Equations (7.13) and (7.14).

$$\mathcal{E}_{ave} = \frac{1}{N} \sum_{i=1}^N \mathcal{E}_i, \quad (7.13)$$

$$\mathcal{E}'_{ave} = \frac{1}{N} \sum_{i=1}^N \mathcal{E}'_i. \quad (7.14)$$

The standard deviation of the absolute estimation error, \mathcal{E}_{std} , is

$$\mathcal{E}_{std} = \sqrt{\frac{1}{N-1} \sum_{i=1}^N (\mathcal{E}_i - \mathcal{E}_{ave})^2}. \quad (7.15)$$

The performances of the smoothing filter to obtain light spatial variation is evaluated by finding the difference between the smooth version of the image, \bar{I}_λ , and the synthetic light spatial distribution ($\cos(\theta)$) as shown in Equation (7.16). Note that $\cos(\theta)$ varies horizontally and the spatial variation is similar for all image rows. P , p , i and N are similar as defined before.

$$\mathcal{E}_p^d = \cos(\theta_p) - \bar{I}_p. \quad (7.16)$$

The difference for image (i) is

$$\mathcal{E}_i^d = \sqrt{\frac{1}{P} \sum_{p=1}^P (\mathcal{E}_p^d)^2}, \quad (7.17)$$

and the average difference across N images is

$$\mathcal{E}_{ave}^d = \frac{1}{N} \sum_{i=1}^N \mathcal{E}_i^d. \quad (7.18)$$

7.2.2 Procedures and Results

BS-MinPix Filter Parameter

It is explained in Section 6.1.3 that BS-MinPix filter requires n_{mp} sample pixels of one spatial position (x,y) from n_{mp} number of images to estimate the level of optical back-scatter in that pixel position. The question is what is the best value for n_{mp} ? If n_{mp} is low, then a dark pixel might not present among the sample pixels and this causes estimation error. On the other hand, if n_{mp} is high, then the level of optical back-scatter in sample images might change throughout imaging in real condition and again this is another cause of error. Therefore, it is required to know the optimum value of n_{mp} . A test is done using synthetic degraded images to investigate the optimum value of n_{mp} .

100 series synthetic degraded images in size of $(8 \times 40, 7 \times 40)$ are generated, where each series consisted of n_{mp} number of images. n_{mp} is varied from 1 to 50 and $\sigma_n = 0$. The synthetic optical back-scatter function is $b_{syn} = 100\cos(\frac{\pi x}{3w} - \frac{\pi}{6})$ in intensity range of $[0 \ 255]$. Figures 7.4(a) and (b) present the plots of \mathcal{E}_{ave}/n_{mp} and \mathcal{E}_{std}/n_{mp} respectively. It can be seen that as n_{mp} increases, the values of \mathcal{E}_{ave} and \mathcal{E}_{std} decrease. This means the performance of BS-MinPix filter gets better with higher values of n_{mp} . This is expected, because when number of sample pixels are

high, there is more chance for a dark pixel to be appeared, so the estimation error is lower. Note that this is when the level of optical back-scatter at each pixel position remains unchanged for all sample images. As explained, in real condition the level of optical scattering in each image pixel might change. If it is assumed that the optical scattering condition is constant for capturing 1 second of a video sequence, and the images are extracted with rate of 25 frames per second, then $n_{mp} = 25$ can be taken as the maximum range of n_{mp} . From the \mathcal{E}_{ave}/n_{mp} plot it can be seen that the expected error for $n_{mp} = 25$ is 0.9% ¹, which is very low.

BS-Hist Filter Parameter

In Section 6.1.4, the level of optical back-scatter is estimated using BS-Hist filter by keeping $n_{HB}\%$ of the output image histogram out of visible range. The part of the histogram, which is kept out of visible range should be set according to the level of added noise. If the value of $n_{HB}\%$ is not appropriate with the level of noise, the BS-Hist filter has higher rate of error. In this part, the performance of BS-Hist filter is evaluated experimentally by varying the value of $n_{HB}\%$ for images with added noise.

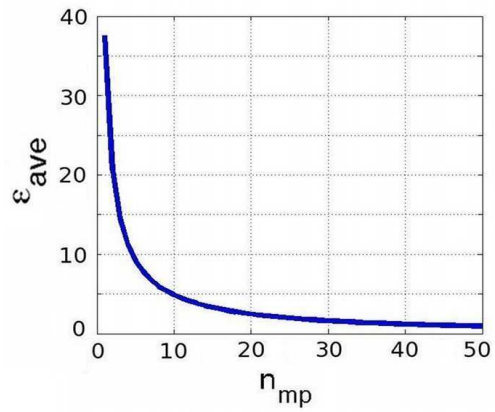
100 images are generated in size of $(8 \times 40, 7 \times 40)$ and with added noise of $\sigma_n = 2$ in intensity range of 255. The synthetic optical back-scatter function is $b_{syn} = 100\cos(\frac{\pi x}{3w} - \frac{\pi}{6})$. $n_{HB}\%$ is varied from 0.2% to 10% in steps of 0.5%.

Figures 7.4(c) and (d) present the plots of $\mathcal{E}_{ave}/n_{HB}\%$ and $\mathcal{E}_{std}/n_{HB}\%$ respectively. It can be seen that \mathcal{E}_{ave} shows the minimum value for $n_{HB}\% = 0.7\%$, which is the value associated to the added noise ($\frac{2}{255}100 = 0.7$). It can be seen for the regions lower or higher than 0.7, \mathcal{E}_{ave} rises. The plot of $\mathcal{E}_{std}/n_{HB}\%$ shows low variation in estimation results ($\mathcal{E}_{std} < 1.3$).

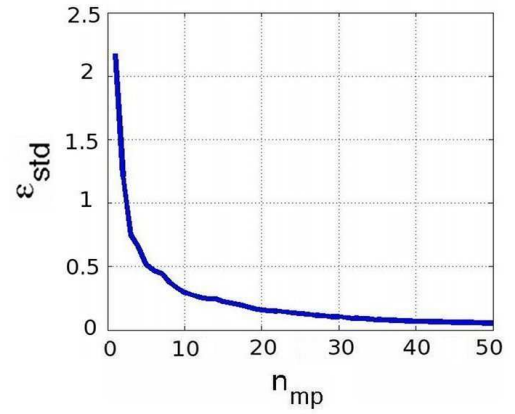
BS-CostFunc Filter Parameter

As mentioned in Section 6.1.5, \bar{I}_λ^{cf} is the local average intensity of a pixel in an image. In practice, \bar{I}_λ^{cf} is estimated using a recursive Gaussian filter with standard deviation of σ_{cf} . The general form of a Gaussian filter is defined in Section 2.3.1. For a Gaussian filter, σ_{cf} is closely related to the size of effective filtering area. If σ_{cf} is too small, the random fluctuation in the pixel intensity cannot be smoothed out. This introduces errors into the estimation of γ from Equation (6.11). On the other hand, if σ_{cf} is too large, the pixels used for averaging are likely to be from more than one region, and the

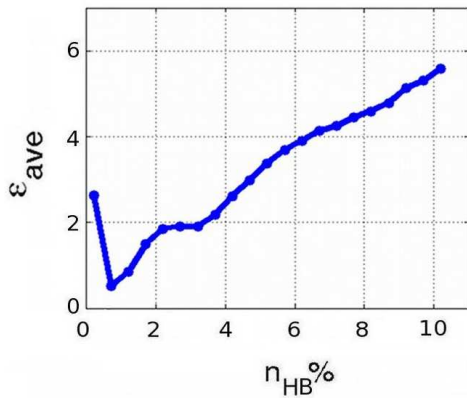
¹ $\mathcal{E}_{ave}(n_{mp} = 25) = 2.4$, in which the expected error is $2.4/255 \times 100 = 0.9\%$.



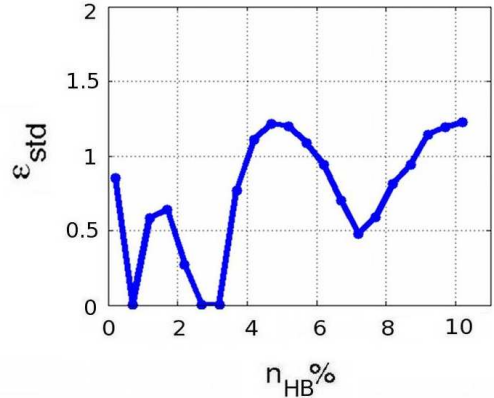
(a)



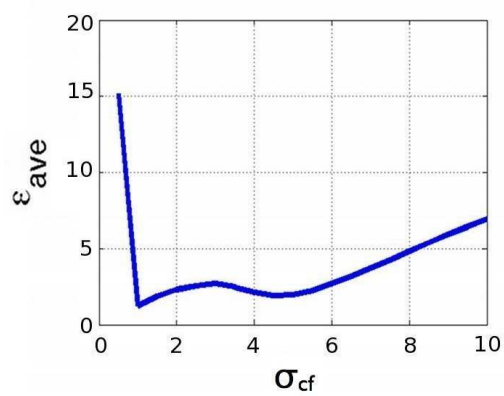
(b)



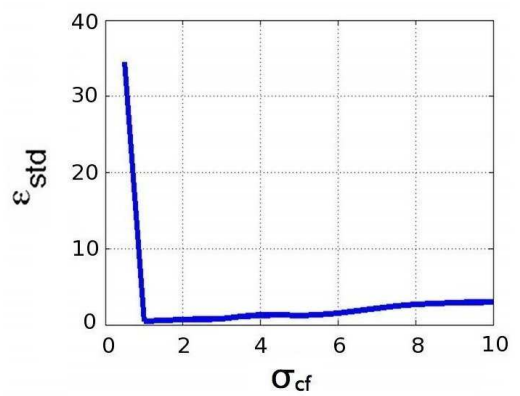
(c)



(d)



(e)



(f)

Figure 7.4: a) The plot of \mathcal{E}_{ave}/n_{mp} , b) The plot of \mathcal{E}_{std}/n_{mp} , c) The plot of $\mathcal{E}_{ave}/n_{HB}\%$, d) The plot of $\mathcal{E}_{std}/n_{HB}\%$ e) The plot of $\mathcal{E}_{ave}/\sigma_{cf}$ f) The plot of $\mathcal{E}_{std}/\sigma_{cf}$.

filtering output no longer reveals the mean intensity of a particular region. Again this causes error in γ estimation and degrades the accuracy of BS-CostFunc filter.

In this part, a test is done to investigate the performance of BS-CostFunc filter by varying σ_{cf} . 100 synthetic degraded images in size of $(8 \times 40, 7 \times 40)$ with $\mu_{min} = 0.03$ and $\sigma_n = 0$ are generated. The value of σ_{cf} is varied from 1 to 10 in steps of 0.5. The synthetic optical back-scatter function is $b_{syn} = 100\cos(\frac{\pi x}{3w} - \frac{\pi}{6})$. Figures 7.4(e) and (f) presents the plots of $\mathcal{E}_{ave}/\sigma_{cf}$ and $\mathcal{E}_{std}/\sigma_{cf}$. It can be seen that for $1.5 < \sigma_{cf} < 5$ both \mathcal{E}_{ave} and \mathcal{E}_{std} are having low values. As σ_{cf} is getting more than 5, both the plots of \mathcal{E}_{ave} and \mathcal{E}_{std} increase, showing higher estimation errors. This confirms that there is a limitation on selecting the filter scale, σ_{cf} .

Region Scale and Quantity

In Section 7.1.1, it is explained that the synthetic images consist several blocks, in which each block represents one surface. The region scale represents the size of each image block, measured by the number of pixels and is denoted by $m \times n$. Region quantity represents the number of blocks in an image and denoted by $M \times N$. In a real image, there are usually a large number of regions with different scales.

The performance of BS-MinPix filter depends on the intensity value of individual pixels. Also, the performance of BS-Hist filter depends on the global image histogram. Therefore, the scale and regions quantity do not effect on the performance of these two filters.

In the Oakley & Bu (2007) study, the region scale is large enough to correctly reveal the statistical distribution of the pixel intensity in each region. This implies that the accuracy of estimation depends on region scale. In this section, the effects of region scale and region quantity on the algorithm performance of BS-CostFunc filter is examined. Several series of synthetic images are generated, in which each series consists of 100 synthetic images with different combinations of region scale and region quantity. The parameters are set as $\mu_{min} = 0.03$, $\sigma_{cf} = 2$, $\sigma_n = 0$, and $b_{syn} = 100\cos(\frac{\pi x}{3w} - \frac{\pi}{6})$ with $w = N \times n$ according to different combinations of region scale and region quantity.

Figures 7.5(a) and (b) present the plots of $\mathcal{E}_{ave}/(M \times N)$ and $\mathcal{E}_{std}/(M \times N)$ for different ranges of region scales. The plots show as region quantity ($M \times N$) increases \mathcal{E}_{ave} and \mathcal{E}_{std} decrease for all region scales. The plot of $\mathcal{E}_{ave}/(M \times N)$ presents that \mathcal{E}_{ave} is higher for smaller region scales across all region quantities. The plot of $\mathcal{E}_{std}/(M \times N)$ shows that the variation of \mathcal{E}_{std} is nearly similar for all region scales across all

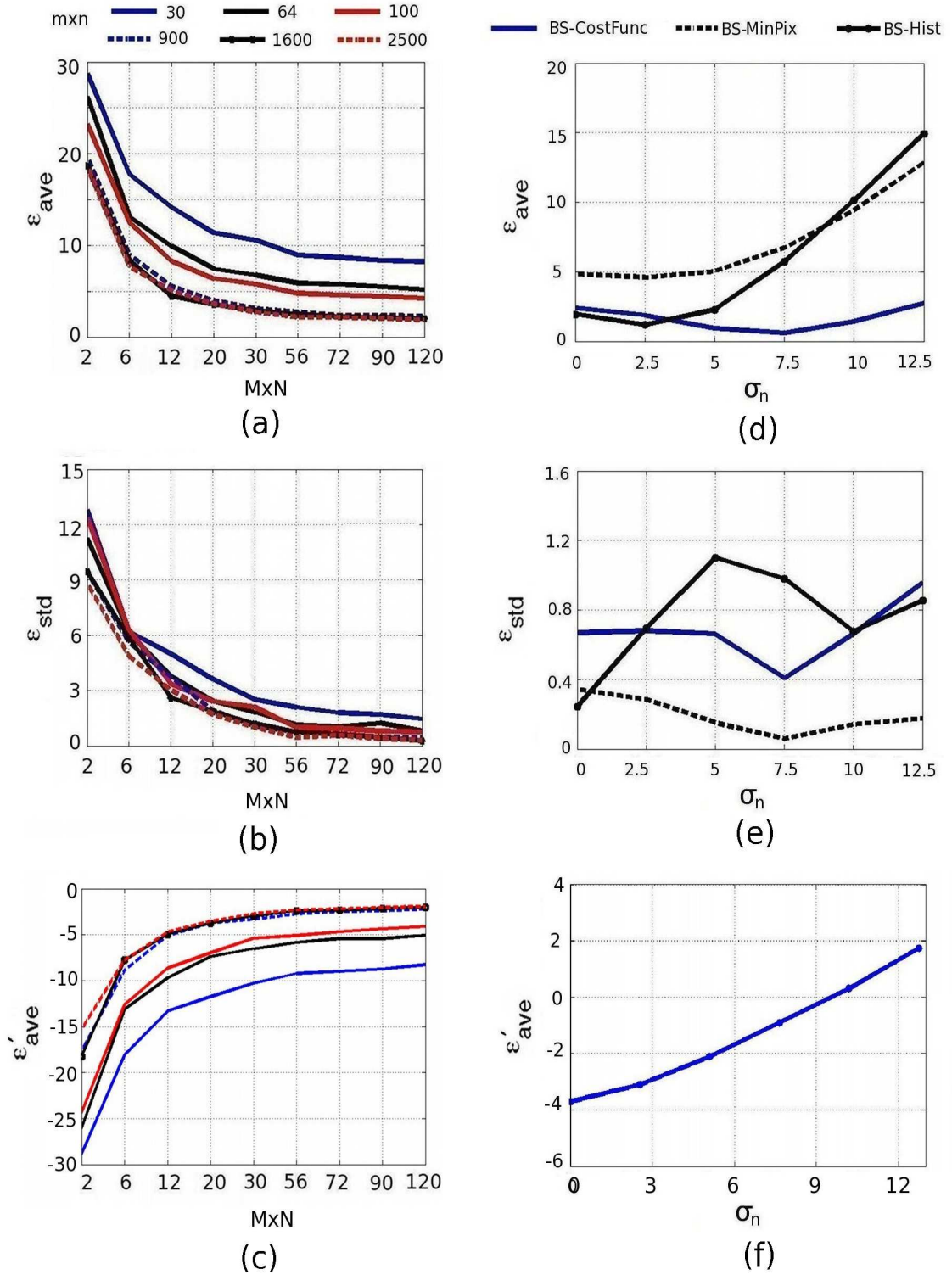


Figure 7.5: a) The plot of $\mathcal{E}_{ave}/(M \times N)$ for different region scales of $m \times n$ for BS-CostFunc filter, b) The plot of $\mathcal{E}_{std}/(M \times N)$ for different region scales of $m \times n$ for BS-CostFunc filter, c) The plot of $\mathcal{E}'_{ave}/(M \times N)$ for different region scales of $m \times n$ for BS-CostFunc filter, d) The plot of $\mathcal{E}_{ave}/\sigma_n$ for BS-CostFunc, BS-MinPix and BS-Hist filters, e) The plot of $\mathcal{E}_{std}/\sigma_n$ BS-CostFunc, BS-MinPix and BS-Hist filters, f) The plot of $\mathcal{E}'_{ave}/\sigma_n$ for BS-CostFunc filter.

region quantities. Figure 7.5(c) presents the plot of $\mathcal{E}'_{ave}/(M \times N)$ for different ranges of region scales. It can be seen that the estimation error is negative for all combinations of $(M \times N)$ and region scales, which means all the estimated values of optical back-scatter are overestimated. As a summary, the plots suggest to have at least 12 regions with region size greater than 100 pixels.

Camera Noise

Synthetic images that are used in simulations so far, representing the scene reflectance and illumination. In real imaging situation there are always some sources of noise added to image as explained in Section 5.3.4. This added noise contributes to some variation in pixel intensities. It is important to know how added noise affects the performance of each BS filter. In this part, the performance of BS filters are evaluated under different levels of noise. 6 series of 100 synthetic images are generated, in which each series corresponds to a level of noise, σ_n . The level of σ_n varies in the range of $[0 \ 12.5]$ in steps of 2.5. The images are in size $(8 \times 40, 7 \times 40)$, with parameters setting to $\mu_{min} = 0.03$, $n_{mp} = 10$, $n_{HB}\% = 2.5\%$, $\sigma_{cf} = 2$ and $b_{syn} = 100\cos(\frac{\pi x}{3w} - \frac{\pi}{6})$.

Figures 7.5(d) and (e) present the plots of $\mathcal{E}_{ave}/\sigma_n$ and $\mathcal{E}_{std}/\sigma_n$. From the plot of $\mathcal{E}_{ave}/\sigma_n$, it can be seen that the performance of BS-MinPix falls more with added noise with respect to the other BS filters for all noise levels. The performance of BS-CostFunc and BS-Hist filters are similar for very low level of noise ($\sigma_n \leq 2.5$). But for higher level of noise, $\sigma_n > 2.5$, the estimation error of BS-Hist filter dramatically increases, while the performance of BS-CostFunc is unchanged with respect to low noise level. Also, the plot of $\mathcal{E}_{std}/\sigma_n$ shows that the error variation is very low (< 1.2) for all BS filters.

The results suggest that among the three BS filters, the performance of BS-CostFunc filter is the best in real imaging condition, where there is always some added noise. Figure 7.5(f) presents the plot of $\mathcal{E}'_{ave}/\sigma_n$. It can be seen that for noise levels less than 9, $\sigma_n < 9$, the estimated optical back-scatter values are overestimated and for higher noise levels, $\sigma_n > 9$, they are underestimated.

Minimum of μ_B

It is explained in Section 7.1.1 that the mean value, μ_B , is required to generate each image block. The mean is restricted within a range $0 < \mu_B < 0.36$. The minimum range of μ_B , $\mu_B(min)$, is not defined to a specific value. The value of $\mu_B(min)$ is important on the performances of BS filters, because it determines the level of dark

pixels. In this part a test is done to investigate the performances of BS filters by varying $\mu_B(min)$.

20 series of 100 synthetic degraded images in size of $(8 \times 40, 7 \times 40)$ and with $\sigma_n = 0$ are generated, in which each series corresponds to a different $\mu_B(min)$. The value of $\mu_B(min)$ vary in range of $[0.001 \ 0.1]$ in steps of 0.005. The synthetic optical back-scatter function is $b_{syn} = 100\cos(\frac{\pi x}{3w} - \frac{\pi}{6})$. Figures 7.6(a) and (b) present the plots of $\mathcal{E}_{ave}/\mu_B(min)$ and $\mathcal{E}_{std}/\mu_B(min)$ for three BS filters.

It can be seen, as $\mu_B(min)$ increases, the value of \mathcal{E}_{ave} increases for all BS filters. The increment rate is higher in BS-CostFunc filter and is lower in BS-Hist. Also, it can be seen that when $\mu_B(min) < 0.01$, BS-CostFunc shows lower error in comparison with two other BS filters. From the plot of $\mathcal{E}_{std}/\mu_B(min)$, it can be seen that \mathcal{E}_{std} for BS-Hist is less steady with respect to BS-CostFunc and BS-MinPix filters. Figure 7.6(c) presents the plot of $\mathcal{E}'_{ave}/\mu_B(min)$. It can be seen that for all values of $\mu_B(min)$ the estimated optical back-scatter values are overestimated.

Optical Back-scatter Level and Spatial Distribution

In Section 7.1.1, it is explained that the spatial distribution of the light source can be simulated by a positive truncated cosine function, as shown in Equation (7.7). The hump part of the cosine function represents the direction of the light source. When the direction of light source varies, the spatial distribution of light varies, and as a result the spatial distribution of the optical back-scatter varies. Therefore, it is expected that different light spatial distributions have a similar effect on the performance of the BS-CostFunc filter. Also, the level of optical back-scatter changes due to several parameters as discussed in Section 2.1.3. It is important to know how BS-CostFunc filter performs with different levels of optical back-scatter.

Different light spatial distributions can be synthesized by varying θ ($-\frac{\pi}{2} < \theta < \frac{\pi}{2}$) in cosine function of Equation (7.7), and different levels of optical back-scatter can be simulated by varying the value of γ_s of Equation (7.7). In this section, the performance of BS-CostFunc algorithm is investigated for different values of θ and γ_s .

Several series of 100 synthetic degraded images in size $(8 \times 40, 7 \times 40)$ are generated with $\mu_{min} = 0.03$, $\sigma_{cf} = 2$ and $\sigma_n = 0$, where each series is a different combination of γ_s and θ . The value of γ_s is varied from 10 to 200. Four different θ are used, which represent for different light spatial distribution as shown in Figure 7.7(a). Figures 7.7 (b) and (c) present the plots of $\mathcal{E}_{ave}/\gamma_s$ and $\mathcal{E}_{std}/\gamma_s$ for four different values of θ . It can be seen that the trend of the plots are similar for different values of θ . This indicates that

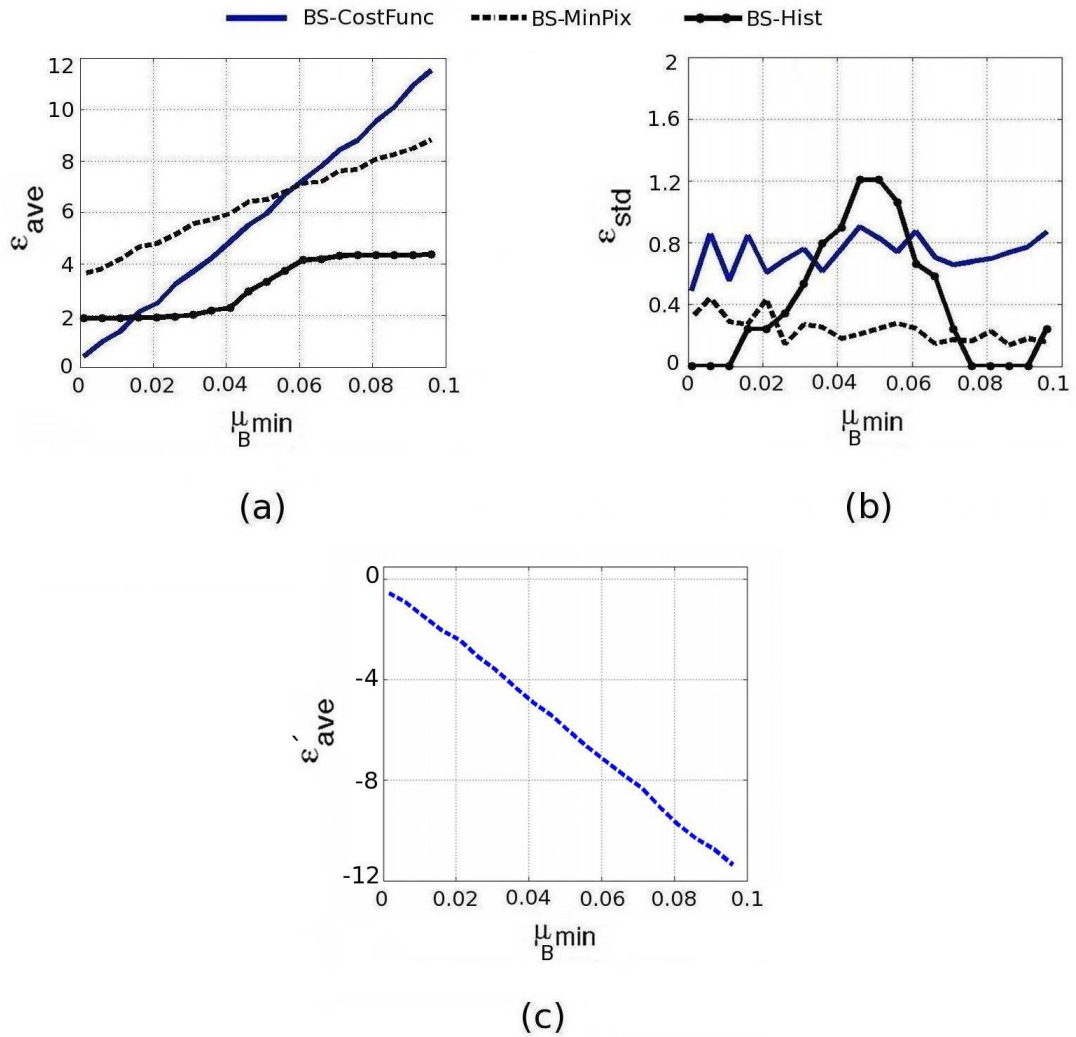


Figure 7.6: a) The plot of $\mathcal{E}_{ave}/\mu_B(\text{min})$ for BS-CostFunc, BS-MinPix and BS-Hist filters. b) The plot of $\mathcal{E}_{std}/\mu_B(\text{min})$ for BS-CostFunc, BS-MinPix and BS-Hist filters. c) The plot of $\mathcal{E}'_{ave}/\mu_B(\text{min})$ for BS-CostFunc.

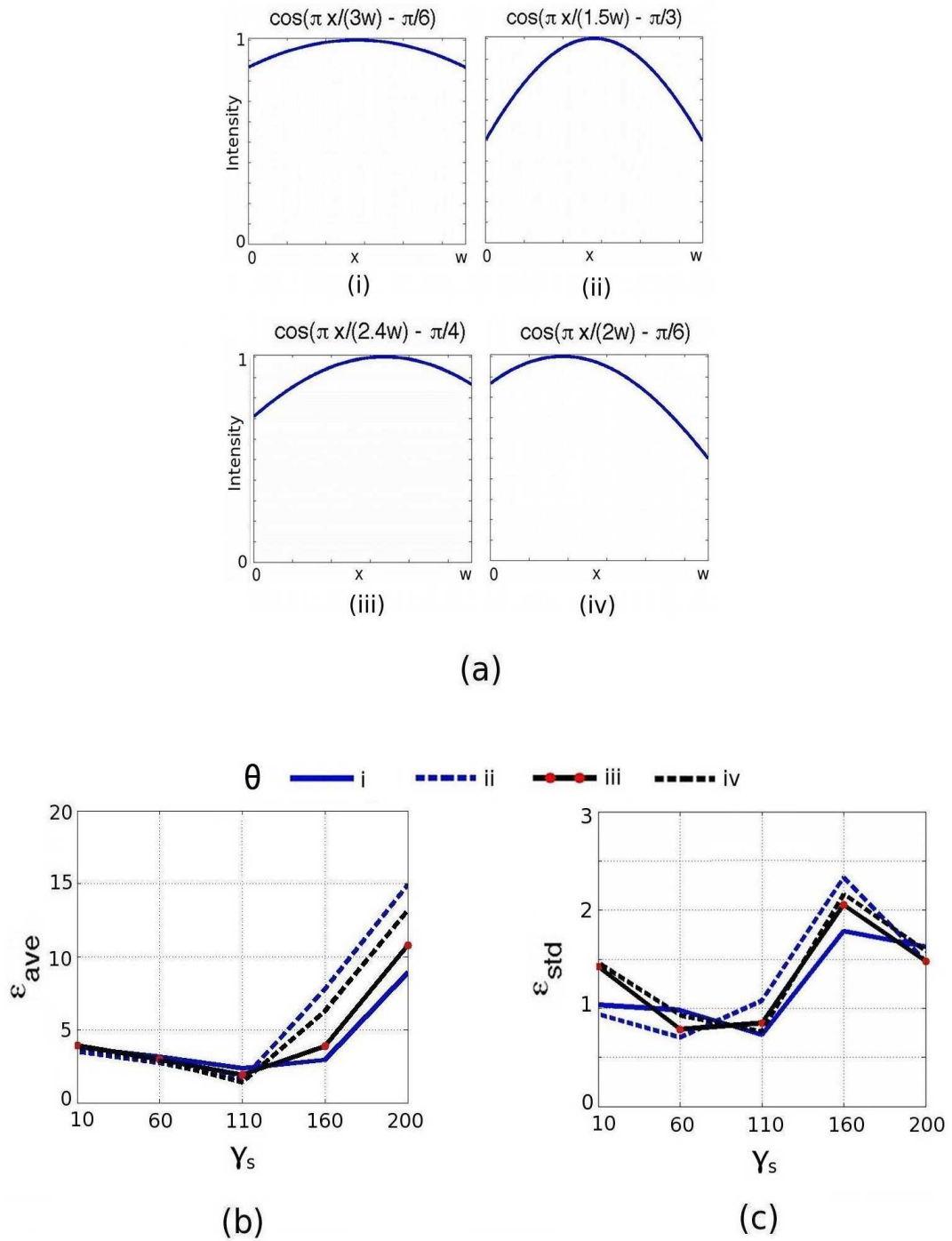


Figure 7.7: a) Different synthetic light variation patterns using different θ . w is the size of an image row and x is the row pixel index. b) The plot of $\mathcal{E}_{ave}/\gamma_s$ using BS-CostFunc filter for different θ , c) The plot of $\mathcal{E}_{std}/\gamma_s$ using BS-CostFunc filter for different θ .

the performance of BS-CostFunc filter is independent of the light spatial distribution (or the direction of light source). The plots also show that the expected error is nearly similar for low and medium level of optical back-scatter, but for a very high level of optical back-scatter (high γ_s) the estimation error, \mathcal{E}_{ave} , increases.

Illumination Intensity

When the intensity of light source is low, it means that there is less light interacting with the scattering particles and this results in less optical back-scatter. Therefore, it is expected that the estimation error should be lower for lower light intensity. This is important, because the light intensity typically varies with wavelength. The parameter $S_{syn}(\lambda)$ in Equation (7.2), represents for the synthetic light intensity spectra. So far $S_{syn}(\lambda)$ was set to 1. In this section, the performance of BS-CostFunc filter is evaluated for different light intensity by varying the value of $S_{syn}(\lambda)$.

100 synthetic images are generated for different values of $S_{syn}(\lambda)$, which varies in the range [0.05 1] in steps of 0.02. The images are in size of $(8 \times 40, 7 \times 40)$ and the noise level is set to $\sigma_n = 2$. The synthetic optical back-scatter function is $b_{syn} = 100Sb_{syn}(\lambda)\cos(\frac{\pi x}{3w} - \frac{\pi}{6})$, where the synthetic optical back-scatter spectrum is assumed to follow the light spectrum $Sb_{syn}(\lambda) = S_{syn}(\lambda)$. Figure 7.8(a) presents the plot of \mathcal{E}'_{ave} versus intensity. It can be seen that the optical back-scatter values are overestimated, and also as intensity increases, the estimation error, \mathcal{E}'_{ave} , increases as well.

Filter Parameter σ_B

According to the proposed back-scatter model (Equation (6.11)), the accuracy of b_λ not only depends on the value of γ parameter, but depends on the smoothed version of the image, \bar{I}_λ . It is explained in Section 6.1 that \bar{I}_λ can be obtained by applying a recursive Gaussian filter with standard deviation of σ_B . The size of σ_B should be selected according to the image size. In this simulation, the spatial distribution of light varies horizontally across the image row. Thus, the size of image row is considered. \bar{I}_λ should be smoothed in such a way that removes all the fluctuations due to the image content, while keeping the light spatial variation.

A simulation is done to investigate the amount of difference between the synthetic light variation and the model of \bar{I}_λ by varying the amount of σ_B . Two series of 100 images are generated, with size of (400×1050) and (400×1400) . The function of light spatial variation is $\cos(\frac{\pi x}{3w} - \frac{\pi}{6})$. The value of $\frac{\sigma_B}{W}$ is varied from 0.07 to 0.25 in steps

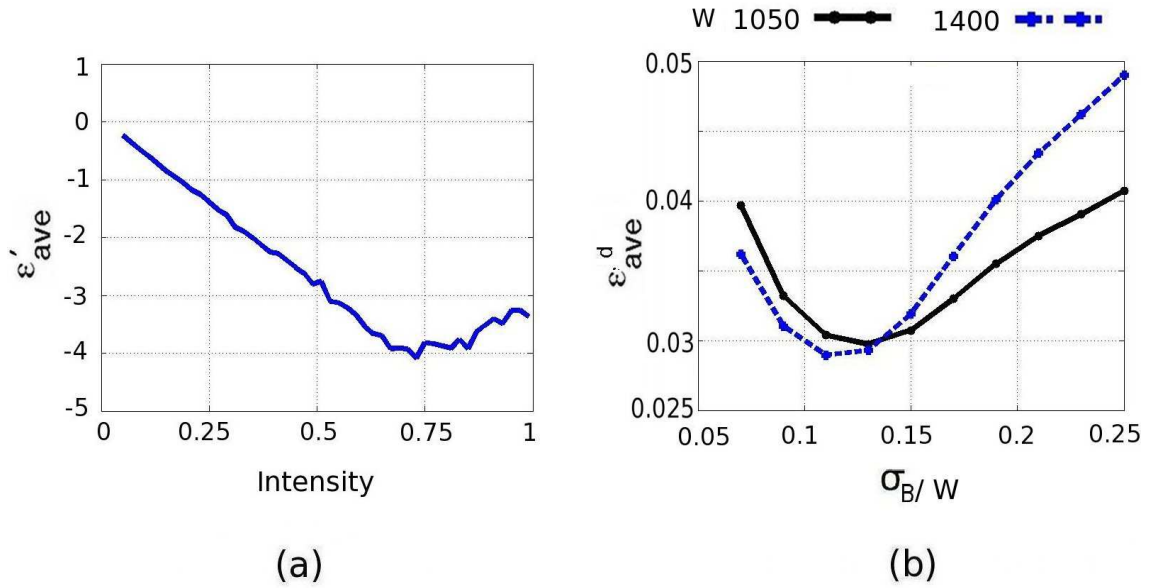


Figure 7.8: a) The plot of \mathcal{E}'_{ave} versus intensity, b) The plot of \mathcal{E}^d_{ave} versus $\frac{\sigma_B}{W}$ for two image widths, $W=1050$ and $W=1400$ pixels.

of 0.02. \bar{I}_λ is normalized to be in the range $[0 \ 1]$, the same range as synthetic optical back-scatter function. The difference between the synthetic light spatial distribution and \bar{I}_λ is calculated for 100 images in both series. Figure 7.8(b) presents the plot of the mean difference, \mathcal{E}^d_{ave} , versus $\frac{\sigma_B}{W}$. It can be seen when $0.1 < \frac{\sigma_B}{W} < 0.15$ the difference shows the lowest value. For higher and lower values of $\frac{\sigma_B}{W}$ the difference rises. For example for image widths of $W=1050$, σ_B can be selected in range of $[105 \ 158]$ to give the best fit with light variation. This confirms that the size of σ_B should be selected with respect to the image size. Also, it can be concluded that the the model of light variation, \bar{I}_λ , introduces an error of 3% in the estimation.

7.3 Colour Simulations

Colour images may be represented by multispectral images in the visible range of 400nm - 720nm. To enhance a degraded colour underwater image, the effect of optical back-scatter in each spectral band should be compensated. One of the main requirements when processing a colour image is that the spectral variation remains unchanged. The aim of simulations in this section is to investigate how much colour difference is caused by the BS-CostFunc filter. First, the generation of a synthetic colour image and

the performance evaluations are explained. Then the simulations are presented.

7.3.1 Synthetic Colour Image Generation

A synthetic colour image is generated in form of multispectral images with 33 narrow spectral bands of 10nm and in visible range of 400nm to 720nm. Equation (7.9) is used to generate the image intensity of each band. Note that the intensity information in adjacent bands is correlated in natural images. If an independent image is generated for each spectral band, the correlation between bands would be zero. For that reason, one image intensity distribution is generated and used for every 4 adjacent bands. The parameters set as following for all of the simulations unless it is stated. The images are of size $(8 \times 40, 7 \times 40, 33)$, with $\mu_B(min) = 0.03$. The synthetic optical back-scatter function is $b_{syn} = 100\cos(\frac{\pi x}{3w} - \frac{\pi}{6})$. The values $S_{syn}(\lambda)$ and $Sb_{syn}(\lambda)$ are taken from the empirical values for the illumination of the halogen lamp and in medium level of water turbidity with emulsion paint particles respectively.

Multispectral images are corrected for the dark current noise as explained in Section 3.2.3. The main noise remaining in multispectral images is the shot noise. The empirical value of shot noise for the maximum intensity level for the Hamamatsu ORCA-ER hyperspectral camera is calculated in Section 5.3.4 as $\sigma_n \approx 2$ and this value is used for colour simulations. As the light intensity varies spectrally, the value of shot noise for different wavelengths varies as well. The noise spectrum is synthesized by

$$\sigma_n(\lambda) = \sigma_n S_{syn}(\lambda). \quad (7.19)$$

7.3.2 Performance Evaluation

The performance of the proposed method to improve the contrast of a colour image is evaluated by calculating the mean estimation error, \mathcal{E}'_{ave} , and the amount of colour difference (CD) introduced to the improved image pixel. The mean estimation error, \mathcal{E}'_{ave} , is similar as defined by Equation (7.14). To calculate the CD, the images should be in $L^*a^*b^*$ colour space, and a white reference is used. The calculations of mapping the multispectral images to XYZ colour space, and converting XYZ to $L^*a^*b^*$ or sRGB and vice versa, and the CD are done using Westland & Ripamonti (2004) algorithms. The CIE A_{64} is used as the white reference, because the correlated colour temperature of a 100 W halogen lamp is 3000 K, which is very close to the CCT of an incandescent 120W light bulb (CCT = 2860 K), which is for the CIE A_{64} (Westland & Ripamonti

2004).

To evaluate the colour difference in an image, the mean colour difference, CD_m , for all image pixels is calculated from

$$CD_m = \frac{1}{P} \sum_{p=1}^P CD_p, \quad (7.20)$$

where p and P are similar as defined before.

7.3.3 Simulation 1

The aim of this simulation is to show that a degraded colour image, either in narrow spectral bands or in wide spectral bands, can be improved by compensating for the effect of optical back-scatter with colour fidelity if the level of optical back-scatter is known for each spectral band.

This is first shown mathematically as follows, and then experimentally by Simulation 1. Suppose $R_d(\lambda)$, $R_c(\lambda)$ and $R_{bs}(\lambda)$ are the reflected light from the scene in murky condition, the reflected light from the scene in clear condition and the reflected light from the particles in turbid water respectively. It is explained in Section 3.2.3, that the level of optical back-scatter in narrow bands can be assumed constant at each pixel position. Here, a and $R_{bs}(\lambda)$ is assumed to be spectrally invariant at each pixel position.

$$R_d(\lambda) = aR_c(\lambda) + R_{bs}(\lambda), \quad (7.21)$$

Equations (2.24) - (2.26) are used to map the images from 33 to 3 spectral bands. Therefore, X_d is

$$X_d = \int_0^\lambda R_d(\lambda)S(\lambda)\bar{x}(\lambda), \quad (7.22)$$

where $\bar{x}(\lambda)$ and $S(\lambda)$ are similar as defined in Section 2.4.3. X_d can be written by substituting Equation (7.21) instead of $R_d(\lambda)$

$$X_d = \int_0^\lambda (aR_c(\lambda) + R_{bs}(\lambda))S(\lambda)\bar{x}(\lambda)d\lambda, \quad (7.23)$$

$$X_d = \int_0^\lambda (aR_c(\lambda)S(\lambda)\bar{x}(\lambda) + R_{bs}(\lambda)S(\lambda)\bar{x}(\lambda))d\lambda, \quad (7.24)$$

$$X_d = \int_0^\lambda aR_c(\lambda)S(\lambda)\bar{x}(\lambda)d\lambda + \int_0^\lambda R_{bs}(\lambda)S(\lambda)\bar{x}(\lambda)d\lambda. \quad (7.25)$$

$\int_0^\lambda aR_c(\lambda)S(\lambda)\bar{x}(\lambda)$ and $\int_0^\lambda R_{bs}(\lambda)S(\lambda)\bar{x}(\lambda)$ are the mapped clear image, X_c , and optical back-scatter, X_{bs} , in XYZ colour space respectively. Therefore, X_d can be written as

$$X_d = X_c + X_{bs}. \quad (7.26)$$

By rearranging Equation (7.26), X_c can be found as

$$X_c = X_d - X_{bs}. \quad (7.27)$$

This also can be extended for Y_d and Z_d as

$$Y_c = Y_d - Y_{bs}. \quad (7.28)$$

$$Z_c = Z_d - Z_{bs}. \quad (7.29)$$

Equations (7.27) - (7.29) confirm that the result of compensating a degraded image with wide spectral band with known values of X_{bs} , Y_{bs} and Z_{bs} is similar to the results of compensating a degraded image with narrow spectral bands with known value of $R_{bs}(\lambda)$.

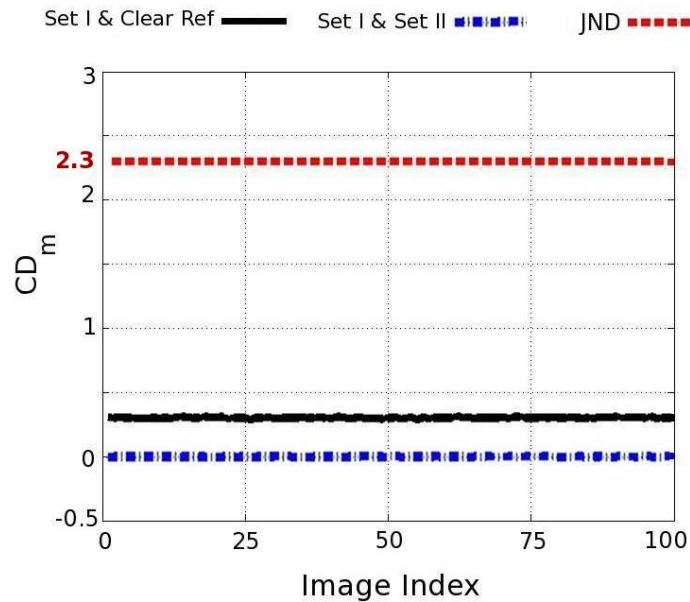


Figure 7.9: The plot of mean colour difference, CD_m , for 100 images between Set I & Set II (dash-dotted line), and Set I and the clear reference image (solid line).

Simulation 1 confirms this experimentally. Two series of 100 synthetic colour images, which are the degraded and the correspondence clear reference, are generated with 33 narrow spectral bands. The degraded images are compensated for the effect of optical back-scatter using known synthetic back-scatter in two different ways. The first way is to process the images in narrow spectral bands. The image in each spectral band is compensated for the effect of known optical back-scatter in the correspondence band. The output images of this series is called Set I. The second way is to map the degraded images and the known optical back-scatter to XYZ colour space, and then compensating each of the X, Y and Z bands for the effect of optical back-scatter. The output images of this series is called Set II. The clear reference images and the improved images in Set I are mapped to XYZ. For comparison the images are converted to $L^*a^*b^*$ colour space and the colour difference between Set I and clear reference image, and Set I and Set II are calculated and presented in Figure 7.9 by the solid line and the dash-dotted line respectively. It can be seen that the mean colour difference, CD_m , between Set I and the clear reference is around 0.3 for all 100 test images, which is below the JND value of 2.3. The CD_m between Set I and Set II is near zero, $CD_m = 5 \times e^{-14}$, for all 100 images. This means that the colour information in Set I matches with that in Set II. The results confirm that the a degraded underwater colour image can be improved with colour fidelity if the level of optical back-scatter is known. Moreover, the results show that processing degraded colour images in wide spectral bands does not introduce any colour difference with respect to processing images with narrow spectral bands.

Sample of synthetic images converted to sRGB in clear, degraded and improved image in Set I and Set II are presented in Figure 7.13(a) - (d) respectively.

7.3.4 Simulation 2

The aim of this simulation is to investigate the amount of colour difference due to the optical back-scatter estimation error in colour images with narrow spectral bands.

It is shown in monochrome simulations (Section 7.2), that the level of optical back-scatter can be estimated by BS-CostFunc filter, but with some estimation error. Also, the plot of Figure 7.8(a) shows that the estimation error varies by light intensity. The light intensity varies spectrally and as a result, the estimation error is spectrally variant due to the noise effects.

The estimation error spectra can be found from the intensity in each spectral band (light source power spectrum) and the corresponding level of estimation error from

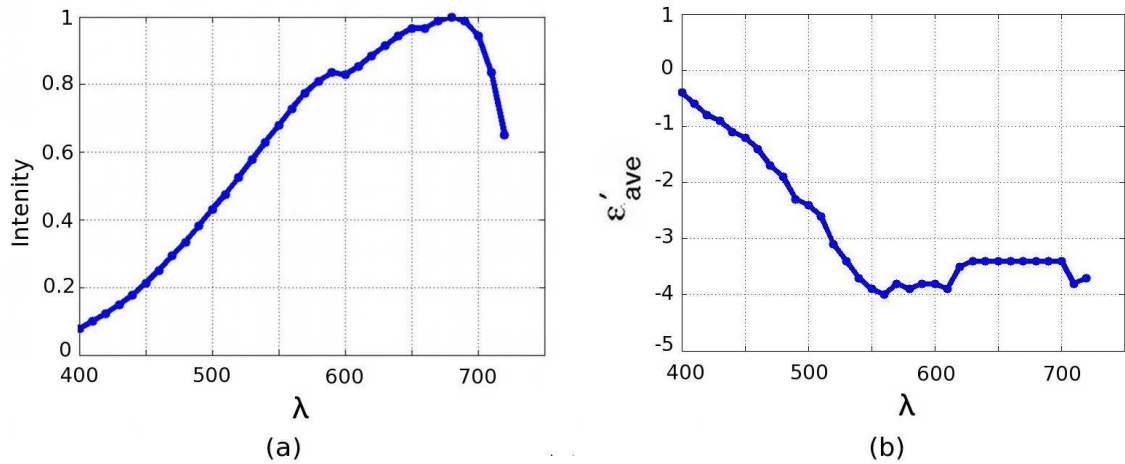


Figure 7.10: The plots of a) the halogen lamp power spectrum, b) the estimation error spectra.

Figure 7.8(a). The plot of the power spectrum of the halogen lamp and the estimation error spectra are presented in Figures 7.10 (a) and (b) respectively.

The estimation error causes variation in the pixel value of each band, and as a result causes a change in the pixel spectrum. The change in pixel spectrum results in a change in colour. The question is how much colour difference is introduced to the output image due to the estimation error? Also, human vision system has limitation in recognising small colour differences as explained in Section 2.4.3, so it is important to know that whether the colour difference due to the estimation error can be sensed by the human vision system.

The expected colour difference due to the estimation error in each band is estimated. For each spectral band, the estimation error is added to a sample of synthetic clear image. The original image and the image with added estimation error are then mapped from 33 bands to 3 bands in form of XYZ and then converted to $L^*a^*b^*$. The amount of colour difference between these two images is calculated as $CD_m = 1.6$. To confirm this, the amount of colour difference due to the BS-CostFunc filter estimation error in each band is investigated experimentally in Simulation 2.

Two series of 100 synthetic colour images, the same as in Simulation 1, are used. The optical back-scatter in each narrow spectral band is estimated by BS-CostFunc with $\sigma_{cf} = 3$. The degraded images in each spectral band are compensated for the effect of optical back-scatter. This set of images is called Set III. A sample synthetic image in Set III, which is converted to sRGB, is presented in Figure 7.13(e). The

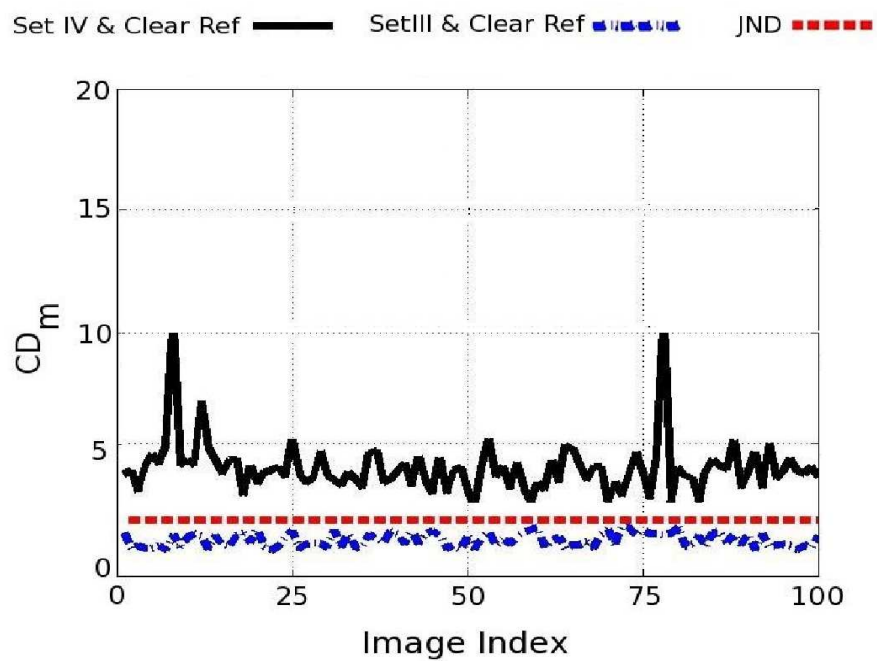


Figure 7.11: The plot of mean colour difference, CD_m , for 100 images between Set III and the clear reference image (dash-dotted line), and Set IV and the clear reference image (solid line).

improved images with their correspondence clear reference images are mapped to 3 bands in form of XYZ and converted to $L^*a^*b^*$ colour space. The mean colour difference, CD_m , between the original image and Set III are calculated for 100 images and presented in Figure 7.11 with dash-dotted line. It can be seen that for 100 images, the value of CD_m is constantly less than JND value of 2.3 for all 100 images. This confirms that the amount of colour difference due to the error of BS-CostFunc filter is less than the eye sensitivity threshold .

7.3.5 Simulation 3

The aim of this simulation is to investigate the amount of estimation error for colour images with wide spectral bands.

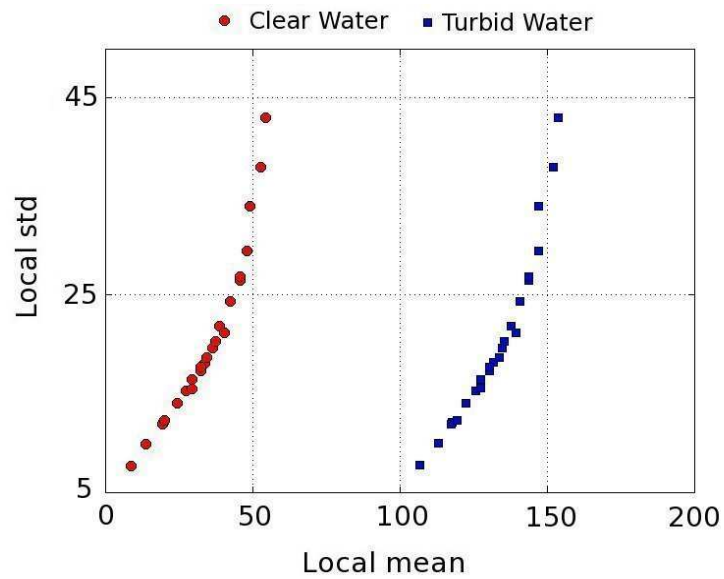
In real life images are generally captured in form of RGB, which has 3 highly correlated spectral bands. In this part, we would like to know how BS-CostFunc algorithm performs with images in wide spectral bands, such as RGB. BS-CostFunc uses the extended Oakley-Bu cost function. The basis of Oakley-Bu cost function is that the relation between the standard deviation and mean of image regions/surfaces can reveal the level of extra lightness due to optical back-scatter in a degraded image.

To show this, two sample monochrome synthetic clear and degraded underwater images at 600nm from test images that used in Simulation 1 are used. The term local is used here to refer for each image block or region.

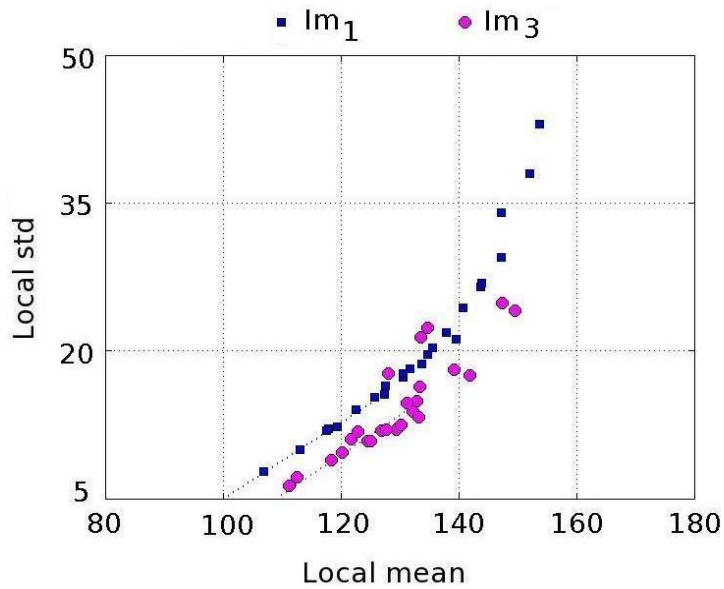
The synthetic images have check-board pattern, in which each block represents for each image region. The standard deviation of each image block (std_b) is plotted versus the correspondence mean (m_b) of that block for clear and degraded condition and presented in Figure 7.12(a) with red circle and blue square marks respectively.

It can be seen that the first part of both plots are linear. The expansion of the plot intercepts with m_b axis around zero for the image in clear water condition, whereas for the degraded image the plot is shifted in local mean axis toward 100, which is the level of synthetic optical back-scatter. Assume an image, Im_3 , is consisted of two uncorrelated images Im_1 and Im_2 , with local mean of m_{b1} and m_{b2} , and local standard deviation of $std_{b1} = c'm_{b1}$ and $std_{b2} = c'm_{b2}$, where c' is a constant value. The mean is a linear operation, so the local mean of Im_3 can be found by

$$m_{b3} = \frac{m_{b1} + m_{b2}}{2}. \quad (7.30)$$



(a)



(b)

Figure 7.12: The plot of local standard deviation (std_b) versus local mean (m_b) for a) synthetic images in clear and turbid water conditions, b) two degraded synthetic images in turbid water condition at 600nm. Im_1 is one single image and Im_3 is from the combination of two degraded images, Im_1 and Im_2 at 600nm.

The standard deviation is not a linear operation and for Im_3 can be found by

$$std_{b3} = \sqrt{\frac{std_{b1}^2 + std_{b2}^2 + 2cov(b1, b2)}{2}}. \quad (7.31)$$

As Im_1 and Im_2 are uncorrelated, $cov(b1, b2) = 0$, and std_{b3} can be written as

$$std_{b3} = \sqrt{\frac{std_{b1}^2 + std_{b2}^2}{2}}, \quad (7.32)$$

$$std_{b3} = \sqrt{\frac{(c'm_{b1})^2 + (c'm_{b2})^2}{2}}, \quad (7.33)$$

$$std_{b3} = c' \sqrt{\frac{m_{b1}^2 + m_{b2}^2}{2}}. \quad (7.34)$$

From Equation (7.30), m_{b3}^2 can be written as

$$m_{b3}^2 = \frac{m_{b1}^2 + m_{b2}^2 + 2m_{b1}m_{b2}}{4}. \quad (7.35)$$

By rearranging Equation (7.35)

$$m_{b1}^2 + m_{b2}^2 = 4m_{b3}^2 - 2m_{b1}m_{b2}. \quad (7.36)$$

By substituting Equation (7.36) in Equation (7.34)

$$std_{b3} = c' \sqrt{2m_{b3}^2 - m_{b1}m_{b2}}. \quad (7.37)$$

Equation (7.37) shows that the amount of difference is related to m_{b1} and m_{b2} . As a result the local standard deviation and mean of the combined image are not proportional.

$$std_{b3} \not\propto m_{b3}. \quad (7.38)$$

To show the relation of std_{b3} and m_{b3} , two synthetic degraded images, Im_1 and Im_2 , at 600nm with same level of optical back-scatter are used. The plots of local standard deviation versus local mean for Im_1 and Im_3 ($Im_3 = Im_1 + Im_2$) are plotted and presented in Figure 7.12(b) by blue square and magenta circle markers respectively. It can be seen that for Im_1 , the expansion of the plot intercepts at 100, whereas for Im_3 the expansion of the plot intercepts with some difference from 100. This shows that the result of local std_{b3} versus m_{b3} plot is less useful when analysing the level of optical back-scatter.

Colour images in wide spectral bands, such as XYZ and RGB, can be assumed to be the sum of several images of narrow spectral bands. The cost function algorithm is based on the relation between the standard deviation and mean of each image region. Also, it is shown in Equation (7.38) that the standard deviation of the combined image regions is not proportional to the mean. The amount of difference is approximately related to the local mean of the narrow spectral band images ($m_{b1}m_{b2}$). If the local mean values are low, the amount of difference is lower and causes less error in the performance of cost function algorithm. But, if the local means have high values, then the difference becomes high and causes more error.

Therefore, when processing colour images with wide spectral bands, the cost function algorithm operates with extra estimation error, in which the amount of error relates to the local mean of narrow band images. If the local mean is low, the amount of error is lower as well.

Simulation 3 is done to investigate how much colour difference is introduced to this extra estimation error. Two series of 100 synthetic colour images, same images as used for Simulation 1, are used in this simulation. Each image is mapped to XYZ colour space. Then, the level of optical back-scatter in each band is estimated and used to compensate for the effect of optical back-scatter. This set of images are called as Set IV. The clear reference and Set IV images are converted to $L^*a^*b^*$ colour space and CD_m between these two images are calculated and plotted in Figure 7.11 with solid line. The colour difference is $CD_m \approx 4$, which is higher than the level of eye sensitivity threshold, JND. A sample of synthetic image in Set IV is converted to sRGB and presented in Figure 7.13(f). It can be seen that the processed image is darker, which is because of the level of noise. The image colour is visually similar to the clear reference image, even if the colour difference is in a range that can be detected by eye. In other word, no colour shift is visually obvious. The reason for colour difference above JND is that, the colour difference is calculated by ΔE_{ab} , which considers the difference between both lightness (L^* in $L^*a^*b^*$ colour space) and colour (a^* , b^* in $L^*a^*b^*$ colour space). When the image is darker, even there is no difference in colour, still it affects on the value of colour difference. This shows that the method can be successfully applied to colour images in wide spectral bands as well.

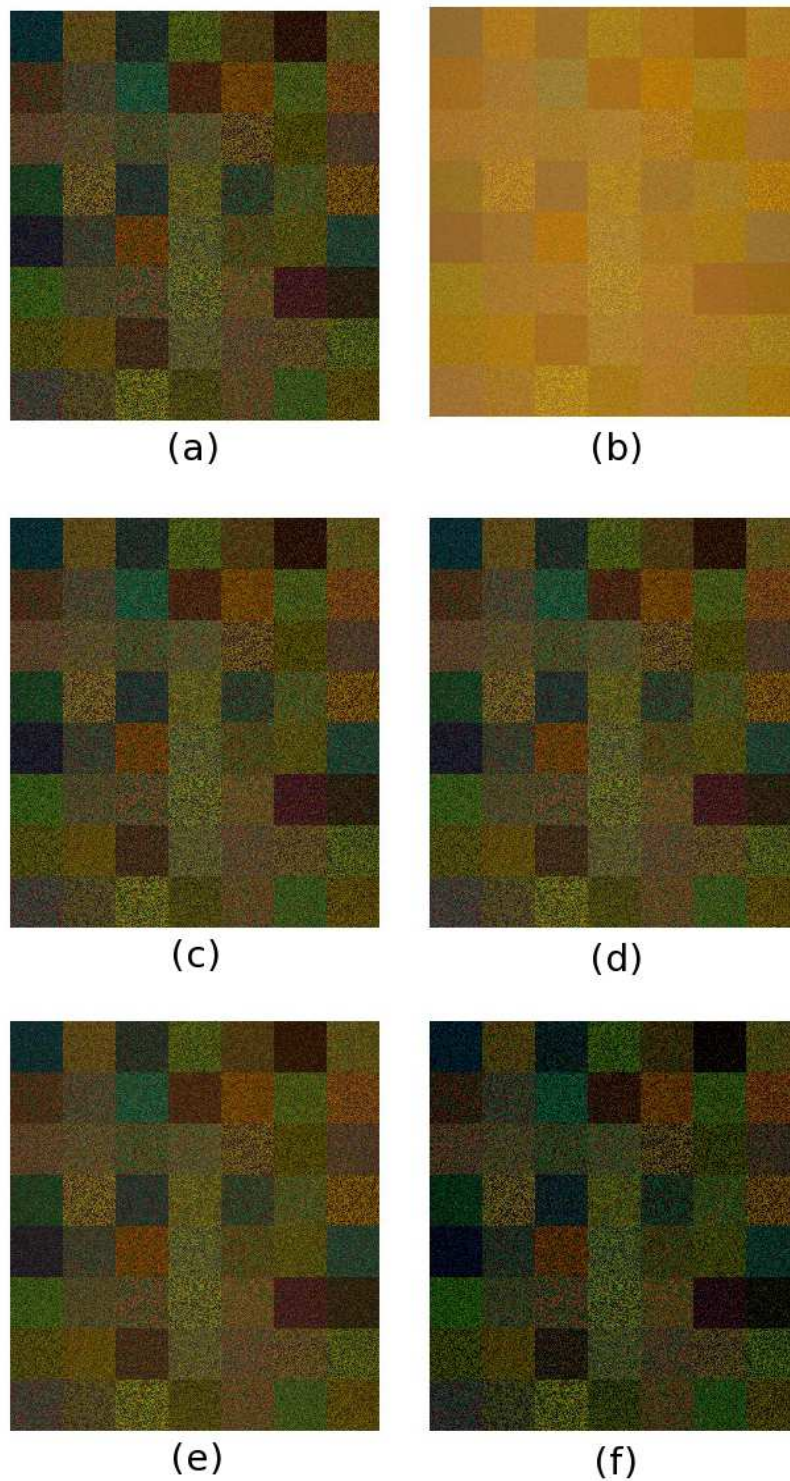


Figure 7.13: A sample of synthetic image converted to sRGB in a) clear water, b) turbid water, and improved images in c) Set I, d) Set II, e) Set III, f) Set IV.

Chapter 8

Experimental Results

8.1 Introduction

In this chapter the performance of the proposed algorithm is tested with real constrained and non-constrained images. The performance evaluations are defined by equations (7.10) - (7.13) in the simulation section in Chapter 7.

This chapter is structured as follows. Section 8.2 presents the results of processing monochrome constrained test images. Each monochrome image is of a narrow spectral band of bandwidth 10 nm. The estimation of the back-scatter parameter (γ) at different levels of water turbidity is investigated. The accuracy in estimating optical back-scatter for monochrome images with narrow spectral bands is evaluated. Some examples of improved monochrome images are presented. The consistency of the estimated back-scatter parameter (γ) across a series of continuous images is investigated at different wavelengths. The quality of the output image, when the image processed by the proposed algorithm, is compared with the output image, when the image is processed by the known contrast enhancement method, local histogram equalisation. Section 8.3 presents the results of processing constrained colour images in both narrow and wide spectral bands. The amount of colour difference introduced due to the proposed algorithm is evaluated for colour images with wide spectral bands. Some examples of improved images are presented. In Section 8.4, the algorithm is used to process non-constrained images. The consistency of γ is investigated in different colour channels. Samples of improved images with the corresponding degraded images are presented.

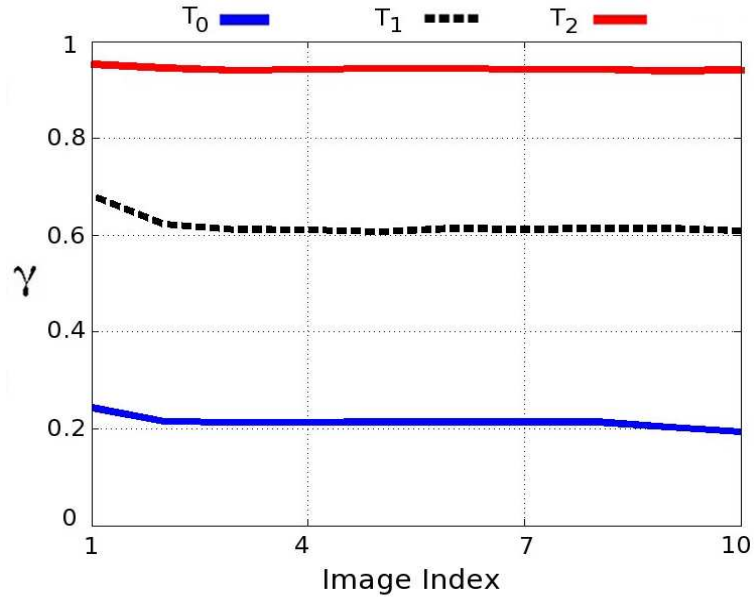


Figure 8.1: The plot of γ versus image index, for three water turbidity levels, T_0 , T_1 and T_2 .

8.2 Monochrome Images

In this section, the accuracy of optical back-scatter estimation and the consistency of the back-scatter parameter (γ) are investigated for monochrome images.

8.2.1 Accuracy

In this part, it is shown that the proposed BS-CostFunc filter can accurately detect the level of optical back-scatter. There is always some level of optical back-scatter even for images in clear water condition. Therefore, it is expected that when the proposed algorithm is applied to a clear underwater image, it detects this low level of optical back-scatter. Also, when the level of water turbidity is higher, a higher level of back-scatter is expected.

Optical back-scatter is estimated for 10 degraded images in clear (T_0), medium (T_1) and high (T_2) levels of water turbidity. The parameters are set to $\sigma_{cf} = 4$ and $\sigma_B = 180$. The estimated γ is plotted for 10 images and is presented in Figure 8.1. It can be seen from the plot that the value of estimated γ is different for each level and is associated with the level of water turbidity.

The estimated value of optical back-scatter, b_λ , is used to calculate the parameter,

a_λ . The estimated values of b_λ and a_λ are used to improve the images in series of T_0 , T_1 and T_2 . The improved images are found by subtracting b_λ from the degraded image and then scaling the remainder by $\frac{1}{a_\lambda}$.

A selection of improved images is presented in Figure 8.2. It can be seen that the improved images from T_0 and T_1 (Figures 8.2(a) and (b) at column (ii)) are similar. The improved images show the scene content without any scattering effect. This confirms that the algorithm can detect the level of optical back-scatter and correct the image appropriately. The lower part of the improved image from T_1 looks darker. This is because, a shadow appears in images from series T_1 (due to a reflection from the translation stage during capturing images in series T_1).

Although the effect of optical back-scatter is mitigated in the processed image from T_2 (Figure 8.2(c)), yet the quality of the processed image is lower with respect to the quality of the improved images from T_0 and T_1 . Resolution loss is evident in the processed image. The turbidity level in T_2 is in the high range of water turbidity (0.7 gr/100 litres) such that the image has both contrast loss and resolution loss problems. It is shown in Chapter 3, that for water turbidity more than 0.3 gr/100 litres both contrast loss and resolution loss are evident. Therefore, the images in T_2 can not be further improved by the proposed method.

Next, optical back-scatter is estimated for 10 monochrome images at different visible wavelengths, 400 nm - 720 nm, with parameters set to $\sigma_{cf} = 4$ and $\sigma_B = 180$. The value of \mathcal{E}'_{ave} (Equation (7.14)) for 10 test images at each spectral band is calculated. Note, the real value of optical back-scatter, b , is required for calculating \mathcal{E}'_{ave} . The regression method is used to calculate the value of b at different wavelengths, using the degraded image and the improved clear image as the reference.

Figure 8.3(a) presents the plot of \mathcal{E}'_{ave} versus wavelength. It can be seen for short wavelengths, $\lambda < 470nm$, the estimation error is negative, which means that the estimation value is over estimated, whereas for longer wavelengths, $\lambda > 470nm$, the estimation error is positive, which means it is under estimated. This is because, the level of noise in each monochrome image changes at different wavelengths. In simulations, it is shown in the plot of Figure 7.5(c) that when the level of noise varies, the estimation error changes. The value of estimation error is in accordance with the results from simulations.

Figure 8.4 presents a sample of the improved images together with the corresponding images in clear water (T_0), the improved of clear water, and the turbid water conditions (T_1) at different wavelengths (550 nm and 700 nm). It can be seen that the

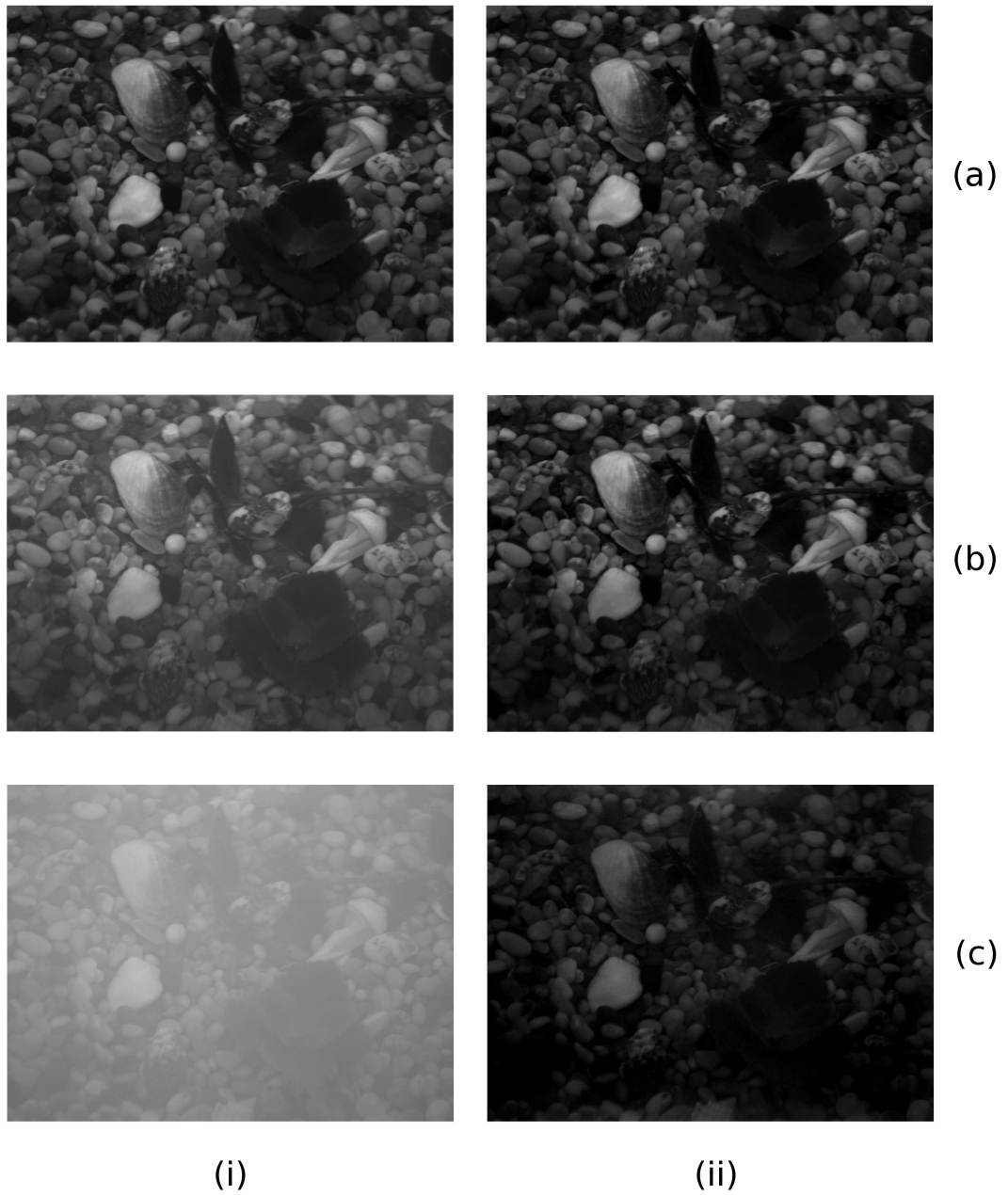


Figure 8.2: The selection of i) original images, and ii) improved images at 600 nm for different levels of water turbidity, a) T_0 , b) T_1 and c) T_2 .

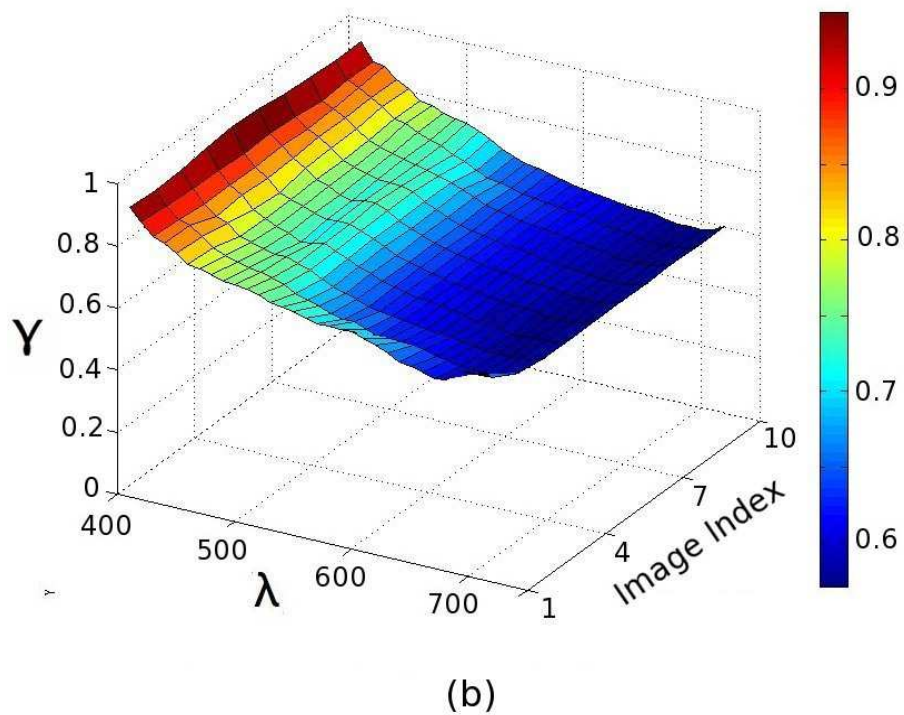
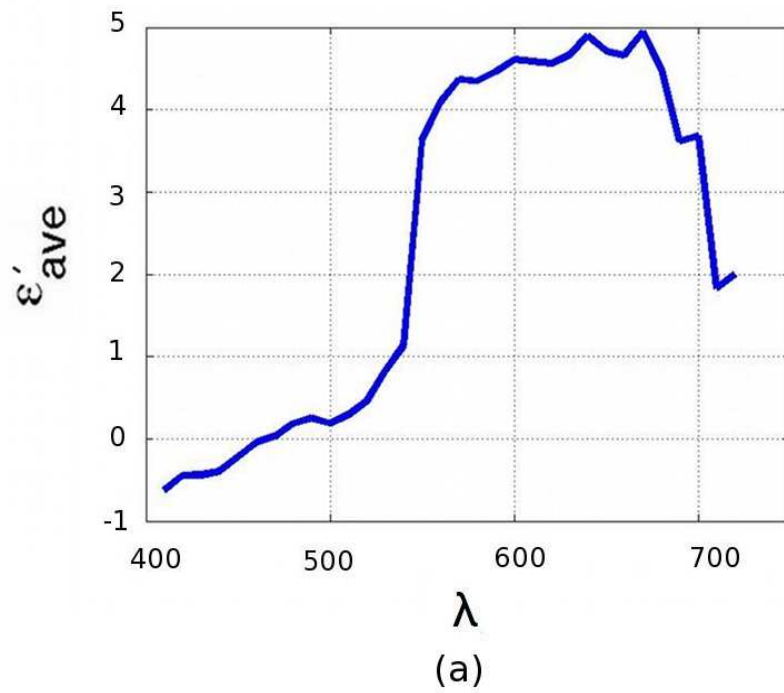


Figure 8.3: a) The plot of ϵ'_{ave} versus wavelength (λ). b) The surf plot of γ versus image index at different spectral bands.

proposed method significantly enhances the contrast of the degraded monochrome image.

8.2.2 Consistency

For a series of continuous images, when the level of water turbidity, the optical depth, the illumination and the wavelength remain unchanged, it is expected that the value of optical back-scatter remains unchanged over continuous images.

The position of the light source and the water turbidity are kept constant during the capture of 10 test images in series T_1 . As a result, the level of optical back-scatter at each narrow spectral band is expected to be consistent over the 10 test images. This is investigated experimentally. Since the position of light source is consistent, the shape of \bar{I} is similar for all of the images. Hence, to have a constant level of optical back-scatter, the value of estimated γ should be consistent over continuous images.

The value of estimated γ from the previous experiment (Section 8.2.1) is plotted versus image index at each wavelength and presented in Figure 8.3(b). It can be seen that the value of γ is consistent within 10 test images at each spectral band. However, the estimated γ at image 1 is slightly higher ($< 10\%$ difference with respect to the γ value at image 2 - image 10). This can be because when image 1 was captured the EP particles have not been settled properly in water tank, where as at the time of imaging for image 2 and after, the particles were settled and provided a constant level of optical scattering.

8.2.3 Quality

In this section the quality of the enhanced image by the proposed algorithm and also local histogram equalisation are compared visually. Figure 8.5(ii), (iii) present the selection of processed images by the proposed method using BS-CostFunc filter and by local histogram equalisation with 120 kernel size respectively for different levels of turbid water, T_0 , b) T_1 , c) T_2 . It can be seen that the quality of the enhanced images with the proposed method is superior to the local histogram equalisation method. The processed images with local histogram equalisation have noise and look grainy.

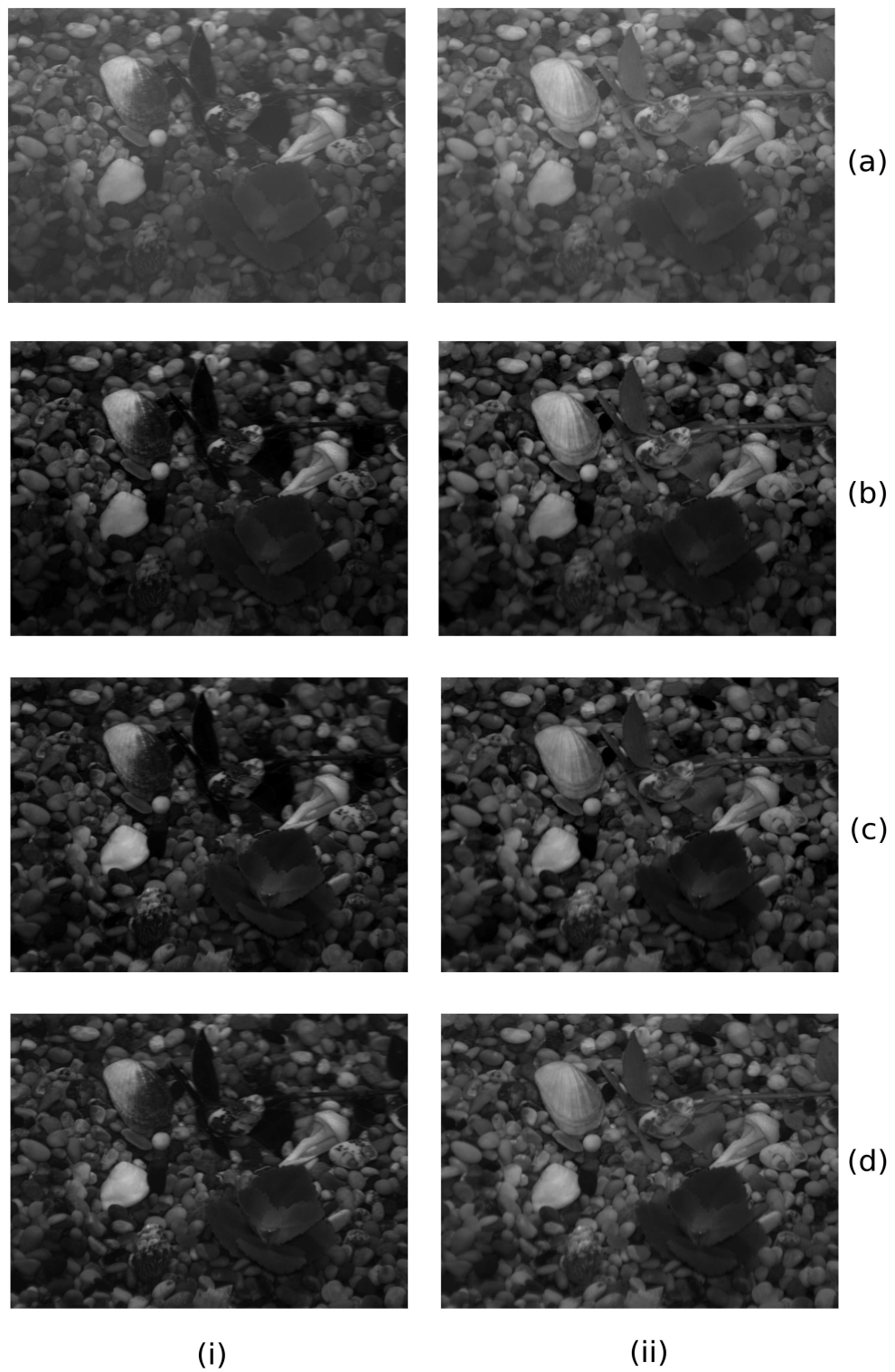


Figure 8.4: The selection of images in a) turbid water (T_1), b) improved from T_1 , c) improved from T_0 , d) clear water (T_0) at i) 550 nm, ii) 700 nm.

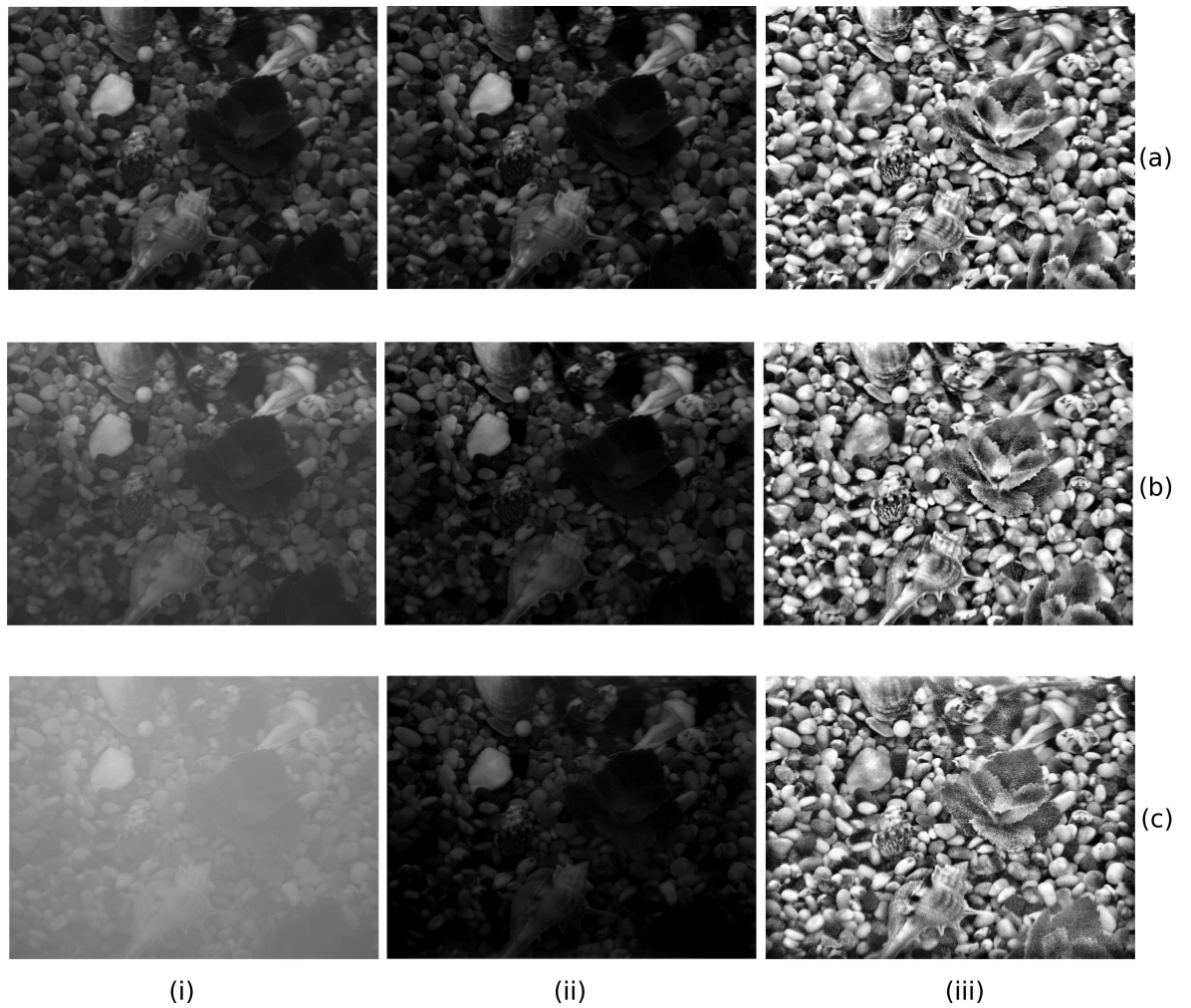


Figure 8.5: The selection of images in i) original images, ii) processed with the proposed method using BS-CostFunc filter, iii) processed with local histogram equalisation with 120 kernel size, for different levels of turbid water a) T_0 , b) T_1 , c) T_2 .

8.3 Colour Constrained Images

In this section, the results of experiments with colour images are presented. The colour fidelity of the improved images using the proposed algorithm is investigated experimentally for real constrained colour images. Experiments are done on colour images with both narrow and wide spectral bands. 10 test images from T_0 and T_1 for clear and turbid water respectively are used for these experiments. The processed image in clear water condition is used as the reference image. The first experiments uses images with 10 nm bandwidth.

8.3.1 Experiment 1- Colour Images in Narrow Spectral Bands

The degraded colour image from T_1 is improved by compensating the effect of optical back-scatter in each spectral band. The parameters are set to $\sigma_{cf} = 4$ and $\sigma_B = 180$.

For each colour image, the value of b_λ is estimated for the monochrome image (I_λ) of that specific band with central wavelength, λ . Then the value of a_λ is calculated using Equation (6.19). Each monochrome image is improved by subtracting b_λ from I_λ and then rescaling the remaining by $\frac{1}{a_\lambda}$.

The multispectral degraded images (T_1), the improved images from T_1 , the reference images (improved from T_0), and the clear water images (T_0) are mapped to XYZ colour space, and then converted to sRGB to be visually presented. Figures 8.6(a) - (d) show a selection of colour degraded images from T_1 , the improved image from T_1 , the reference image (improved from T_0), and the image from T_0 respectively for two different scenes (image 1 and image 10).

It can be seen that the low level of optical back-scatter is removed from the image in clear water condition. The colour of the improved images from the turbid water (Figure 8.6(b)) is similar to that of the reference images (Figure 8.6(c)). This result is in accordance with the simulation results in Section 7.3.4.

8.3.2 Experiment 2- Colour Images in Wide Spectral Bands

In the second experiment, the performance of the proposed algorithm, when improving colour images in wide spectral bands is investigated. There are two main sources of estimation error, when processing in wide spectral bands with respect to processing in narrow spectral bands, which are the extra estimation error introduced by BS-CostFunc filter for wide spectral bands, and the difference of the level of noise between wide

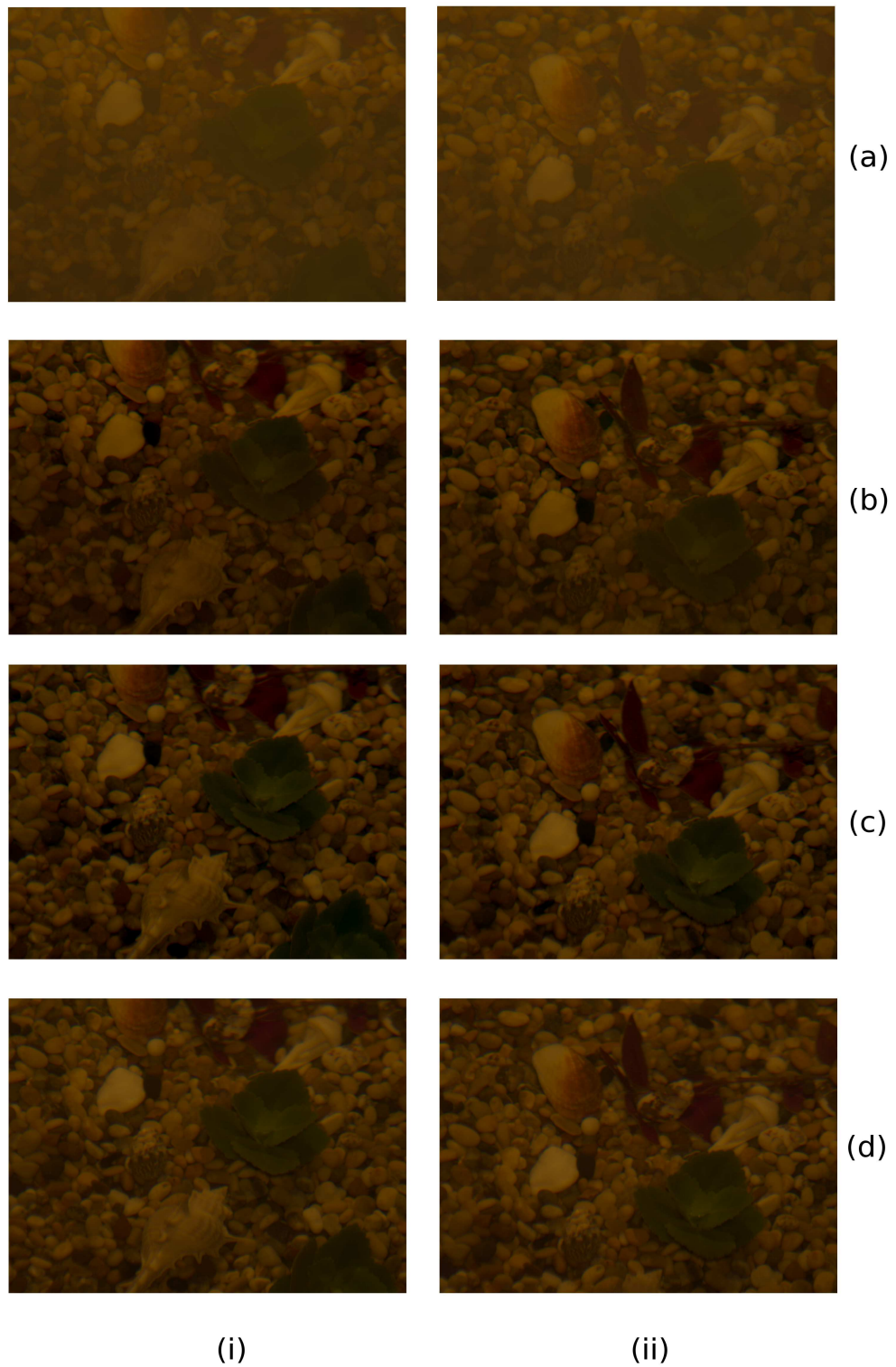


Figure 8.6: The selection of colour images from two different scenes, i) image 1, ii) image 10 for a) the degraded image from T_1 , b) the improved image with narrow spectral bands from T_1 , c) the reference image (improved with narrow spectral bands from T_0), d) the image from the clear water condition (T_0).

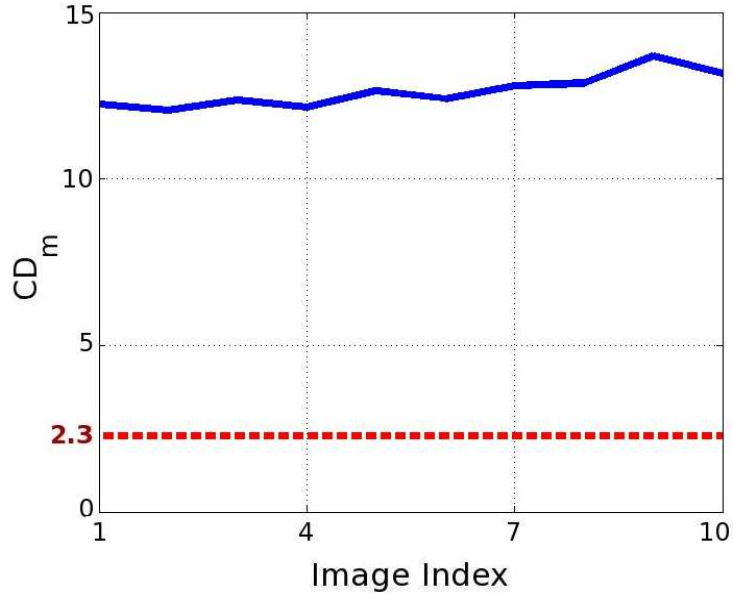


Figure 8.7: The plot of colour difference between the improved colour image in wide bands from T_1 and the reference image (the improved from T_0) for 10 images.

bands and narrow bands.

In simulations, the plot of \mathcal{E}'_{ave} versus σ_n in Figure 7.5(c), shows that when the level of noise is low, the estimation error is higher and is overestimated. For medium level of noise, the estimation error decreases to lower value. The level of noise in wide spectral bands is lower, with respect to the narrow spectral bands, because during the mapping process, the noise value is nearly averaged over the narrow bands of that specific wide band. Therefore, it is expected that the level of estimation error should be higher and also should be overestimated for wide spectral bands. The subtraction of a higher value from the degraded image pixels, causes the pixel intensity of the improved image have lower values and as a result the image are expected to look darker. The improved synthetic image in wide spectral band, presented in Figure 7.13(f), also shows that the processed image in wide spectral bands is darker with respect to the processed image in narrow spectral bands (Figure 7.13(e)).

The multispectral images are first mapped to XYZ and then converted to sRGB colour space. The degraded images are improved by processing in each colour channel, red (R), green (G) and blue (B). The parameters are set to $\sigma_{cf} = 6$ and $\sigma_B = 180$. The process of improving images in each colour channel is as explained for narrow spectral bands in Experiment 1.

Figures 8.8(a) - (d) present a selection of images from the degraded image T_1 , the improved image in narrow spectral bands, the improved image in wide spectral bands, and the reference image (the processed images from clear water condition in narrow bands) respectively for image 1 and image 10. It can be seen that the improved image in wide bands are darker than that of the narrow bands, while the colour is the same for both images.

The numerical colour difference is found between the improved image from T_1 in wide spectral bands and the reference image (the improved from T_0), which are converted to $L^*a^*b^*$ colour space.

The mean colour difference, CD_m , (Equation (7.20)) is calculated for 10 test colour images. Figure 8.7 presents the plot of the mean colour difference, CD_m , versus image index for 10 colour images. The plot shows that the CD_m value is higher than the eye sensitivity threshold (JND=2.3). This colour difference can be because of the difference in intensity level between two images, as the calculation of colour difference considers the lightness difference as well.

8.4 Colour Non-constrained Images

In this section, the proposed algorithm is tested with non-constrained colour images, which are captured in real underwater condition. The images are captured at two different locations, in UK and Abu Dhabi as explained in Section 3.1. Since the reference image in clear water condition is not available for non-constrained images, as a result the accuracy of the optical back-scatter estimation can not be assessed directly. Therefore, the evaluation of the proposed algorithm is done by investigating the consistency of the estimated γ value in each spectral band. The parameters are set to $\sigma_{cf} = 3$, $\sigma_B = 90$ and $\sigma_{cf} = 3$, $\sigma_B = 80$ for processing images from the Thales Research and the ADMA company respectively.

The value of γ is estimated for each colour channel (R, G, B) for 100 continuous test images at two different water locations. Figures 8.9(a) and (b) present the plots of γ versus image index for each colour channel for images from the ADMA and the Thales Research companies respectively. From Figure 8.9(a) (ADMA), it can be seen that the level of optical back-scatter changes from image 1 to image 100. The plots of γ versus image index for different channels show that the red channel has higher fluctuations with respect to the green and the blue channels. Yet, the trend of increasing γ with image index in red channel is consistent with the trends in the green and blue channels.

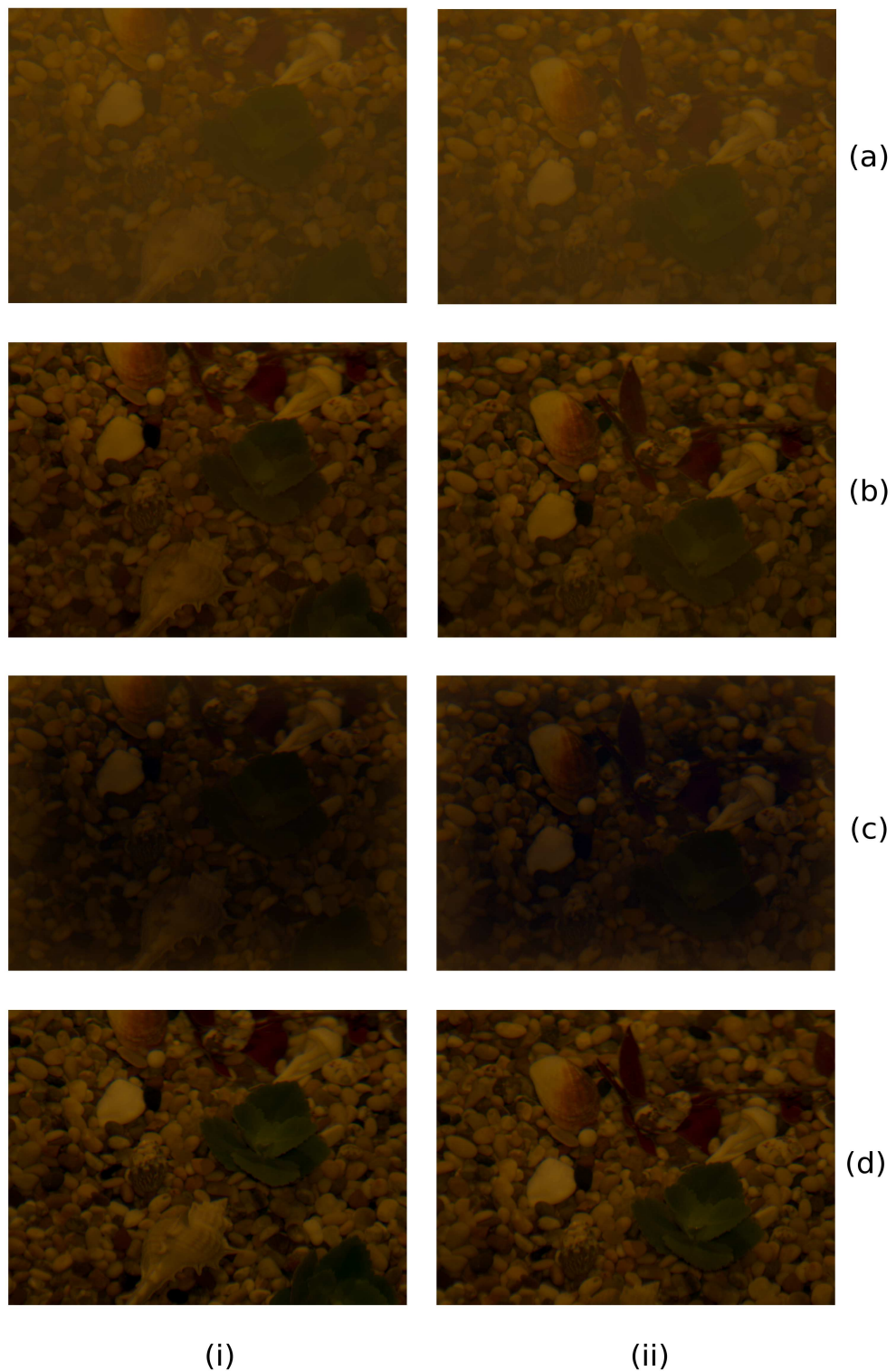


Figure 8.8: The selection of colour images from two different scenes, i) image 1, ii) image 10 for a) the degraded image from T_1 , b) the improved image in narrow spectral bands from T_1 , c) the improved image in wide spectral bands from T_1 d) the reference image (improved with narrow spectral bands from T_0).

From Figure 8.9(b) (Thales Research), it can be seen that the level of optical back-scatter also from image 1 varies to image 100. The plots of γ versus image index for all colour channels show similar levels of fluctuations.

Sample of degraded images are also enhanced by Photoshop, one of the popular commercial image enhancement programme. The histogram of the degraded image is first shifted in such a way that to keep 2% of the image histogram less than zero, in non-visible part, in order to compensate the effect of camera noise. Then the contrast enhancement option is applied to images. Figures 8.10, 8.11 present the sample of the degraded, the improved images by the proposed algorithm using BS-CostFunc filter and the improved images by Photoshop from the ADMA and the Thales Research companies respectively. It can be seen that the processed images by the proposed algorithm are significantly improved in terms of perceived visibility and more detail is visible. The processed images by Photoshop have limited contrast improvement, and the images are still low contrast.

The sample of 24 continuous image pairs, the degraded and improved images by the proposed method, are presented in Figures 8.12 - 8.15 from one second of the ADMA and the Thales Research companies video frames. Figures 8.12, 8.13 presents images 1 to 12 and 13 to 24 of the ADMA company. Figures 8.14, 8.15 presents images 1 to 12 and 13 to 24 of the Thales Research company. It can be seen that the improvement process is consistent over continuous images, and the quality of the improved images remains consistent for both samples from the ADMA and the Thales Research companies.

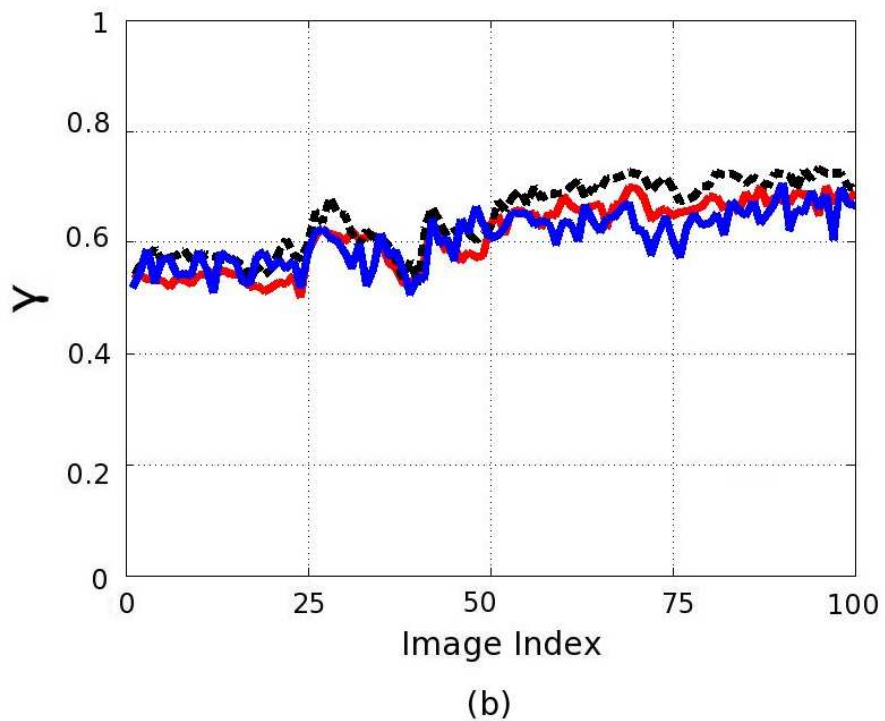
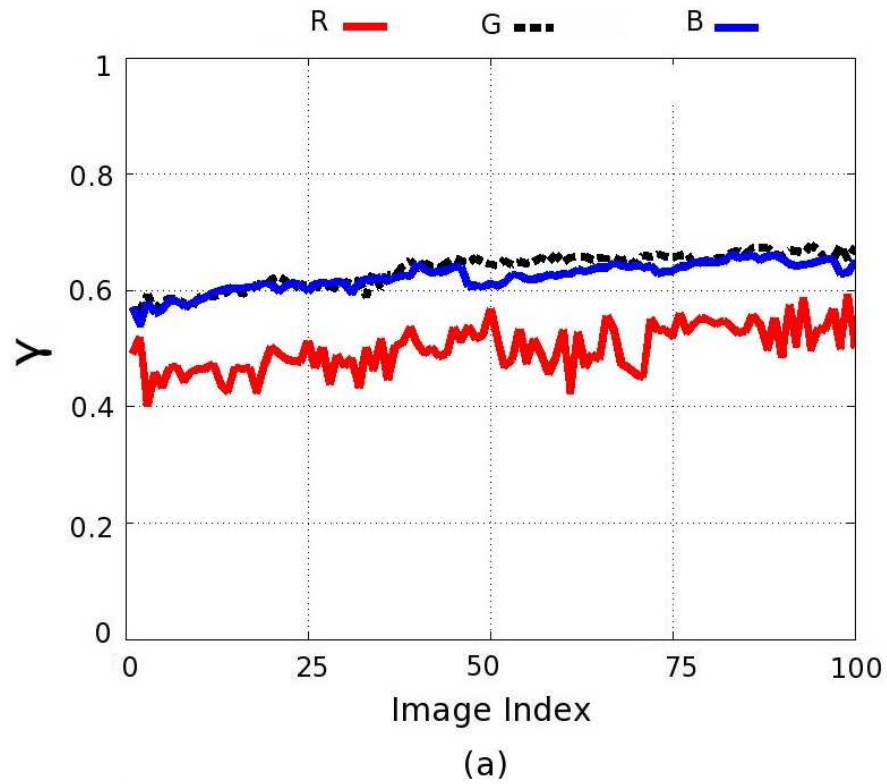


Figure 8.9: The plot of γ versus image index for 100 images provided by a) the ADMA company, b) the Thales Research company

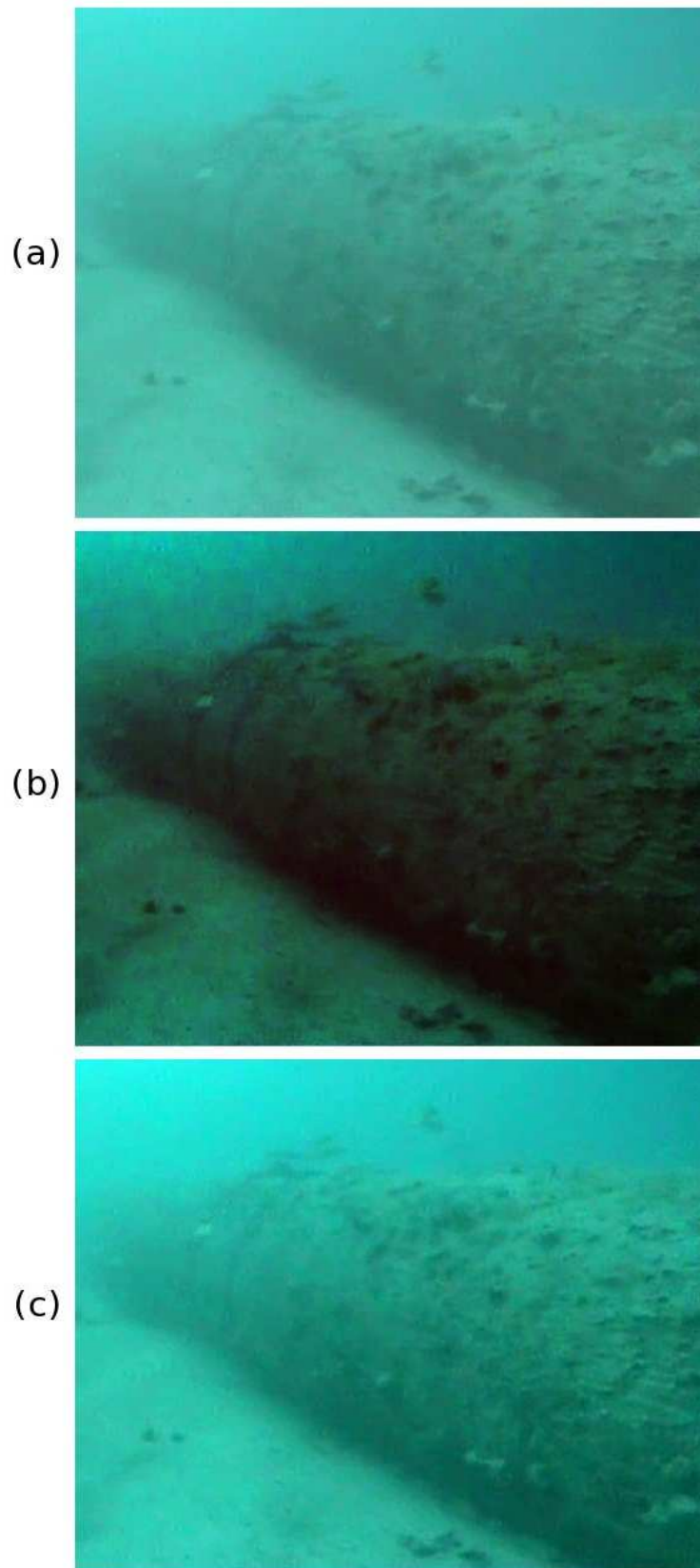


Figure 8.10: The sample of images from the ADMA oil company a) Original degraded image, b) Improved image by the proposed algorithm with BS-CostFunc filter, c) Improved image by Photoshop. First, 2% of the image histogram is shifted to be less than zero to compensate for the noise effects. Then, the image contrast is enhanced.

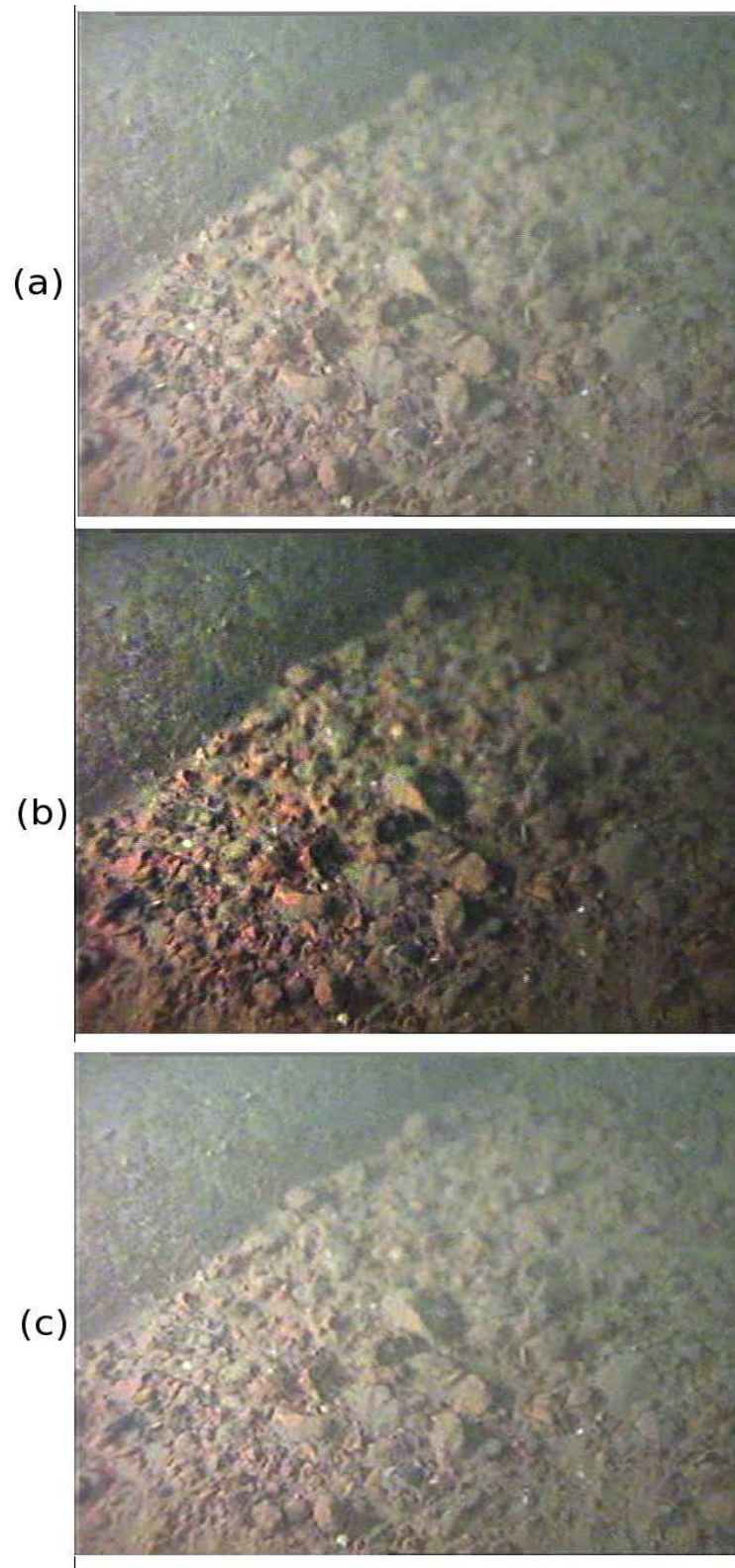


Figure 8.11: The sample of images from the Thales Research company a) Original degraded image, b) Improved image by the proposed algorithm, c) Improved image by Photoshop. First, 2% of the image histogram is shifted to be less than zero to compensate for the noise effects. Then, the image contrast is enhanced.

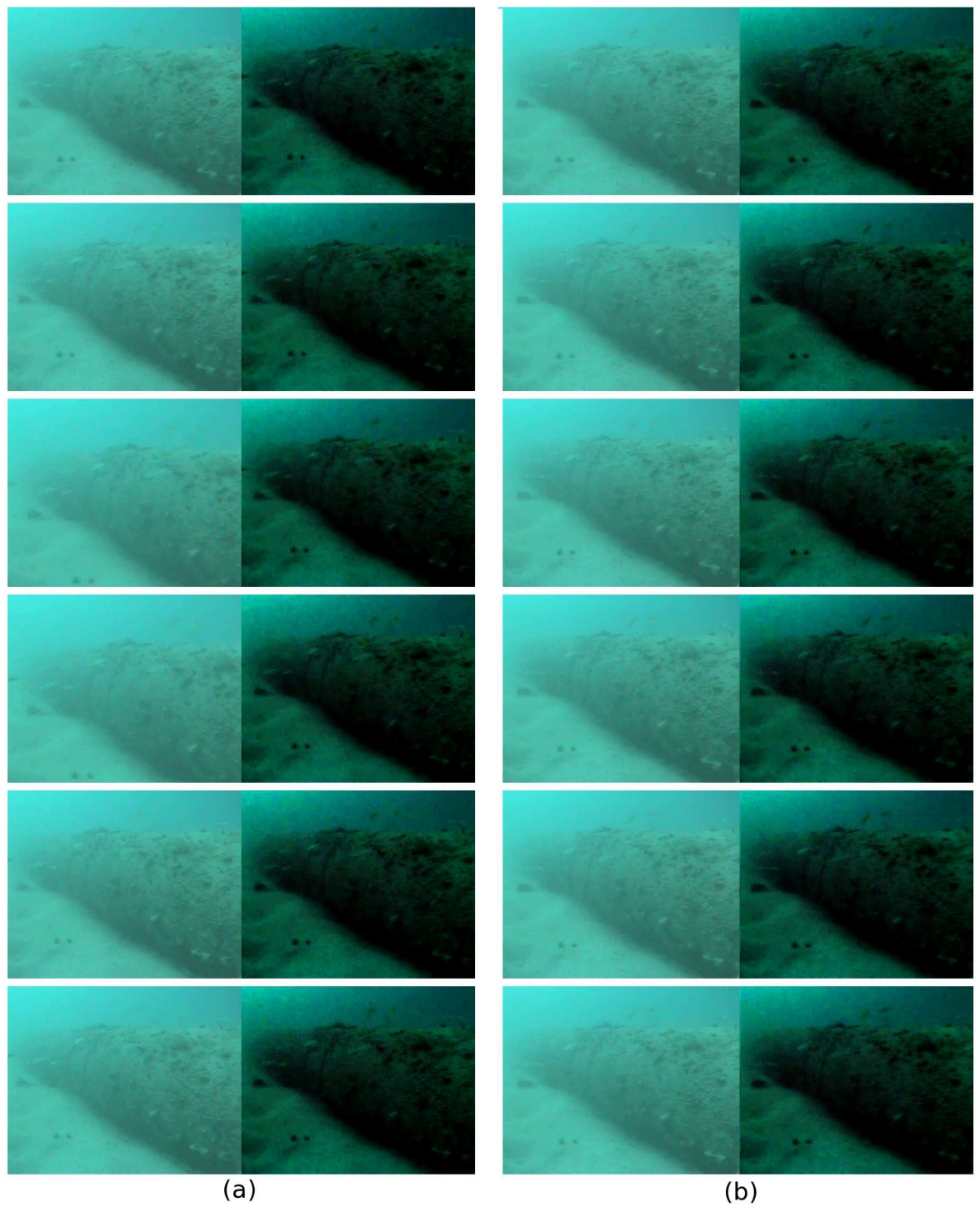


Figure 8.12: The sample of continuous images from the ADMA oil company video sequence. a) Image 1-6, b) Image 7-12.

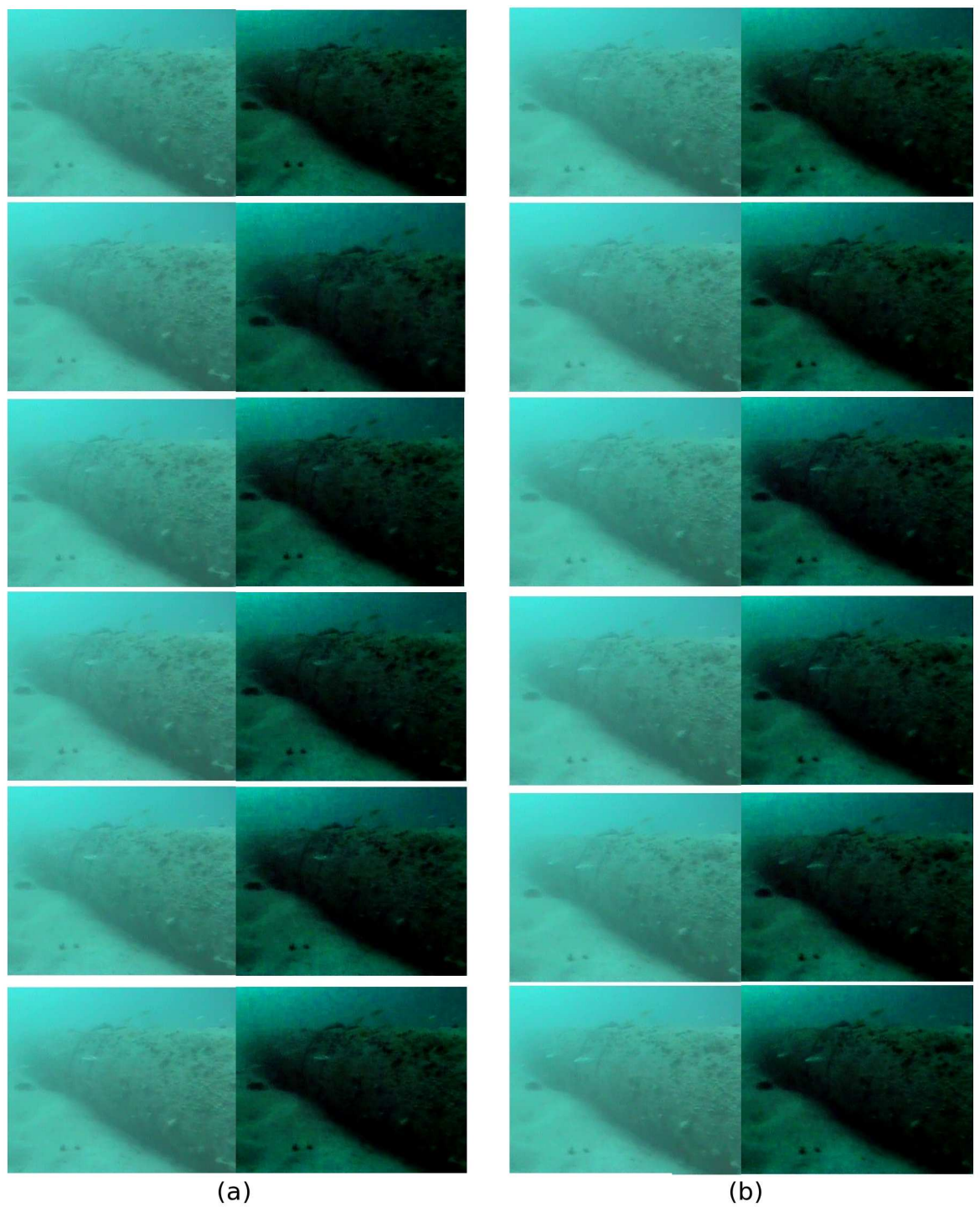


Figure 8.13: The sample of continuous images from the ADMA oil company video sequence. a) Image 13-18, b) Image 19-24.

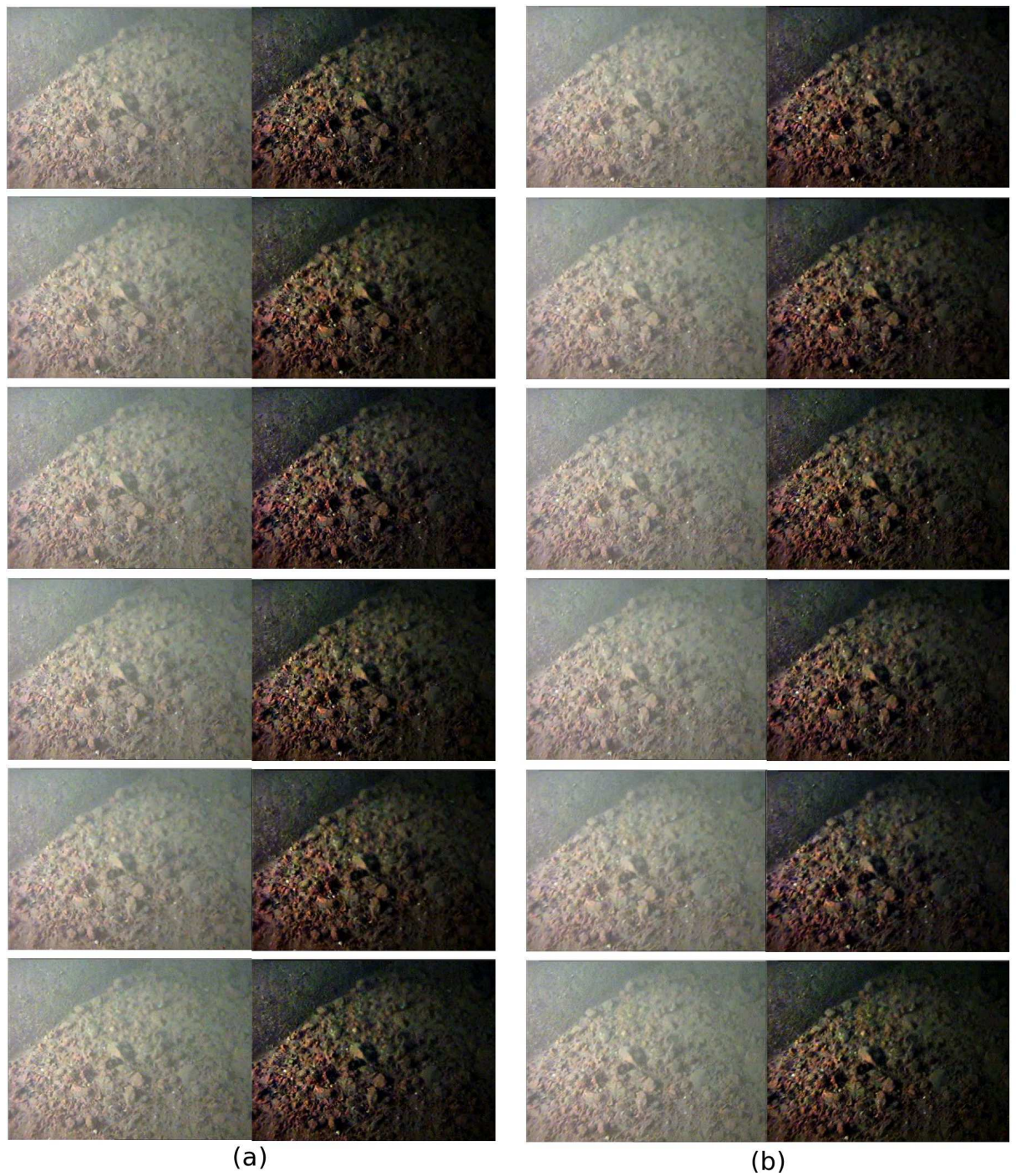


Figure 8.14: The sample of continuous images from the Thales Research company video sequence. a) Image 1-6, b) Image 7-12.

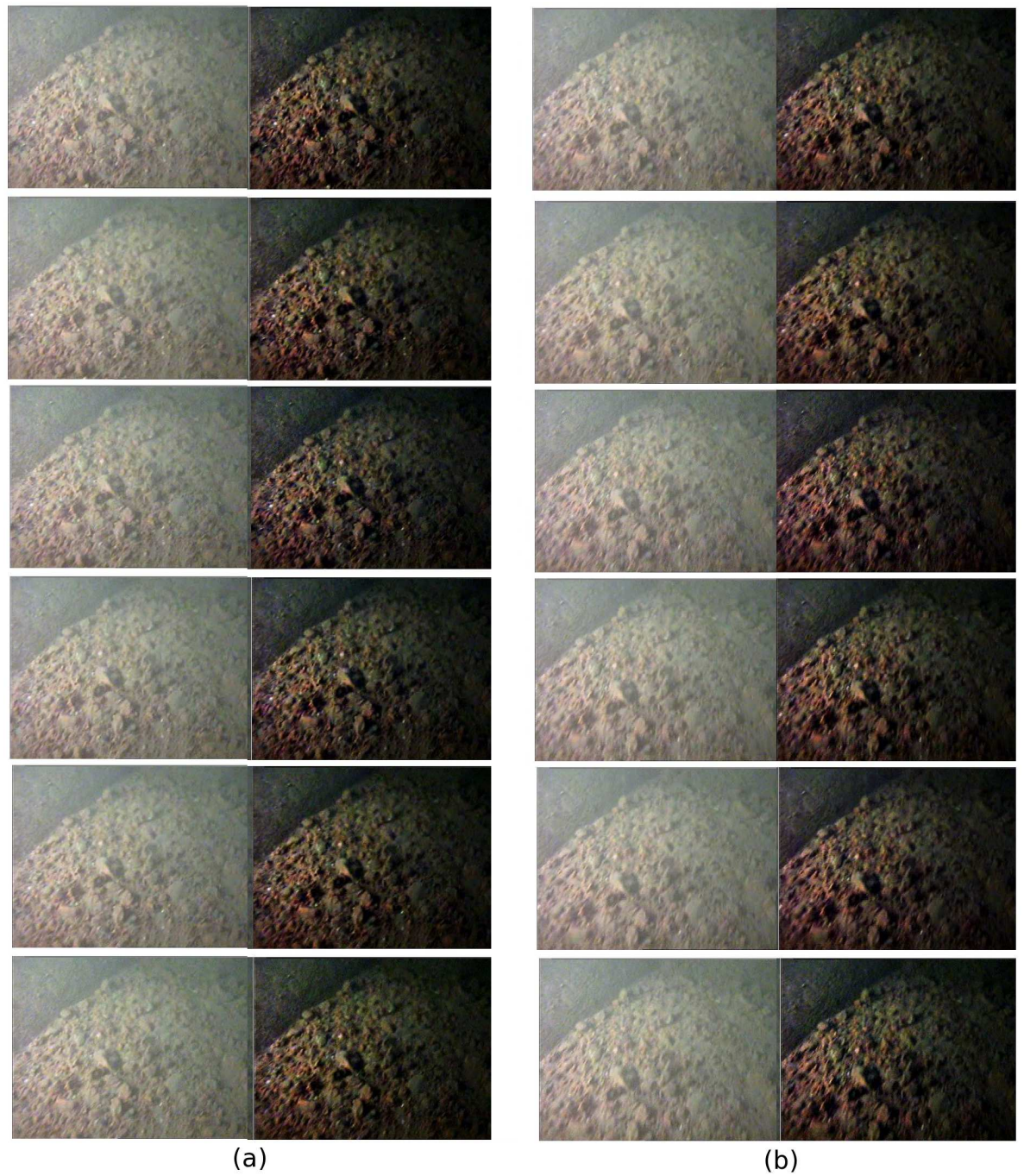


Figure 8.15: The sample of continuous images from the Thales Research company video sequence. a) Image 13-18, b) Image 19-24.

Chapter 9

Conclusions and Future Works

The aim of this thesis is to improve the quality of an underwater image. Conclusions from the results of this work and the suggestions for future work are discussed below.

9.1 Conclusions

Resolution loss and contrast loss are two of main types of degradation in underwater images. There are due to the effects of small angle forward-scattered light and back-scattered light respectively. Although both of these problems degrade the image quality, the problem of contrast loss is less difficult to mitigate than that of resolution loss. The magnitudes of these two problems vary according to distance and water turbidity. Figure 9.1 presents a chart describing the effects of distance and turbidity from the experimental results of Chapter 4. The two parameters represent a two dimensional space which is divided by the dotted line at $\beta = 0.059m^{-1}$. Above the dotted line, the region A1 corresponds to parameter values for which both resolution loss and contrast loss are significant. Below the dotted line, the regions A2 & A3 correspond to parameter values for which only contrast loss is significant. The image contrast in the region A2 is higher than 5%, whereas the image contrast in the region A3 is very low, less than 5%. As the image contrast in the region A3 is very low, practically the image contrast enhancement is not useful for improving the images. In practice, contrast enhancement can be used to improve the images within the region A2. It can be concluded that in certain imaging situations the image can be improved by compensating the effect of contrast loss.

In this work, an image processing method is proposed to improve the image quality. The proposed method is applicable to underwater images, which are taken in water

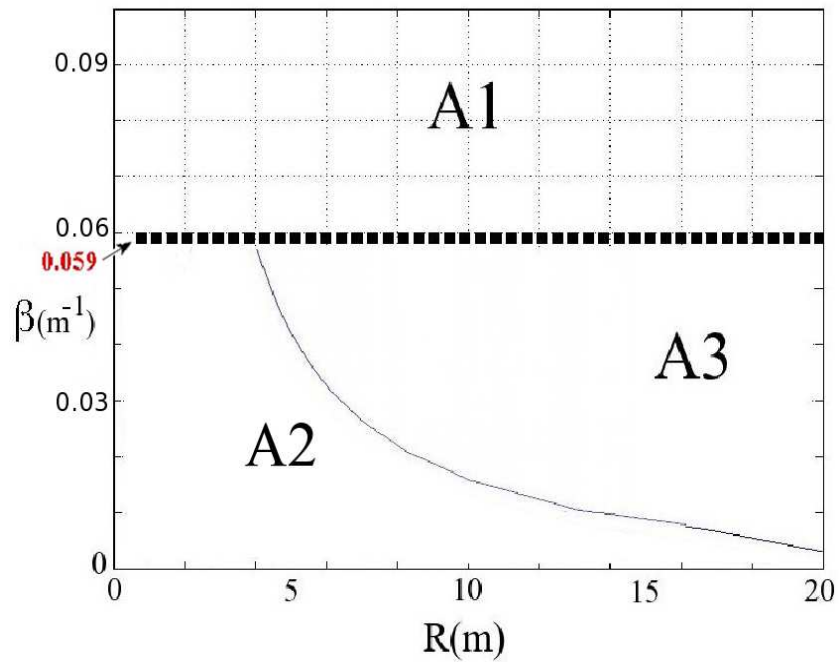


Figure 9.1: The chart is describing the effects of distance (R) and turbidity (β). The region A1 corresponds to parameter values for which both resolution loss and contrast loss are significant. The regions A2 corresponds to parameter values for which only contrast loss is significant and the image contrast is $> 5\%$ (Image enhancement is applicable). The region A3 corresponds to parameter values for which only contrast loss is significant, but the image contrast is very low $< 5\%$.

conditions with parameters in the region A2. The basis of the proposed enhancement method is to remove the effect of optical back-scatter from the degraded images, since optical back-scatter is the main cause of contrast loss.

A forward model for a degraded underwater image is given by Equation (5.12). In this model, the relation between the pixel values of a degraded image in turbid water with the corresponding value in clear water condition is a straight line. The underwater image model is validated experimentally for different water conditions, such as different levels of water turbidity and different light wavelengths. The inverse of underwater image model, suggests that the contrast of the degraded image can be improved by subtracting the intensity value of optical back-scatter from the degraded image in each pixel position, and rescaling the remaining using the extinction parameter. Thus, the inverse model is the basis of the proposed enhancement method.

In this work, three different filters are used to estimate the level of optical back-scatter in a degraded image. Two of the methods, BS-Hist and BS-CostFunc filters, use the model of optical back-scatter given by Equation (6.11). The performance of these filters are examined and compared using Monte-Carlo simulations with synthetic underwater images in clear and turbid water under different statistical assumptions and filter parameters. The results of the simulations with monochrome images indicate that the performance of the BS-CostFunc filter is superior to that of the BS-MinPix and BS-Hist filters. Therefore, the BS-CostFunc filter is selected to estimate the level of optical back-scatter.

The accuracy of optical back-scatter estimation in monochrome images is examined by simulations with synthetic underwater images. The simulation results showed that the maximum total estimation error for estimating optical back-scatter is less than 5%. The errors are the γ estimation error, which is around 1% (maximum 5 intensity level) and the estimation error of finding the optical back-scatter spatial variation (\bar{I}_λ), which is around 3%. In addition, it is shown that when the level of light source intensity is lower, the level of optical back-scatter is lower, and as a consequence the estimation error is lower.

From experimental results with real monochrome underwater images, it is concluded that

- there is no perfectly clear reference for underwater images. Even for clear water conditions, there is some level of optical back-scatter.
- the amount of correction in the proposed method depends on the level of degradation. It is shown that for clear water, the correction is very low, whereas for

high level of degradation, the correction is high.

- the method does not require any information about the physical properties of the scene, and also does not require any special equipment for image acquisition. It only requires an image intensity, which can be obtained by any commercial digital camera. Therefore, this method is generally applicable.
- the proposed method can significantly improve the contrast of a degraded monochrome underwater image without introducing either further noise or over enhancement.
- the level of estimated optical back-scatter is consistent for continuous images with same level of optical back-scatter. It is shown in non-constrained images, that even when the level of optical back-scatter over continuous images is not constant, the estimated level of optical back-scatter varied over the continuous images. This indicates that the method is applicable to video streams as well as one image.
- the computational cost of the proposed method is mainly due to the Oakley-Bu cost function to estimate the parameter γ and the smoothing filter to find the spatial variation of the light intensity. In previous study, it is shown the computational cost of Oakley-Bu cost function is low. Also, the recursive Gaussian filter is used as the smoothing filter and this is fast. So, it can be concluded that the computational cost of the proposed method is low. Therefore, the proposed method is applicable to real time imaging applications.

It is shown mathematically and confirmed by simulations with synthetic colour images that when the accurate level of optical back-scatter is known, it is possible to recover colour of a degraded underwater image, either in form of multispectral or RGB. This result suggests that underwater image improvement for colour images is possible with colour fidelity.

The result of improving multispectral images, synthetic and real images, by the proposed method indicates that the colour difference between the recovered image and the reference image is below the eye sensitivity threshold, which is $JND=2.3$. From this result, it can be concluded that it is possible to recover the spectrum of a degraded multispectral underwater image.

Comparing the improved images in RGB and multispectral images with reference images, it can be seen both images are darker. For multispectral it is hardly noticeable, whereas for RGB images it is evident. It is shown mathematically that the performance

of BS-CostFunc filter for RGB images, introduces noticeable estimation error. Thus, the amount of darkness is related to the amount of estimation error. The result of simulation shows that the amount of estimation error varies by the level of image noise. As the level of noise increases the error decreases. Multispectral images have higher level of noise with respect to RGB images, which causes having lower error. As a result, it can be concluded that the amount of darkness depends on the level of image noise.

9.2 Suggestions for Future Work

The suggestions for possible future works are:

- The algorithm of the proposed method is written in MATLAB. The algorithm should be written in another programming language, such as C, in order that the algorithm can be used commercially. For example, the system could be an extra option for processing underwater images in digital cameras, or an enhancement option for image editing software.
- The method can be extended to recover spectral information for hyperspectral images, which also cover ultraviolet and infrared wavelengths.
- It is shown that the performance of BS-CostFunc filter in RGB images introduces noticeable estimation error. Further statistical study should be done to find out the expected value of the estimation error due to the performance of BS-CostFunc filter with RGB images, and also whether the estimation error is underestimated or overestimated. Moreover, by knowing the expected error in b_λ , the amount of error for scaling factor, a_λ , can also be investigated.
- The calculated colour difference (ΔE_{ab}) between the improved image and reference image is above the eye sensitivity threshold (JND) for RGB images. This suggests there is colour difference. However, the improved images are only darker and have similar colour with respect to reference image. This contradiction might be because the value of ΔE_{ab} includes the difference in lightness (L^*) as well as the difference in chroma (a^* , b^*). Further work should be done to compare only the chroma independent on the lightness, in both images with another colour measuring tool. A possible suggestion would be to plot the values

of b^* versus a^* in $L^*a^*b^*$ colour space for two reference and processed image pixels.

- Further work can be done to extend the algorithm in order that the effect of darkness is corrected in improved image. Possible suggestion is to apply histogram modification to place the image histogram in visible range.
- The method can be extended to real time image processing. However, processing images in real time is not straight forward. In real time application each image is improved independently. For a series of adjacent images, even a small difference in estimated value of γ can result the variation in the intensity or colour of the improved image pixels, which causes further noise in form of image flickering. The possible solution to correct the effect of flickering is to smooth the variation of γ value over adjacent images. For this, a time filter can be used after BS-CostFunc filter.

Appendix A

Camera Specifications

A.1 Canon PowerShot Pro90 IS

Max resolution	1856 × 1392
Lower resolutions	1024 × 768, 640 × 480
Image ratio w:h	4 : 3
CCD pixels	3.34 megapixels (2.6 effective)
CCD size	1/1.8" (0.556")
CCD colour filter array	C - Y - G - M
ISO rating	Auto (50-100), ISO 50, 100, 200, 400
Lens	Canon F2.8 - F3.5 Image Stabilised, 13 elements in 10 groups
Lens thread	58 mm
Zoom wide	37 mm
Zoom tele	370 mm (10 x)
Digital zoom	Yes, 2 x or 4 x
Auto Focus	Continuous AF (Silent focus mechanism)
Manual Focus	Yes (approx. 40 focus positions)
Normal focus range	Wide: 10 cm - Infinity
Tele:	1 m - Infinity
White balance override	Auto, Five presets, Custom white balance
Min shutter	8 sec (Shutter Priority or Manual)
Max shutter	for help 1/1000 sec
Flash	Internal, automatic pop-up
Flash range	(ISO 100) Wide: 70 cm - 4.2 m
Tele:	1 m - 3.4 m
External Flash	Yes, Hot-Shoe: Canon Speedlite 220EX, 380EX, 420EX and 550EX

Flash modes	Auto, Red-eye reduction auto, Red-eye reduction on, On and Off
Exposure modes	Auto, Creative (Program AE, Aperture Priority, Shutter Priority, Manual), Pan-Focus, Portrait, Landscape, Night scene, B&W, Stitch Assist, Movie
Metering	Center-weighted, Spot
Aperture priority	Wide: F2.8, F3.2, F3.5, F4.0, F4.5, F5.0, F5.6, F6.3, F7.1, F8.0 Tele: F3.5, F4.0, F4.5, F5.0, F5.6, F6.3, F7.1, F8.0
Shutter priority	Yes, 1/1000, 1/800, 1/640, 1/500, 1/400, 1/320, 1/250, 1/200, 1/160, 1/125, 1/100, 1/80, 1/60, 1/50, 1/40, 1/30, 1/25, 1/20, 1/15, 1/13, 1/10, 1/8, 1/6, 1/5, 1/4, 0.3, 0.4, 0.5, 0.6, 0.8, 1, 1.3, 1.6, 2, 2.5, 3.2, 4, 5, 6, 8
Full manual	Yes (any combination of above apertures & shutter speeds apart from 1/1000 sec only F4.0 - F8.0)
Noise reduction	All the time (always enabled)
AE Lock	Yes
Exposure adjustment	-2EV to +2EV in 1/3EV steps
Bracketing	Yes, 3 images @ 0.3, 0.7, 1.0, 1.3, 1.7 or 2.0 EV steps
Movie clips	320 x 240, 15 fps, 30 seconds, including audio
Audio clips	Yes, WAV file format
Tripod mount	Yes
Self-timer	Yes, 10s delay
Video out	Yes, switchable NTSC / PAL
Storage types	Compact Flash Type I & II
Storage included	16 MB Compact Flash Type I card
Uncompressed format	Yes, RAW (Canon proprietary)
Compressed format	JPEG (EXIF)
Quality Levels	RAW, JPEG: Super Fine, Fine, Normal
Viewfinder	TTL Electronic View Finder (with dioptre correction)
LCD	1.8" TFT Flip-out and tilt
Playback zoom	Yes, 2.5x to 5.0x
Operating system	Proprietary
TWAIN acquire	(Required for RAW format) PC Windows 95/98 (including SE) / Me / NT 4.0 (Service Pack 3 or higher) / 2000, Mac OS 8.1 or higher
Video Out	PAL / NTSC (selectable) - including audio
Connectivity	USB, RS232C (optional cable)
Battery	Yes, supplied Canon BP-511 Li-Ion rechargeable
Battery charger	Yes, supplied AC adapter / charger
Weight (exc. batteries)	680 g (1.5 lb)
Dimensions	125 x 85 x 130 mm, (4.9" x 3.3" x 5.1")

A.2 Hamamatsu ORCA-ER

Imaging device	Progressive scan interline CCD with micro-lens
Effective no. of pixels	1344(<i>H</i>) × 1024(<i>V</i>)
Cell size	6.45 <i>m</i> × 6.45 <i>m</i> (square format)
Effective area	8.67 <i>mm</i> × 6.60 <i>mm</i> (2/3-inch format)
Pixel clock rate	14.75MHz/pixel
Frame rate	8.3 Hz 2 × 2 <i>binning</i> 16.4 Hz 4 × 4 <i>binning</i> 29.0 Hz 8 × 8 <i>binning</i> 45.3 Hz
Readout noise (r.m.s.)	8 electrons
Full well capacity	18,000 electrons
Dynamic range*	2250 :1
Cooling method	Peltier cooling with hermetic vacuum sealing
Cooling temperature	- 20 C at 20 C ambient temperature
Dark current	0.1 electron/pixel/sec
A/D converter	12 bit
Output signal (digital output)	RS-422A 12-bit parallel output
External control	RS-232C (full remote for all camera functions)
Sub array**	yes
External trigger	yes
Contrast enhancement	Analog Gain (10 times max.) and Offset functions
Power consumption	70 VA
Ambient storage temperature	-10 to +50 C
Ambient operating temperature	0 to +40 C
Ambient operating/storage humidity	70%max. (no condensation)

Appendix B

Oakley & Bu cost function with variable offset

The optical back-scatter function (7.7) is substituted with b_λ in Equation (2.14) with $Sb_{syn}(\lambda) = 1$:

$$S(\kappa) = \frac{1}{P} \sum_{j=1}^P \left(\frac{I_j - \bar{I}_j}{\bar{I}_j - \kappa \cos(\theta)} \right)^2 \cdot \exp \frac{1}{P} \sum_{j=1}^P \ln(\bar{I}_j - \kappa \cos(\theta))^2. \quad (\text{B.1})$$

In recent study, (Bu 2007), it is proved that the first derivative of $S(b)$ has minimum value when $b = c$.

$$\left. \frac{d(S)}{d(b)} \right|_{b=c} = 0. \quad (\text{B.2})$$

For parametric offset, again we are looking for the value of offset function which makes the cost function minimum. The first derivative of the $S(\kappa)$ by using the chain rule is given by:

$$\frac{d(S)}{d(\kappa)} = \frac{d(S)}{d(b)} \frac{d(b)}{d(\kappa)}. \quad (\text{B.3})$$

From Equation (7.7):

$$\frac{d(b)}{d(\kappa)} = \cos(\theta). \quad (\text{B.4})$$

Substituting Equation (B.4) in Equation (B.3) gives:

$$\frac{d(S)}{d(\kappa)} = \frac{d(S)}{d(b)} \cos(\theta). \quad (\text{B.5})$$

$\frac{d(S)}{d(\kappa)}$ is zero when either $\frac{d(S)}{d(b)} = 0$ or $\cos(\theta) = 0$. The range of θ is defined in Equation (7.7) and as a result $\cos(\theta)$ never has zero value. Therefore, $\frac{d(S)}{d(b)} = 0$ which shows the function can have a minimum value at the offset value.

Bibliography

- Abdullah-Al-Wadud, M., Kabir, M. H., Dewan, M. A. A. & Chae, O. (2007), 'A dynamic histogram equalization for image contrast enhancement', *Consumer Electronics, IEEE Transactions on* **53**(2), 593 – 600.
- Ahlen, J. & Sundgren, D. (2003), 'Bottom reflectance influence on a color correction algorithm for underwater images', *Proc. SCIA* pp. 922–926.
- Ahn, J. H. & Grant, S. B. (2007), 'Size distribution, sources, and seasonality of suspended particles in southern california marine bathing waters', *Environmental Science & Technology* **41**(3), 695–702.
- Alparslan, E. & Ince, F. (1980), 'Image enhancement by local histogram stretching', *IEEE Trans on Systems, Man and Cybernetics* **SMC-11**(5), 376–385.
- Anderson, M., Motta, R., Chandrasekar, S. & Stokes, M. (1996), Proposal for a standard default color space for the internet-srgb, in 'Color Science, Systems and Applications', Proc of the S&T/SID 4th Color Imaging Conf., pp. 238–46.
- Arnott, S. H., Dix, J. K., Best, A. I. & Gregory, D. J. (2005), 'Imaging of buried archaeological materials: The reaction properties of archaeological wood', *Marine Geophysical Researches* **26**(2-4), 135–144.
- Attewell, D. & Baddeley, R. J. (2007), 'The distribution of reflectances within the visual environment', *Vision Research* (47), 548–554.
- Badamchizadeh, M. A. & Aghagolzadeh, A. (2004), 'Comparative study of unsharp masking methods for image enhancement', *Proc.-Third Int. Conf. on Image and Graphics* pp. 27–30.
- Balakrishnan, N. & Nevzorov, V. (2003), *A Primer on Statistical Distributions*, Wiley.

- Bogucki, D. J., Domaradzki, J. A., Stramski, D. & Zaneveld, J. R. (1998), 'Comparison of near-forward light scattering on oceanic turbulence and particles', *Applied Optics* **37**(21), 4669–4677.
- Botelho, S., Jr, P. D. & Leivas, G. (2008), Nlmap - visual-based self localization and mapping for autonomous underwater vehicles, in 'OCEANS 2008', IEEE Computer Society, pp. 1–6.
- Bu, H. (2007), Digital Image Enhancement, Phd, Electrical and Electronic Eng., The University of Manchester.
- Buzuloiu, V., Ciuc, M., Rangayyan, R. M. & Vertan, C. (2001), 'Adaptive-neighboring histogram equalization of color images', *Journal of Electronic Imaging* **10**(2), 445–459.
- Caimi, F. M., Kocak, D. M., Dalglish, F. & Watson, J. (2010), 'Underwater imaging and optics- recent advances', *IEEE Oceanic Engineering Society Newsletter* pp. 21–29.
- Chang, P., Flitton, J., Hopcraft, K., Jakeman, E., Jordan, D. & Walker, J. (2003), 'Improving visibility depth in passive underwater imaging by use of polarisation', *Applied Optics* **42**(15), 2794–2809.
- Chaves-Gonzalez, J. M., Vega-Rodrigueza, M. A., Gomez-Pulidoa, J. A. & Sanchez-Perez, J. M. (2010), 'Detecting skin in face recognition systems: A colour spaces study', *Digital Signal Processing* **20**(3), 806–823.
- Cheikh, F. A. & Gabbouj, M. (2000), Directional-rational approach for color image enhancement, in 'International Symposium on Circuits and Systems', Vol. 3, IEEE, pp. III-563–III-566.
- Cheung, V., Westland, S., Li, C., Hardeberg, J. & Connah, D. (2005), 'Characterization of trichromatic color cameras by using a new multispectral imaging technique', *Opt. Soc. Am.* **22**(7), 1231–1240.
- Chou, C.-H. & Liu, K.-C. (2008), 'Colour image compression based on the measure of just noticeable colour difference', *IET Image Process* **2**(6), 304–322.
- Colombo, A. G. & Jaarsma, R. J. (1980), 'A powerful numerical method to combine random variables', *IEEE Trans on Reliability* **R-29**(2), 126–129.

- Cronin, T., Shashar, N., Caldwell, R., Marshal, J., Cheroske, A. & Chiou, T. (2003), 'Polarization vision and its role in biological signalling', *Integrative and Comparative Biol* (43), 549–558.
- D. Demigny, L. K. & Pons, J. (2002), Fast recursive implementation of the gaussian filter, in '11th Int. Conf. on Very Large Scale Integration of Systems-on-Chip (VLSI)-SOC'01', SOC Design Methodologies, IFIP TC10/WG10.5, pp. 39–49.
- Dahms, H.-U. & Hwang, J.-S. (2010), 'Perspective of underwater optics in biological oceanography and plankton ecology studies', *Journal of Marine Science and Technology* **18**(1), 112–121.
- Deriche, R. (1992), Recursively implementing the gaussian and its derivatives, in 'ICIP 92, Proc. of the 2nd Singapore Int. Conf. on Image Processing', Singapore, pp. 263–267.
- Duan, J. & Qiu, G. (2004), Novel histogram processing for colour image enhancement, in 'Proc. of the Third Int. Conference on Image and Graphics (ICIG'04)', IEEE Computer society, pp. 55 – 58.
- ElMasry, G., Wanga, N., Vigneaultc, C., Qiaoa, J. & ElSayed, A. (2008), 'Early detection of apple bruises on different background colors using hyperspectral imaging', *LWT-Science Direct* **41**, 337345.
- Fairchild, M. D. (2005), *Color Appearance Models*, Wiley.
- Farnebäck, G. & Westin, C.-F. (2006), 'Improving deriche-style recursive gaussian filters', *Journal of Mathematical Imaging and Vision* **26**(3), 293–299.
- Ferrari, J. A., Flores, J. L. & Garcia-Torales, G. (2010), 'Edge enhancement by unsharp masking using liquid-crystal displays', *Journal of Modern Optics* **57**(10), 866–871.
- Foresti, G. (2001), 'Visual inspection of sea bottom structures by an autonomous underwater vehicle', *IEEE Trans. Syst.Man and Cyber part B* **31**, 691–705.
- Forrest, A. (2005), 'Colour histogram equalisation of multichannel images', *IEE Proceeding Vision, Image and Signal Processing* **152**(6), 677–686.

- Foster, D. H., Amano, K., Nascimento, S. M. C. & Foster, M. J. (2006), 'Frequency of metamerism in natural scenes', *Journal of the Optical Society of America A: Optics and Image Science, and Vision* **23**(10), 2359–2372.
- Freeman, M. H. & Hull, C. (2003), *Optics*, 11th edn, Butterworth Heinemann.
- Gasparini, F., Corchs, S. & Schettini, R. (2007), 'Low-quality image enhancement using visual attention', *Optical Engineering* **46**(4), 040502(1)–(3).
- Ghahramani, S. (2000), *Fundamentals of Probability*, 2nd edn, Pearson-Prentice Hall.
- Gilchrist, W. (1984), *Statistical Modelling*, Wiley.
- Gonzalez, R. C. & Woods, R. E. (2008), *Digital Image Processing*, 3 edn, Pearson, Prentice Hall, USA.
- Govender, M., Chetty, K. & Bulcock, H. (2007), 'A review of hyperspectral remote sensing and its application in vegetation and water resource studies', *Water SA* **33**(2), 145–151.
- Gutierrez, D., Seron, F. J., Munoz, A. & Anson, O. (2008), 'Visualizing underwater ocean optics', *Computer Graphics Forum* **27**(2), 547–556.
- Haeghen, Y. V., Naeyaert, J. M. A. D., Lemahieu, I. & Philips, W. (2000), 'An imaging system with calibrated color image acquisition for use in dermatology', *IEEE Trans on Medical Imaging* **19**(7), 722–730.
- Hardeberg, J. Y., Schmitt, F. J. M. & Brette, H. (2002), 'Multispectral color image capture using a liquid crystal tunable filter', *Optical Engineering* **41**(10), 2532–2548.
- Healey, G. E. & Kondepudy, R. (1994), 'Radiometric ccd camera calibration and noise estimation', *IEEE Transactions on Pattern Analysis and Machine Intelligence* **16**(3), 267–76.
- Hernandez-Andres, J., Jr., R. L. L. & Romero, J. (1999), 'Calculating correlated color temperatures across the entire gamut of daylight and skylight chromaticities', *APPLIED OPTICS* **38**(27), 5703–5709.
- Hirakawa, K. & Parks, T. (2005), Chromatic adaptation and white-balance problem, *in* 'ICIP 2005', Vol. 3, IEEE, pp. III – 984–7.

- Hou, W. (2009), 'A simple underwater imaging model', *Optics Letters* **34**(17), 2688–2690.
- I. Motoyoshi, Sh. Nishida, L. S. & Adelson, E. H. (2007), 'Image statistics and the perception of surface qualities', *Nature* **447**, 206–209.
- Irie, K., McKinnon, A., Unsworth, K. & Woodhead, I. (2008), 'A model for measurement of noise in ccd digital-video cameras', *Measurement Science & Technology* **19**(4), 045207.
- Ishimaru, A. (1978), 'Limitation on image resolution imposed by a random medium', *Applied Optics* **17**(3), 348–352.
- Jaffe, J. S. (1990), 'Computer modeling and the design of optimal underwater imaging systems', *IEEE Journal of Oceanic Engineering* **15**(2), 101–110.
- Jain, A. K. (1989), *Fundamentals of Digital Image Processing*, Prentice-Hall.
- Jiang, D. (2004), Digital image enhancement, Mphil, Electrical and Electronics Eng.
- Johnson, M. (2003), Real time pipeline profile extraction using recursive filtering and circle location, in 'Proc. Int. Conf. on Image Processing', Vol. 2.
- Kahanov, Y. & Royal, J. (2001), 'Analysis of hull remains of the dor d vessel, tantura lagoon, israel', *Int. J. Nautical Archeology* (30), 257–265.
- Kang, H. R. (2006), *Computational Colour Technology*, SPIE.
- Kim, J., Kim, L. & Hwang, S. (2001), 'An advanced contrast enhancement using partially overlapped sub-block histogram equalization', *IEEE, Trans. on Circuits and Systems for Video Technology* **11**(4), 475–484.
- Kim, T. & Yang, H. (2006), 'Colour histogram equalisation via least-squares fitting of isotropic gaussian mixture to uniform distribution', *Electronics Letters* **42**(8), 452–4.
- Kokhanovsky, D. A. A. (2008), *Aerosol Optics-Light Absorption and Scattering by Particles in the Atmosphere*, Springer.
- Kopeika, N. S. (1998), Causes of blur in imaging through the atmosphere: a system engineering approach to imaging, Vol. 3433, Proc. of SPIE - The International Society for Optical Engineering, pp. 320–331.

- Kopeika, N. S., I.Dror & Sadot, D. (1998), 'Causes of atmospheric blur - comment on atmospheric scattering effect on spatial resolution of imaging systems', *Optical Society of America-Optics and Image Science, and Vision* **15**(12), 3097–3106.
- Krauskopf, J. (2001), A journey in color space, in 'Color Research & Application', Vol. 26, 15th Meeting of the International Color Vision Society, pp. S2–11.
- K.V. Mardia, J. A. & Goitía, A. (2006), 'Synthesis of image deformation strategies', *Science Direct-Image and Vision Computing* **24**(1), 1–12.
- Lamberti, F., Montrucchio, B. & Sanna, A. (2004), Bbfhe: Block-based binomial filtering histogram equalization, in 'Trans on information science and applications', Vol. 6, WSEAS, Venice.
- Lee, E. H., Ahn, S. C. & Kim, J. H. (2000), Colour reproduction based on spectral reflectance, in 'Color Imaging: Device-Independent Color, Color Hardcopy, and Graphic Arts V', Vol. 3963, SPIE, pp. 101–108.
- Lee, K.-W., Kim, Y.-S., Park, S.-H., Suryanto & Ko, S.-J. (2008), 'Effective color distortion and noise reduction for unsharp masking in lcd', *IEEE Transactions on Consumer Electronics* **54**(3), 1473–7.
- Levi, L. & Mossel, M. (1976), On perfect image correction by unsharp masking, in 'Applications of Holography and Optical Data Processing, Israel', pp. 73–83.
- Levman, J., Alirezaei, J. & Khan, G. (2003), Perfectly flat histogram equalization, in 'Signal Processing and Pattern Recognition and Applications', IASTED, Rhodes Greece, pp. 38–40.
- Lewis, G. D., Jordan, D. L. & Roberts, P. J. (1999), 'Backscattering target detection in a turbid medium by polarization discrimination', *APPLIED OPTICS* **38**(18), 3937–3944.
- Li, H., Wang, X., Bai, T., Jin, W., Huang, Y. & Ding, K. (2009), 'Speckle noise suppression of range gated underwater imaging system', *Proc. of the SPIE - The Int. Society for Optical Engineering* **7443**, 74432A1–8.
- li Hu, J., bing Deng, J. & shan Zou, S. (2010), 'A novel algorithm for color space conversion model from cmyk to lab', *Journal of Multimedia* **5**(2), 159–166.

- Lin, S.-S., Yemelyanov, K. M., Jr., E. N. P. & Engheta, N. (2004), Polarization enhanced visual surveillance techniques, *in* 'Proceedings of the 2004 IEEE International Conference on Networking Sensing & Control', IEEE, Taiwan, pp. 216–221.
- Liu, C., Szeliski, R., Kang, S. B., Zitnick, C. L. & Freeman, W. T. (2008), 'Automatic estimation and removal of noise from single image', *IEEE Trans. on Pattern Analysis and Machine Intelligence* **30**(2), 299–314.
- Liu, S., Chen, Y. & Xia, Y. (1994), 'Viewing method for improving underwater visibility by reduction of back-scatter', *Applied Optics* **33**(26), 6213–18.
- L.J. van Vliet, I. Y. & Verbeek, P. W. (1998), Recursive gaussian derivative filters, *in* 'Proc. of the 14th Int. Conf. on Pattern Recognition', IEEE, Computer Society Press, Brisbane-Australia, pp. 509–514.
- Lukas, J., Fredrich, J. & Goljan, M. (2006), 'Digital camera identification from sensor pattern noise', *IEEE Transactions on Information Forensics and Security* **1**(2), 205–214.
- McCartney, E. J. (1976), *Optics of the atmosphere scattering by molecules and particles*, Wiley.
- McNeil, L. E., Hanuska, A. R. & French, R. H. (2001), 'Orientation dependence in near-field scattering from tio₂ particles', *Applied Optics* **40**(22), 3726–36.
- Moller, B. & Posch, S. (2008), 'An integrated analysis concept for errors in image registration', *Pattern Recognition and Image Analysis* **18**(2), 201–206.
- Mortazavi, H. (2006), Underwater image enhancement, Mphil, Electrical and Electronics Eng.
- Mortazavi, H. & Oakley, J. (2007), 'Underwater image enhancement by backscatter compensation', *ICMSAO2007 Conf.* .
- Narimani, M., Nazem, S. & Loueipour, M. (2009), Robotics vision-based system for an underwater pipeline and cable tracker, *in* 'OCEANS 2009', IEEE, p. 6.
- Nimeroff, I. & Yurow, J. (1965), 'Degree of metamerism', *Journal of the Optical Society of America* **55**(2), 185–190.

- Oakley, J. & Bu, H. (2007), 'Correction of simple contrast loss in colour images', *IEEE, Trans. on Image Processing* **16**(2), 511–522.
- Oakley, J. & Satherley, B. L. (1998), 'Improving image quality in poor visibility conditions using a physical model for contrast degradation', *IEEE, Trans. on Image Processing* **7**(2), 167–179.
- Ohno, Y. (2000), Cie fundamental for colour measurements, in 'IS&T NIP16', Vancouver, pp. 16–20.
- Pal, N. & Pal, S. (1991), 'Image model, poisson distribution and object extraction', *Int. Journal of Pattern Recognition and Artificial Intelligence* **5**(3), 459–83.
- Peli, E. (1990), 'Contrast in complex images', *Journal of Optical Society of America* **7**(10), 2032–2040.
- Petrou, M. & Bosdogianni, P. (1999), *Image Processing The Fundamentals*, Wiley.
- Pointer, M. R. (2002), Cie: vision, color, and imaging, in '9th Congress of the International Colour Association', Vol. 4421, SPIE, pp. 547–9.
- Polesel, A., Ramponi, G. & Mathews, J. (2000), 'Image enhancement via adaptive unsharp masking', *IEEE Trans. on Image Processing* **9**(3), 505–510.
- Rao, C., Mukherjee, K., Gupta, S., Ray, A. & Phoha, S. (2009), Underwater mine detection using symbolic pattern analysis of sidescan sonar images, in 'ACC-09', 2009 American Control Conference, pp. 5416–21.
- Reibel, Y., Jung, M., Bouhifd, M., Cunin, B. & Draman, C. (2003), 'Ccd or cmos camera noise characterisation', *The European Physical Journal Applied Physics* **1**(21), 75–80.
- Reynolds, R. A., Stramski, D., Wright, V. M. & Wozniak, S. B. (2008), Particle size distribution of coastal waters measured with an in situ laser diffractometer, in '20th Conference on Ocean Optics', Ocean Optics XIX Conference.
- Robinson, D. & Milanfar, P. (2004), 'Fundamental performance limits in image registration', *IEEE, Transactions on Image Processing* **13**(9), 1185–1199.
- Roode, R. D., Noordmans, H. J., Verdaasdonk, R. M. & Sigurdsson, V. (2006), 'Multispectral system evaluates treatments in dermatology', *Laser Focus World* **42**(4), 102–104.

- S. Tan, J. & Johnston, A. (2003), 'Performance of three recursive algorithms for fast space-variant gaussian filtering', *Real Time Imaging* **9**(3), 215–228.
- Schechner, Y. & Karpel, N. (2005), 'Recovery of underwater visibility and structure by polarization analysis', *IEEE J. of Oceanic Eng.* **30**(3), 570–587.
- Schechner, Y. Y. & Averbuch, Y. (2007), 'Regularized image recovery in scattering media', *IEEE Trans. on Pattern Analysis and Machine Intelligence* **29**(9), 1655–1660.
- Schechner, Y. Y. & Karpel, N. (2004), Clear underwater vision, in 'CVPR 04', Vol. 1, Proc. of the 2004 IEEE Computer Soc. Conf. on Computer Vision and Pattern Recognition, pp. 536–43.
- Sharma, G. & Trussell, H. J. (1997), 'Digital color imaging', *IEEE Transaction of Image Processing* **6**(7), 901–932.
- Sheldon, R., Prakash, A. & Sutcliffe, W. (1972), 'The size distribution of particles in the ocean', *Limnology and Oceanography* **17**(3), 327–340.
- Sivaswamy, J., Salcic, Z. & Ling, K. L. (2001), 'A real-time implementation of non-linear unsharp masking with fplds', *Real Time Imaging* **7**, 195–202.
- Spaulding, K. & Holm, J. (2002), Color encodings: srgb and beyond, in 'Image Processing, Image Quality, Image Capture, Systems Conference', Society for Imaging Science and Technology, pp. 167–171.
- Srivastava, A., Lee, A., Simoncelli, E. & Zhu, S.-C. (2003), 'On advances in statistical modeling of natural images', *J. of Mathematical Imaging and Vision* **18**(1), 17–33.
- Stokes, M., Fairchild, M. & Berns, R. S. (1992), 'Precision required for digital color reproduction', *ACM Transactions on Graphics* **11**(4), 406–422.
- Sullivan, J., Twardowski, M. S., Donaghay, P. & Freeman, S. A. (2005), 'Use of optical scattering to discriminate particle types in coastal waters', *Applied Optics* **44**(9), 1667–1680.
- Tan, C. S., Sluzek, A., L., G. S. G. & Jiang, T. Y. (2007), Range gated imaging system for underwater robotic vehicle, in 'OCEANS 2006', 16th IEEE Int. Symp. on the Applications of Ferroelectrics, pp. 1–6.

- Tan, C., Seet, G., Sluzek, A. & He, D. M. (2005), 'A novel application of range-gated underwater laser imaging system (ulis) in near target turbid medium', *Optics and Laser in Eng.* **43**, 995–1009.
- Tan, K. & Oakley, J. (2001), 'Physics based approach to color image enhancement in poor visibility conditions', *J. Optical Society of America* **18**(10), 2460–2467.
- Tao, Y., Lin, H., Bao, H., Dong, F. & Clapworthy, G. (2009), 'Feature enhancement by volumetric unsharp masking', *Visual Computer* **25**(5-7), 581–588.
- Treibitz, T. & Schechner, Y. Y. (2006), Instant 3descatter, in 'CVPR 2006', Vol. 2, IEEE Computer Society Conference on Computer Vision and Pattern Recognition, New York, United States, pp. 1861–1868.
- Treibitz, T. & Schechner, Y. Y. (2009), 'Active polarization descattering', *IEEE Trans. on Pattern Analysis and Machine Intelligence* **31**(3), 385 – 399.
- Trucco, E. & Olmos-Antillon, A. T. (2006), 'Self-tuning underwater image restoration', *IEEE JOURNAL OF OCEANIC ENGINEERING* **31**(2), 511–519.
- Tyo, J. S., Rowe, M. P., Jr., E. N. P. & Engheta, N. (1996), 'Target detection in optically scattering media by polarization-difference imaging', *APPLIED OPTICS* **35**(11), 1855–1870.
- Valero, E. M., Nieves, J. L., Nascimento, S. M. C., Amano, K. & Foster, D. H. (2007), 'Recovering spectral data from natural scenes with an rgb digital camera and colored filters', *Color research and application* **32**(5), 352.
- Voss, K. J. (1991), 'Simple empirical model of the oceanic point spread function', *Optics* **30**(18), 2647–2651.
- Wagner, S. (2007), 'Match makers', *Engineer* **293**(7718), 33.
- Weeks, A. R., Sartor, L. J. & Myler, H. R. (1999), Histogram specification of 24-bit color images in the color difference (c-y) color space, in 'Nonlinear Image Processing', Vol. 3646, SPIE, San Jose, pp. 319–329.
- Weiss, Y. & Freeman, W. T. (2007), What makes a good model of natural images?, in 'IEEE Computer Society Conference on Computer Vision and Pattern Recognition', IEEE-CVPR'07.

- Westland, S. & Ripamonti, C. (2004), *Computational Colour Science Using MATLAB*, Wiley.
- Withagen, P. J., Groen, F. C. A. & Schutte, K. (2007), 'Ccd color camera characterization for image measurements', *IEEE Transaction on Instrumentation and Measurement* **56**(1), 199–203.
- Wyszecki, G. & Stiles, W. (1982), *Color Science: Concepts and Methods, Quantitative Data and Formulae*, 2nd edn, John Wiley.
- Xu, X. & Negahdaripour, S. (1999), 'Automatic optical station keeping and navigation of an rovs: sea trial experiment', *Proc. Oceans* **1**, 71–76.
- Y. Zimmer, R. T. & Akselrod, S. (2000), A lognormal approximation for the gray level statistics in ultrasound images, in 'Proc. of the 22nd Annual Int. Conf. of the IEEE', Vol. 4, IEEE, pp. 2656–61.
- Yamaguchi, M., Haneishi, H. & Ohyama, N. (2008), 'Beyond red-green-blue (rgb): Spectrum-based color imaging technology', *Imaging Science and Technology* **52**(1), 1–15.
- Yemelyanov, K. M., Lin, S.-S., Pugh, E. N., Jr. & Engheta, N. (2006), 'Adaptive algorithms for two-channel polarization sensing under various polarization statistics with nonuniform distributions', *Applied Optics* **45**(22), 5504–5520.
- Young, I. & van Vliet, L. (1995), 'Recursive implementation of the gaussian filter', *Signal Processing* **44**, 139–151.
- Yu, C.-H. & Chen, S.-Y. (2006), 'Universal colour quantisation for different colour spaces', *IEE, Proc. Image Signal Process* **153**(4), 445–455.
- Yu, Y. & Liu, F. (2007), 'System of remote-operated-vehicle-based underwater blurred image restoration', *Optical Engineering* **46**(11).
- Yura, H. T. (1971), 'Small-angle scattering of light by ocean water', *Applied Optics* **10**(1), 114–118.
- Zawada, D. G. (2003), 'Image processing of underwater multispectral imagery', *IEEE, Journal of Oceanic Engineering* **28**(4), 583–594.

- Zhou, Q. (2004), *Illumination Compensation*, PhD thesis, Electrical and Electronic, UMIST, Manchester, UK.
- Zhu, H., Chan, F. H. Y. & Lam, F. K. (1999), 'Image contrast enhancement by constrained local histogram equalization', *Computer Vision and Image Understanding* **73**(2), 281–290.
- Zitova, B. & Flusser, J. (2003), 'Image registration methods: A survey', *Image and Vision Computing* **21**(11), 977–1000.